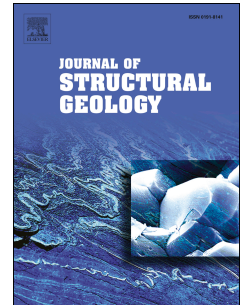


# Journal Pre-proof

Shape of plutons in crustal shear zones: A tectono-magmatic guide based on analogue models

Maria Michail, Michael Rudolf, Matthias Rosenau, Alberto Riva, Piero Gianolla, Massimo Coltorti



PII: S0191-8141(21)00141-3

DOI: <https://doi.org/10.1016/j.jsg.2021.104417>

Reference: SG 104417

To appear in: *Journal of Structural Geology*

Received Date: 27 July 2020

Revised Date: 17 June 2021

Accepted Date: 7 July 2021

Please cite this article as: Michail, M., Rudolf, M., Rosenau, M., Riva, A., Gianolla, P., Coltorti, M., Shape of plutons in crustal shear zones: A tectono-magmatic guide based on analogue models, *Journal of Structural Geology*, <https://doi.org/10.1016/j.jsg.2021.104417>.

This is a PDF file of an article that has undergone enhancements after acceptance, such as the addition of a cover page and metadata, and formatting for readability, but it is not yet the definitive version of record. This version will undergo additional copyediting, typesetting and review before it is published in its final form, but we are providing this version to give early visibility of the article. Please note that, during the production process, errors may be discovered which could affect the content, and all legal disclaimers that apply to the journal pertain.

© 2021 Elsevier Ltd. All rights reserved.

### Author Statement

The authors of the current study declare that this manuscript is original, has not been published before and is not currently being considered for publication elsewhere.

As a corresponding author I am responsible for communicating with the other authors about progress, submissions of revisions and final approval of proofs.

As the lead and corresponding author, I confirm that the manuscript has been read and approved by all named authors. I further confirm that the order of authors listed in the manuscript has been approved by all authors and is in accordance with the authors' diverse contributions to this work:

1. **Maria Michail:** Conceptualization, Methodology, Investigation, Visualization, Writing - Review & Editing
2. **Michael Rudolf:** Software, Formal analysis, Visualization, Writing - Review & Editing
3. **Matthias Rosenau:** Conceptualization, Supervision, Resources, Writing - Review & Editing
4. **Alberto Riva:** Supervision, Writing - Review & Editing
5. **Piero Gianolla:** Supervision, Review & Editing
6. **Massimo Coltorti:** Supervision, Review & Editing

Sincerely,

Maria Michail and co-authors

# Shape of plutons in crustal shear zones: A tectono-magmatic guide based on analogue models

Maria Michail <sup>a</sup>, Michael Rudolf <sup>b</sup>, Matthias Rosenau <sup>b</sup>, Alberto Riva <sup>a</sup>, Piero Gianolla <sup>a</sup>, Massimo Coltorti <sup>a,c</sup>

<sup>a</sup> University of Ferrara, Department of Physics and Earth Sciences, Via Saragat 1, 44122 Ferrara, Italy

<sup>b</sup> Helmholtz Centre Potsdam, GFZ German Research Centre for Geosciences, Telegrafenberg, 14473 Potsdam, Germany

<sup>c</sup> National Institute of Geophysics and Volcanology, Palermo branch, Via Ugo la Malfa 153, 90125 Palermo, Italy

Corresponding author: Maria Michail, email address: [mchmra@unife.it](mailto:mchmra@unife.it), tel. 00393200486527

## Keywords:

1. Analogue modelling;
2. Magma emplacement;
3. Strike-slip tectonics;
4. Transtension;
5. Pluton shape

**Abstract**

Plutons in crustal shear zones may exploit inherited structures, interfere with strain localizing or be deformed passively. To constrain the relative timing of such tectono-magmatic relationships in natural settings is not always straight-forward. We here present sandbox-type analogue model experiments simulating magma emplacement into simple and transtensional crustal shear zones to test the diagnostic potential of pluton shape with respect to timing and setting. Observations based on surface deformation and intrusion shape exemplify the interplay between evolving and inherited tectonic structures and magma uprising. We observe markedly asymmetric intrusions in association with dikes reflecting the regional stresses, fault pattern and finite strain field. At the same time, the presence of an intrusion modifies the tectonic evolution, but only transiently, resulting in short-lived faults, reactivation and inversion. Diagnostic attributes include the pluton's aspect ratio, its orientation and amplitude as well as dike association. Accordingly, syn-tectonic intrusions show the highest pluton amplitudes, but only intermediate elongation compared to other scenarios. They are oriented parallel to Riedel shears in simple shear, respectively to the compression direction in transtension. Post-tectonic intrusions are least elongated, have medium amplitudes and exploit Riedel shears. Pre-tectonic intrusions are characterized by lowest amplitudes but the highest aspect ratios and are parallel to the finite elongation direction. Intrusions in transtensional shear zones are generally of less elongate than those in simple shear zones. Experimental results are tested against observations from natural examples validating the diagnostic potential of pluton shape for the timing and the tectonic setting of the emplacement.

**1 Introduction**

The spatial association of plutons and shear zones has long been recognized. Revealing their temporal and spatial relation as a key to understand the mechanisms of tectono-magmatic interaction, is a matter of research since. The interactions of tectonic and magmatic processes are often ambiguous and hard to interpret (Paterson and Schmidt, 1999; Paterson and Tobisch, 1992).

It is generally recognised that both inherited structures and active faults but also the tectonic stress field represent key features in crustal-scale magma transport and emplacement (Hutton, 1988; Hutton and Reavy 1992; Vigneresse 1995; Román-Berdiel et al., 1997; Petford et al., 2000; Handy et al., 2001; Rosenberg, 2004; Corti et al., 2005; Galland et al., 2006; Galland et al., 2007b). Likewise, the presence of magma in actively deforming crust may control fault localization and structural evolution (e.g. Holohan et al., 2008; Dooley and Schreurs, 2012; Gomes et al., 2019). The delineated scenarios of pre-, syn- and post-tectonic magmatism and the mechanisms involved remain poorly understood taking also into account that gathering information from the field could be rather challenging (Fig. 1). Beside the limited outcrops in some areas, observations are, in most cases, restricted to the final stage of magma emplacement which is often overprinted. In addition, the deformed upper crustal layers that once hosted the magmatic chamber are in most cases subject to erosion and therefore missing from the field. Consequently, the information on the incremental and finite deformation has to be inferred with much effort from structural indicators and the processes taking place at depth must be extrapolated (Vigneresse, 1995).

Modelling can help in overcoming some of the restrictions of field analysis and guide researchers by identifying key observables and testing hypothesis. Modelling studies on tectono-magmatic interaction included analytical (e.g. Mandal and Chakraborty, 1990), numerical (e.g. Burov et al., 2003), and analogue approaches (see e.g. review by Galland et al., 2015). The latter were particularly suited for the typically cross-scale and four-dimensional problems posed by tectono-magmatic processes. Amongst them, studies on syn-tectonic magma emplacement prevail: a) in compressional settings (Galland et al., 2003, 2006, 2007; Mazzarini et al., 2010; Montanari et al., 2010); b) in strike-slip settings (Román-Berdiel et al., 1997; Corti et al., 2005; Mazzarini et al., 2010; Gomes et al., 2019); c) in transpressional settings (Benn et al., 1998); d) in transtensional settings (Román-Berdiel et al., 2000; Corti et al., 2003) and finally e) in extensional settings (Román-Berdiel et al., 1999; Mazzarini et al., 2010; Corti et al., 2003). Only few analogue modelling studies exist regarding the shearing of pre-tectonic intrusions (e.g. Holohan et al., 2008; Dooley and Schreurs,

2012; Gomes et al., 2019). Similarly, the post-tectonic intrusion scenario is very poorly studied, where exploitation of inherited structures from the uprising intrusion is still under debate.

In this paper, we aim at closing this knowledge gap and test the diagnostic potential of pluton shape for relative timing with a new set of analogue model experiments simulating magma emplacement within the upper brittle crust rising from a basal ductile shear zone. We conduct a systematic series of magma emplacement scenarios in simple shear and transtensional regime (Fig. 2). To cover the full range of relative timing, we analyze pre-tectonic, syn-tectonic and post-tectonic intrusion scenarios (Table 1).

In contrast to earlier analogue modelling studies with a similar goal (e.g. Román-Berdiel et al., 1997; Corti et al., 2005; Holohan et al., 2008; Mazzarini et al., 2010, Gomes et al., 2019), we do not use a Riedel-type experiment with a linear velocity discontinuity at the base but a distributed basal shear zone (e.g. Dooley and Schreurs, 2012, and references therein). This seems a more realistic basal kinematic boundary condition if brittle-viscous deformation at mid-crustal levels is considered (e.g. Handy et al., 2001). According to our conceptual model of pluton emplacement (Fig. 1b), our model pluton rises from this viscous shear zone instead of being injected in a purely brittle deforming model upper crustal layer.

Using state of the art kinematic monitoring techniques (Digital Image correlation – DIC; Structure-from-Motion – SfM), the full 3D surface deformation over time (i.e. 4D deformation) and the final intrusion three-dimensional shapes are captured digitally at high resolution and accuracy. Based on this experimental data set, which is openly available (Michail et al., 2021), we identify diagnostic features of pluton shape and validate them against selected field examples. The presented models therefore appear as a guide to the interpretation of necessarily incomplete and limited field observations.

96 2.1 *Experimental setup*

97 The experimental setup consists of two mobile plastic plates on a 1 by 1 m wide solid steel support  
98 platform. The mobile plates are moved by linear actuators, controlled by stepper motors, in opposite  
99 direction (Fig. 2). A 40-mm wide gap between the two 700 mm long and 7 mm thick mobile plates  
100 is filled with viscous material (silicone oil) to allow the formation of a distributed basal shear zone,  
101 similar to natural lower crustal shear zones (Fig. 2a-b). Two kinematically distinct experimental  
102 series, representing two different tectonic regimes, namely simple shear (reference model RS and  
103 models of group A; Fig. 2c,e) and transtension (reference model RT and models of group B; Fig.  
104 2d,f) are presented (Table 1).

105 For the simple shear regime, the gap between the mobile plates is oriented parallel to the plates'  
106 motion (Fig. 2c,e), while in the transtensional configuration, they are oriented with an angle,  $\alpha$ , of  
107  $15^\circ$  (Fig. 2d). Relative plate velocity is fixed to 1 mm/min, for all experiments, which corresponds to  
108 a simple shear rate of  $4.2 \cdot 10^{-4} \text{ s}^{-1}$  across the width of gap resulting in a final relative displacement of  
109 the two sides of the shear zone of 60 mm for all experiments. A low shear rate, together with a  
110 viscous fluid, rough inner edges of the mobile plates and polished and lubricated surface of the  
111 metal base, result in a well distributed deformation within the gap although minor localization of  
112 shear and extension at the shear zone boundaries is unavoidable.

113 A 40-mm thick, sieved quartz sand layer representing the brittle upper crust (Fig. 2a-b) covers the  
114 mobile plates and the basal shear zone. On top of each mobile plate, fixed, motion-parallel sidebars  
115 confine the sand layer laterally and helps in model preparation (Fig. 2a,e). In the centre of the basal  
116 shear zone, a motor-controlled piston pushes silicone oil up through a pipe (with 40 mm diameter)  
117 placed beneath the experiment's foundation, to simulate the magma ascending from the lower crust  
118 into the upper-crustal shear zone (Fig. 2e-f). The piston moves at a velocity of 1 mm/min, which  
119 translates into an injection rate of  $21 \text{ mm}^3/\text{s}$  for all experiments (Table 1). All the experiments are  
120 performed under air-controlled ambient conditions ( $23^\circ\text{-}25^\circ\text{C}$ , 50% humidity).

## 2.2 *Analogue materials*

The viscous (or ductile) analogue material used for both the intrusion and the basal ductile layer is a silicone oil (Polydimethylsiloxane PDMS, G30M by K. Obermeier GmbH). It has a density of  $965 \text{ kg m}^{-3}$  and a Newtonian viscosity of  $22.4 \text{ kPa s}$  at laboratory strain rates below  $10^{-2} \text{ s}^{-1}$  (Rudolf et al., 2016; see Table 2). Earlier studies showed that similar material is a suitable analogue for ductile lower crust and, at reduced viscosity, for low density-high viscosity (i.e. granitic) magmas simulation (e.g. Román-Berdiel et al., 1997; Benn et al., 1998, 2000; Galland et al., 2015). We here use a single material for simulating both the ductile lower crust and the magma in order to reduce rheological complexity but also due to practical reasons, i.e. to avoid gravitational collapse of the model pluton during manual excavation and before photogrammetric imaging.

Sieved dry quartz-sand (G12) functions as brittle analogue of the upper crust. The sand is a well-sorted, well-rounded and fine-grained ( $<400 \text{ }\mu\text{m}$ ) sand of fluvial origin (Klinkmüller et al., 2016; Rosenau et al., 2018). When sieved, a bulk density  $\rho \sim 1600 \text{ kgm}^{-3}$  is reached and the sand layer is characterized by internal friction coefficients  $\mu$  of 0.69, 0.62, 0.55 (static, reactivated, sliding) and a cohesion  $C$  in the order of 50 - 110 Pa (Table 1). The localization behaviour of sand produces shear zones several grain diameters wide rather than idealized infinitely narrow faults. However, we here use the term “faults”, to describe the small-scale shear zones, evolving in the analogue model because of the generally close dynamic similarity (Ritter et al., 2016). With the term “shear zone” in contrast we refer to the regional deformation zone composed of several faults evolving on top of the basal ductile shear zone.

## 2.3 *Scaling and Similarity*

The experiments are scaled following the principles of geometric, kinematic and dynamic similarities to the natural prototype (Hubbert, 1937; Ramberg, 1981; Weijermars and Schmeling, 1986). Accordingly, for a brittle-viscous sandbox model under normal gravity, the stress scaling dictates the length and time scaling. In the pressure-dependent brittle regime and under normal gravity, the

length scale  $L^*$  can be delineated from densities and cohesion in the model and prototype following the scaling law:

$$L^* = C^* / \rho^* \quad (i)$$

where the asterisks denote the model/prototype ratios known as the scaling factors (i.e.  $C^* = C_{model}/C_{prototype}$ ). Inserting numbers for the scaling factors for density and cohesion of our brittle analogue rock material ( $C_{model} \sim 10\text{-}100$  Pa,  $\rho_{model} = 1600$  kg/m<sup>3</sup>) and typical upper crustal rocks ( $C_{prototype} = 10$  MPa,  $\rho_{prototype} = 2600$  kg/m<sup>3</sup>) yields a length scaling factor of  $L^*$  in the order of  $0.6\text{-}6 \times 10^{-6}$ , i.e. 1 cm in the model equals 0.6-6 km in nature (Table 2). Consequently, our model represents an intrusion into the upper 2-20 km thick crust. For our models, due to dimensional identity, the stress scale is also fixed by the choice of cohesion to  $\sigma^* = 1\text{-}10 \times 10^{-6}$ .

In the strain-rate dependent viscous regime the time-scale  $T^*$  can be delineated, based on dimensional arguments, from the viscosities  $\eta$  in the model and in nature using the formerly set stress scale and following the scaling law

$$T^* = \eta^* / \sigma^*. \quad (ii)$$

With the viscosity of the silicone oil ( $\eta_{model} \sim 10^4$  Pas) and considering a typical viscosity range for magma ( $\eta_{prototype} = 10^4\text{-}10^{10}$  Pas), this scaling yields highly unsuitable laboratory time scales, that require running the experiments at even lower rates than in nature. This dilemma has already been noticed by Ramberg (1981) who stated that magma cannot be properly scaled because even the most viscous (low water content, high silica) magma would require an analogue fluid, which is even less viscous than water and which does not exist. **(Table 2 here)**

To solve this dilemma, we here consider the rising magmatic body not as a homogenous melt with low viscosity but as a succession of rapid melt injections into the crust over millions of years. This is in accordance to the general view that plutons grow transiently over the Ma timescale fed by magma that transits through lower crustal shear zones episodically on the hundreds to thousands of years timescale (e.g. Handy et al., 2001, Patterson et al., 2011, Brown, 2013). The resulting

magmatic system has therefore an effective bulk viscosity much higher than that of the individual melt components and which is more similar to ductile lower (quartz-feldspatic/andesitic) crust at typical regional tectonic strain rates ( $\eta_{prototype} > 10^{20}$  Pas at  $< 10^{-14} \text{ s}^{-1}$ , e.g. Shinevar et al., 2015). Such an alternative interpretation of the analogue model is not only consistent with modern views of episodic pluton growth but considers at the same time, though highly simplified, thermal aspects of the emplacement process (i.e. cooling and crystallization between injection episodes; Gomes et al., 2019). Following this reasoning and considering a Million-year time scale of pluton growth, we derive the time scale by relating the filling times of our model pluton (ca.  $10^{-8} \text{ m}^3/\text{s}$ ) to mean natural rates of  $10^2 \text{ km}^3/\text{Ma}$  (e.g. Patterson et al., 2011). Accordingly, we arrive at  $T^* = 10^{-13}$  (1 second in the lab corresponds to ca. 30.000 years, Table 2). According to this timescale the applied velocity of 1 mm/min scales to ca. 0.5 mm/a in nature and a corresponding shear rate of ca.  $10^{-17} \text{ s}^{-1}$ .

## 2.4 Monitoring and Analysis

We use state-of-the-art digital image correlation techniques for kinematic monitoring of the model surface deformation (Particle Image Velocimetry, PIV) and for deriving the surface topography and intrusion shape (Structure-from-Motion, SfM). All digital data generated in this study are published open access in Michail et al. (2021).

### 2.4.1 Particle Image Velocimetry (PIV)

A stereoscopic pair of charge-coupled device (CCD) cameras (11 MPx, 14bit, LaVision Imager ProX) monitor the model surface during the experimental run at a frequency of 0.3 Hz (Fig. 2a). Digital image correlation, using a least square minimization technique (as implemented in LaVision Davis 8), allows a quasi-continuous quantitative monitoring of the topographic evolution and surface deformation at high spatio-temporal resolution according to the principles of PIV (Adam et al., 2005). We derive 3D incremental and cumulative surface deformation pattern (i.e. velocity fields, strain fields and topography) at the sub-millimetre resolution.

From the surface velocity field, we produce surface strain maps by means of the incremental normal strain  $E_n$  and shear strain  $E_{xy}$  (in millistrain, mS), highlighting active faults and their kinematics. Positive values (red colours in all figures) indicate extension and clockwise rotation or dextral shear sense, respectively. One increment in this study is 30 seconds long corresponding to 0.5 mm of piston and/or 0.5 mm of shear (relative motion of opposing sides). The final shear strain is computed as the cumulative (or finite) displacement field by summing up the incremental deformation fields indicating the relative importance of individual faults in accommodating deformation over the full experimental range. See Michail et al. (2021) for further technical details and data.

#### 2.4.2 Structure-from-Motion (SfM)

To obtain the 3D model reconstruction of the final topography (digital elevation model, DEM) and the final intrusion shape (digital intrusion model, DIM) at high resolution we rely on the Structure-from-motion (SfM) technique (Westoby et al., 2012) using digital images taken at the end of every experiment with a customer grade DSLR camera (NIKON D80, 10 MPx). For the 3D model reconstruction we use Agisoft PhotoScan (Professional Edition) by taking images from various angles including perspective views of both the final model surface and the model intrusion after excavation. For visualization we extract coloured DIM-contours from each model.

The intrusion's geometry (pluton shape) is quantified using various dimensionless parameters derived from the DIM:

First, its normalized amplitude

$$A_{intrusion} = H_{intrusion} / H_{sand\ layer} \quad (iii)$$

where  $H_{intrusion}$  is the intrusion height above the initial surface of the ductile layer and  $H_{sand\ layer}$  is the thickness of the sand layer (i.e. 40 mm). Second, the aspect ratio

$$r = L/W \quad (iv)$$

calculated based on the length  $L$  and width  $W$  of the ellipse that fits to the DIM perimeter at a given contour level.

Third, the orientation of the intrusion, that is described by  $\Theta$ , defined as the small angle between the long axis  $L$  of the fitted ellipse and the strike of the basal shear zone.  $\Theta$  is counted counter clockwise in dextral shear (Fig. 1). Aspect ratio and angle of intrusion are derived for each contour level allowing the analysis of the shape as a function of height.

### 3 Experimental results

In this study we present and analyze nine experiments in total (Table 1): i) three reference experiments (Group R); ii) three models of intrusion under (dextral) simple shear (Group A) and iii) three models of intrusion under (dextral) transtension (Group B). Pre-, syn and post-tectonic intrusion scenarios are presented for the Groups A and B. Group R consists of a static intrusion without applied shear (R0), a simple shear (RS) and a transtensional experiment (RT), both without intrusion. Rates of intrusion and deformation are kept constant in all experiments as well as the thickness of the brittle layer.

#### 3.1 Reference models (Group R)

The surface evolution of the reference experiments, namely the static intrusion model (R0, Fig. 3a-f), the simple shear model (RS, Fig. 3g-i) and the transtension model (RT, Fig. 3j-l) is shown in Fig. 3. In the R0 model, a circular sand dome starts forming as soon as the injection has started ( $V_{inj} = 3.2$  ml; Fig. 3a, d) characterized by diffuse surface extension in the centre and diffuse lateral shortening and conjugate shear. Gradually, the sand layer forms an elongated rectangular domal uplift bound by a conjugate set of lateral oblique reverse faults, parallel to the basal ductile layer (Fig. 3b-c, e-f). The uplift rate decreases with time (not shown here).

For the reference experiments under simple shear (RS) and transtensional (RT) deformation the surface evolution shows a typical sequence of structures consistent with previous studies using a distributed basal shear zone and dry sand layers (Román-Berdiel et al., 1997; Corti et al., 2005; Dooley and Schreurs, 2012). In the very early evolution stage of the RS model ( $d_{rel} = 5.0$ mm) a diffuse belt starts to form above the basal ductile shear zone (Fig. 3g). With increasing displacement,

early en-echelon synthetic Riedel shears (R) develop with a trend of  $\sim 20^\circ$  to the trace of the basal shear zone ( $d_{rel} = 16.1$  mm; Fig. 3h). Lower-angle synthetic shears develop between the overlapping R shears, having a strike of  $\sim 15^\circ$  with respect to the shear zone boundary (Fig. 3h). The final deformation surface pattern ( $d_{rel} = 38.3$  mm) is characterised by the formation of an active and continuous master fault (MF), as a result of the linkage of the individual early shear structures, parallel to the basal shear zone, along which the less active anastomosing minor faults define shear lenses and pop-up structures ( $d_{rel} = 38.3$  mm; Fig. 3i). The final surface width of the shear zone (ca. 50 mm) is larger than the basal shear zone (40 mm; Fig. 3i).

The transtensional reference experiment (RT) shows an early evolutionary history similar to the simple shear experiment with the formation of a diffuse shear zone above the basal ductile shear zone (Fig. 3j-l). Linkage of early right-stepping and overlapping R shears occur along lower angle structures (Y, P shears) causing a deformation localization in the central part and forming a through-going master fault from early on ( $d = 11.1$  mm; Fig. 3j-k). During the final stage, the deformation partitions between lateral faults and fault-bounded rhomboidal basin structures (Fig. 3l). In this stage, the pull-apart basin structure is cut short by strike-slip faults that continue to propagate towards the dominating parallel boundary faults. This results in lengthening and narrowing of the pull-apart basin in a direction parallel to the displacement vector. The final surface width of the shear zone is larger (ca. 60 mm) than the basal shear zone (44.4 mm; Fig. 3i).

## 3.2 Simple shear intrusion models (Group A)

### 3.2.1 Effect of intrusion on fault pattern

The three models presented in this group show the evolution of deformation with the presence of analogue magma injection that predates (A1, pre-tectonic model), coincides (A2, syn-tectonic model) and post-dates (A3 post-tectonic model) the applied simple shear deformation. Our observations focus on the interactions taking place between faulting and intrusion and how they affect the fault pattern evolution and the final intrusion geometry.

270 The pre-tectonic intrusion experiment, Model A1 (Fig. 4), consists of two parts: during the first half  
 271 of the experiment, static intrusion takes place ( $V_{inj} = 37.3$  ml) causing a central domal uplift bound  
 272 by a conjugate set of lateral oblique reverse faults ( $\Delta h_{init} = 7$  mm, Fig. 4a) as shown in the Model R0  
 273 (Fig. 3a-c). In the second half of the experiment, following the static intrusion, dextral shearing is  
 274 applied. Accordingly, in the early intrusion stage there is no obvious fault formation (Fig. 4a). Once  
 275 shearing started diffuse deformation occur in a spindle-like surface area ( $d_{rel} = 11.4$ ; Fig. 4b) forming  
 276 a wider shear domain bound by transpressional faults. At a later stage of shearing ( $d_{rel} = 22.2$  mm;  
 277 Fig. 4c) a system of strike-slip faults consisting of two lateral and one central fault is cutting through  
 278 the uplifted domain. The finite fault pattern (Fig. 4d-f) is, in contrast to the model RS, characterized  
 279 by a wider strike-slip system encompassing the intrusion area and external transpressional faults  
 280 which have been active mainly during early stages of deformation.

281 The fault pattern in the syn-tectonic intrusion experiment, Model A2 (Fig. 5), initially evolves in a  
 282 similar fashion as in model A1. In the early deformational stage ( $d_{rel} = 3.9$ mm;  $V_{inj} = 4.9$ ml; Fig. 5a)  
 283 a diffuse spindle-like shear zone occurs encompassing the uplifting centre. With ongoing shearing  
 284 and intrusion ( $d_{rel} = 6.7$ mm;  $V_{inj} = 4.9$ ml; Fig. 5b) transpressional faults localize at the periphery of  
 285 the spindle-like area embracing the intrusion domain as well as Riedel shear in the centre. In the  
 286 late stage ( $d_{rel} = 27.8$ mm;  $V_{inj} = 35.0$ ml; Fig. 5c) deformation localizes into a narrow strike-slip fault  
 287 system cutting the roof over the intrusion. This set of parallel, locally transtensional faults cause the  
 288 depressing of the uplifted central domain (Fig. 5e). The finite fault pattern (Fig. 5d-f) shares  
 289 characters of the reference model RS (a central strike-slip fault system; Fig. 3d-f) and the pre-  
 290 tectonic model A1 (early stage transpressional faults swinging around the intrusion area; Fig. 4b).

291 The post-tectonic experiment, Model A3 (Fig. 6) consists again of two parts: In the first half, the  
 292 experiment follows according to the observations documented for the RS model ( $d_{rel} = 30$ mm; Fig.  
 293 3d-f) resulting in a system of strike-slip faults (Fig. 6a) at the start of intrusion. In the second half of  
 294 the experiment, static intrusion causes formation of new oblique reverse, lateral faults (in the upper  
 295 image half) but also the reactivation of inherited, lateral faults (in the upper image half;  $V_{inj} = 12.6$ -

32.2mm; Fig. 6b-c). Importantly, active faults in opposite corners of the intrusion show a synthetic sense including dextral and sinistral shear (Fig. 6b-c). Consequently, dextral displacement across inherited faults acquired in the first half of the experiment is now partly inverted. The finite fault pattern (Fig. 6d-f) is a composite of partly re-activated strike-slip faults similar to the reference model R0 (Fig. 3h-i) and new reverse faults bounding a central domal uplift.

### 3.2.2 Effect of deformation on intrusion shape

Among the three emplacement scenarios there is a significant variation regarding the final geometrical features of the intrusion described by the intrusion's absolute height ( $H$ ) and normalized amplitude ( $A$ ), its aspect ratio ( $r = \text{length}/\text{width}$ ) and the orientation of its long axis (angle  $\theta$ ). The intrusion models appear strongly deformed and asymmetric, revealing the tectonic impact during their emplacement, and have a systematic generic relation to the regional stress and finite strain fields (Fig. 7).

The sheared intrusion of Model A1 (pre-tectonic, Fig. 7a-d) is characterized by low height and amplitude ( $H_{A1} = 15 \text{ mm}$ ,  $A_{A1} = 0.38$ ), compared to intrusions from other scenarios. Its asymmetry is related to displacement along the crosscutting faults developing late in the experiment. The lower part of the intrusion represented e.g. by the contour level  $c_1 = 3\text{mm}$  shows a relatively high aspect ratio ( $r_1 = 2.7$ ) with the long axis of the intrusion forming a low angle of  $\theta_1 = 12^\circ$  to the shear zone. At higher contour levels the intrusion progressively elongates ( $r > 3$ ) and rotates antithetic (i.e. anticlockwise) with respect to the dextral simple shear (e.g.  $\theta_2 = 34^\circ$  at  $c_2 = 12\text{mm}$ ) becoming subparallel to the extension direction of the finite strain tensor (Fig. 8; A.2). The intrusion roof is sculpted by one central and two lateral dikes that represent silicone oil intruding upwards along the master fault (MF) and the lateral faults, obviously during the post-intrusion stage of the experiment.

The intrusion Model A2 (syn-tectonic, Fig. 7e-h) is characterized by an acute roof resulting in a significant height and amplitude ( $H_{A2} = 24\text{mm}$ ;  $A_{A2} = 0.6$ ; Fig. 7e-f) compared to intrusions from other scenarios. It shows a strong asymmetric wing shape with opposing orientation to the intrusion model A1. At lower levels, the intrusion has a high aspect ratio (e.g.  $r_1 = 2.5$ ) with the long axis almost

parallel to the shear zone ( $\theta_1 = 1^\circ$ ). Upwards, the intrusion progressively rotates synthetically into the orientation of Riedel shears (e.g.  $\theta_2 = -10^\circ$  at  $c_2 = 20\text{mm}$ ) while keeping its aspect ratio rather constant (Fig. 8; A.3). Lateral dikes flank the central upheaval with all of them exploiting faults formed during intrusion. The wing shape of the intrusion in association with scissor tailed and offset apophyses appears unique to this scenario.

The intrusion Model A3 (post-tectonic, Fig. 7 i-l) is characterized by a more domal shape with intermediate height and amplitude ( $H_{A3} = 22\text{ mm}$ ;  $A_{A3} = 0.55$ ). It appears sub-circular to gently elongated ( $r < 2$ ) and largely subparallel to the shear zone with no systematic change of aspect ratio and orientation with height (Fig. 8; A.4). The roof is rounded and sculpted by a central dike ( $r_2 = 1.9$  at  $c_2 = 19\text{mm}$ ) and two lateral dikes exploiting inherited structures, especially Riedel shears (Fig. 7i-j).

### 3.3 *Transtensional intrusion models (Group B)*

#### 3.3.1 *Effect of intrusion on fault evolution*

Transtensional intrusion experiments demonstrate, similarly to Group A, ongoing interactions developing between the intrusion and the fault pattern evolution for all three scenarios.

In the first half of the pre-tectonic intrusion experiment, Model B1, static intrusion takes place ( $V_{inj} = 37.7\text{ ml}$ ), causing a central domal surface uplift bound by a conjugate set of lateral oblique reverse faults ( $\Delta h_{init} = 7\text{ mm}$ ; Fig. 9a). In the second half of the experiment, transtension is applied and a diffuse spindle-like shear zone occurs ( $d_{rel} = 5.6\text{ mm}$ ; Fig. 9b) similar as in the pre-tectonic simple shear Model A1. With ongoing transtension, lateral oblique normal faults and oblique Riedel shears localize deformation ( $d_{rel} = 16.7\text{ mm}$ ; Fig. 9c) causing subsidence along the shear zone. The initial central dome is crosscut by a fault system (P and Y-shears) that links the lateral boundary faults, which remain active until the end of the experiment (Fig. 9c-f). Similar to the reference model (RT, Fig. 3g-i), Riedels form an en-echelon array of oblique normal faults within the basin (Fig. 9d). The finite deformation pattern of the surface is characterised by a well-defined elongated pull-apart basin (Fig. 9d-f). The domal uplift, caused by the initial intrusion, is overprinted and appears as a remaining

gentle uplift in the centre (Fig. 9e). Notably, the topographic expression of the pre-tectonic intrusion is much less than in the corresponding simple shear Model A1 (Fig. 4e).

The early stage of the syn-tectonic intrusion experiment, Model B2, is characterized by diffuse shear and Riedel shear formation ( $d_{rel} = 1.2$  mm;  $V_{inj} = 1.5$  ml; Fig. 10a). At an intermediate stage ( $d_{rel} = 8.3$  mm;  $V_{inj} = 10.5$  ml) and along with subsidence, the linkage of these Riedel shears forms a dominant fault zone that diverges from the strike of the basal shear zone to form a releasing bend centred on the intrusion domain (Fig. 10b). At a late stage ( $d_{rel} = 16.7$ ;  $V_{inj} = 21$ ; Fig. 10c) oblique normal faults bound the outer basin margins and curve towards the centre (Fig. 10c). As the master fault continues to propagate, it crosscuts and deforms the evolving basin. The finite fault pattern (Fig. 10d-e) is, in contrast to the reference model (RT, Fig. 3g-i), characterised by a more segmented and curved faults bounding the elongate basin with the deep central graben flanked by horst blocks.

The post-tectonic intrusion experiment, Model B3 (Fig. 11), is divided again into two parts: the first transtension phased follows the one described for Model RT (Fig. 3g-i), resulting in a fault-controlled, spindle-shaped pull-apart basin ( $d_{rel} = 30$ mm; Fig. 11a, d). Then static intrusion ( $V_{inj} = 13$  ml) starts to form a domal uplift, triggering the re-activation of the pre-existing faults (Fig. 11b). Similarly, as observed in Model A3, inherited faults are reactivated and partly inverted (Fig. 11b-c), however, no new faults are formed in Model B3; the master fault is re-activated in dextral sense while sinistral displacement occurs along inverted boundary faults ( $V_{inj} = 18.6$ ; Fig. 11c). The finite topography (Fig. 11d-e) directly reflects the intrusion at depth within the basin system (Fig. 11d-e).

### 3.3.2 Effect of deformation on intrusion geometry

The intrusion Model B1 (pre-tectonic, Fig. 12a-d) is like the corresponding Model A1 characterized by very low height and amplitude probably enhanced by post-emplacement flattening in the transtensional regime ( $H_{B1} = 5$  mm;  $A_{B1} = 0.13$ ). The intrusion's aspect ratio shows characteristic medium values with no systematic change with height (Fig. 13; A.5), varying from 1.8 at  $c_1 = 1$ mm (Fig. 12c) to 1.9 at  $c_2 = 3$ mm (Fig. 12d). The orientation of the intrusion, similar to Model A1, rotates from the base to the top antithetic (i.e. anti-clockwise) with respect to the dextral sense of transtensional

shear to become subparallel to the extension direction of the finite strain tensor (e.g.  $\theta_2 = 42^\circ$ ; Fig. 13). The intrusion's flat roof is sculpted by lateral dikes exploiting faults obviously developing during the post-emplacement deformation phase.

The intrusion Model B2 (syn-tectonic; Fig. 12e-h) similarly to Model A2 is characterised by an acute roof with significant height and amplitude ( $H_{B2} = 22$  mm;  $A_{B2} = 0.6$ ). The intrusion's base shows an intermediate aspect ratio of  $r_1 = 1.7$  with the long axis subparallel to the shear zone boundary (e.g.  $\theta_1 = -10^\circ$ ; Fig. 12g). Upwards, the intrusion rotates synthetically towards the maximum horizontal stress orientation,  $\sigma_{Hmax}$  (Fig. 12h; Fig. 13; A.6). This model bears a smooth roof top and lateral dikes flanking the central uplift. The asymmetric wing shape marked by a scissor tail apophyses that trails behind the intrusion are similarly observed for model A2 (Fig. 7e-h).

Finally, the intrusion Model B3 (post-tectonic, 11j-l) is, similar to A3, a sub-circular to slightly elongated intrusion of domal shape with intermediate height and amplitude ( $H_{B3} = 20$  mm;  $A_{B3} = 0.5$ ). At lower contour levels, the intrusion shows an aspect ratio of  $r_1 = 1.4$  with the long axis parallel to Riedel shears like in Model A3 (Fig. 12k; Fig. 13; A.7). The intrusion has an asymmetric roof of carrying a central dike ( $r_2 = 1.7$  at  $c_2 = 18$  mm) and two lateral dikes (Fig. 12l). The latter exploits inherited faults ( $\theta_2 = -11^\circ$ ; Fig. 8).

## 4 Discussion of experimental results

### 4.1 Synthesis and comparison of experimental results

#### 4.1.1 Controlling parameters on pluton emplacement

In this study we show that the timing of the magmatic emplacement with respect to the regional tectonic deformation is a controlling parameter on the finite pluton geometry and emplacement mode. Thus, the shape of the produced intrusions, based on the timing of their emplacement, is suggested as an effective diagnostic feature. The findings of this work support and extends the results of previous studies on static and syn-tectonic intrusion.

Based on our observations, the pluton shape is directly controlled by the evolving faults, for both groups in pre- and syn-tectonic scenarios. At the same time, strain localization on the weak body influences the upward fault propagation. Post-tectonic models are influenced and overprinted by the boundary conditions and indirectly by the inherited fault structures during their emplacement. According to our observations and in agreement with previous related studies (Román-Berdiel et al., 1997; 2000; Corti et al., 2005) local interactions between on-going fault propagation and magma uprising induce asymmetric intrusion shapes.

With respect to the kinematic boundary condition (transtension versus simple shear) we find quantitative differences in the final pluton shape with generally more elongated plutons in simple shear models. This contrasts the findings of Román-Berdiel et al. (2000) who studied the importance of the divergence angle,  $\alpha$ , in deformation styles of both surface and magma models. They concluded that for comparably low values of obliquity (i.e.  $\alpha = 15^\circ$ ) under transtension the fault pattern is similar to pure simple shear kinematics, therefore resulting in similar geometries for the syn-tectonic intrusions.

Previous studies show that variations in the displacement velocity and the intrusion rate control the final geometry and orientation of the syn-tectonic magmatic body emplaced in the upper crustal layer (Román-Berdiel et al., 1997; Corti et al., 2005). According to these studies, high horizontal-displacement or low intrusion rates result in normal pluton asymmetry with the pluton's long axis parallel to the velocity discontinuity (VD) zone, whereas low horizontal-displacement or high intrusion rates, generate plutons with reverse asymmetry (magmatic emplacement controlled by tensional faults). In this study the variation of the ratio between tectonic displacement rate and intrusion rate is constant. However, by varying the time of emplacement we also capture observations on the pluton's asymmetry with respect to the shear zone trend: Pre-tectonic models show a pluton orientation consistent with synthetic rotation and shearing: The long pluton axis form with the shear zone angles of  $\theta = 28^\circ$  (Model A1, Fig. 7c-d) and  $\theta = 42^\circ$  (Model B1, Fig. 12c-d) which is parallel to the extension direction in simple shear and transtension, respectively. In the contrary,

syn- and post-tectonic models from both experimental groups, show an antitetic orientation with their long axis forming low angles with the shear zone (Fig. 7, Fig. 12f,i). Only the syntectonic transtension Model B2 shows indications of stress-controlled emplacement with the pluton long axis parallel to the compression direction ( $s_1$  or  $sH_{max}$ ). All others are fault-controlled and follow Riedel shear orientation.

#### **4.1.2 Interactions between deformation and pluton emplacement**

The significant geometrical differences of the finite intrusions' shape observed among the emplacement scenarios (Fig. 7, Fig. 12) reveal strong interactions between deformation and intrusion emplacement (Román-Berdiel et al., 1997; Corti et al., 2005; Galland et al., 2007a; Montanari et al., 2010; Gomes et al., 2019). Our experimental results, in both simple and transtensional shear settings, show that pre- and syn-tectonic scenarios produce more elongated and fault-controlled intrusions in comparison to the less deformed post-tectonic intrusions characterised by low aspect ratios. The presence of intrusion causes regional surface uplift above the injection point and interferes with the fault structure evolution during their propagation.

In accordance to the study of Gomes et al. (2019), this study illustrates that the shear zone deformation can be significantly modified by rheological heterogeneities. A perturbation effect on fault evolution arises from the presence of a (pre-tectonic) viscous-weak bodies which does prohibit internal strain localization and causes faults in the brittle layer to be deflected. The pre-tectonic plutons, A1 and B1, with the gradual evolution of the post-emplacement shearing start to accumulate deformation in a ductile manner acquiring a sigmoidal (initially circular) shape of high aspect ratio and the lowest amplitude among all models (Fig. 7a-d, Fig. 12 a-d). This is very well shown from the shape analysis, where the lower levels of these intrusions are subparallel to the shear zone while the highest levels follow the finite stretching direction (Fig. 7c-d, Fig. 12c-d). The surface structures observed only for this model are acting separately over the domal uplift and not as one master fault (Fig. 4f). These above results seem compatible with the inferred observation on caldera collapse modelling and the case of strike-slip deformation of brittle layer containing a passive magmatic

chamber (Holohan et al., 2008), where the magmatic chamber showed a NE-SW pluton axis orientation, stretched approximately parallel to the extensional direction (in accordance to current study Models A1 and B1). The limitation of pre-tectonic models, by the fault structures developing subparallel to the boundary of the shear zone is an observation that is only attributed to the variations on the overburden thickness (Román-Berdiel et al., 1997). The presence of the weak body delays the upward propagation of the synthetic Riedel shears and results in a wider shear zone, in respect to its reference model (Fig. 3f, Fig. 4f). A feature that is inferred from the deformational response and the delay of the shear zone formation on the brittle surface, in comparison to the reference models (Fig. 3, Fig. 4, Fig. 9).

Syn-tectonic intrusions are clearly fault-controlled: faults control and confine the emplacement of the intrusions, resulting in narrow and acute pluton shape that follows the highly active master fault (e.g. Román-Berdiel et al., 1997; Corti et al., 2005; Mazzarini et al., 2010). Syn-tectonic models in simple shear deformation show the highest pluton amplitude among all models ( $A_{A2} = 0.6$ ; Table 3). Local fault control on the intrusions' boundaries and orientation is inferred from the shape analysis of the excavated intrusions.. Models A2 and B2, are initially orientated subparallel to the shear zone (intrusions' lower level), with very low long axis angles. Towards higher levels, their orientation rotates: In Model A2, the intrusion long axis seems to follow the helicoidal shape of Riedel shears (e.g. Dooley and Schreurs, 2012) and meet their surface orientation while it orients towards  $S_{Hmax}$  in Model B2.

The post-tectonic intrusions, Models A3 and B3, ascend in the absence of a regional tectonic stress field and pierce through the overburden creating local stresses. The shape analysis reveals a characteristic subcircular intrusion of an intermediate amplitude ( $A_{A3} = 0.55$ ;  $A_{B1} = 0.5$ ; Table 3) and with an analogous axis orientation to the syn-tectonic models (Fig. 7k-l, Fig. 12k-l). From the strain analyses it is inferred that in both settings, the uprising intrusions interferes and reactivates the pre-existing brittle structures (Fig. 6c, Fig. 11c).

As a second order feature, the dike system overprinting the intrusions, is observed and analysed upon excavation. Diking occurs locally and along fault structures and for all models, is developing either on the intrusion's flat roof top, as in the cases of pre- and post-tectonic emplacement models (Fig. 7a-b; i-j, Fig. 12a-b; i-j) or as a form of a sheared tail intrusion's extension, as in the case of the syn-tectonic Models A2 and B2 (Fig. 7e-f, Fig. 12e-f). Fault controlled diking in our models shares geometric and dynamic similarities with models of "reactive diapirism" in salt tectonic studies using similar rock analogue materials (e.g. Vendeville & Jackson, 1992; Koyi, 1998; Dooley & Hudec, 2020)".

Our models have shown that the pluton's geometry functions as an excellent first order discriminator for the timing of the intrusion with respect to tectonic activity. In addition, this study offers information on the surface deformation, often limited during field work due to the occurrence of natural (e.g. erosion) and tectono-magmatic processes. The diagnostic attributions serving as a tectono-magmatic guide are summarized in Table 3. **(Table 3 here)**

## *4.2 Model boundary conditions, simplifications and limitations*

### **4.2.1 Effect of the basal ductile shear zone on the emplacement process**

We use a ductile homogenous shear zone as a basal kinematic boundary condition, which mimics a natural mid-crustal shear zone at the brittle-viscous transition (Fig. 1B). Apart from distributing deformation within a well-confined shear zone, the viscous material may also influence the emplacement mechanisms as reported in previous studies (Román-Berdiel et al., 1997, 2000; Corti et al., 2005; Montanari et al., 2010; Mazzarini et al., 2010). In those models, the presence of a widespread ductile layer within the model crust is a pre-requisite to allow lateral flow and emplacement in laccolith style. It is suggested that for the syn-tectonic intrusion the rheological stratification causes a deeper level of emplacement with respect to purely brittle models where the model magma tends to rise to the surface. For our experiments, instead of a widespread ductile layer, we introduced a basal ductile band. Intrusions are allowed within the ductile band and above

the fixed injection tube. The effects described previously is similarly active in our setup with lateral intrusion aided by the ductile material.

#### 4.2.2 Ignoring thermal and strain-rate dependent effects on rheology.

The deformation in our experiments was accomplished by a quasi-stationary rheology including temperature- and strain rate-insensitive brittle and linear Newtonian viscous materials. Our modelling faces therefore some limitations regarding rheological principals (Corti et al., 2003). Magma cooling is considered in simplified way by choosing a relatively high viscosity of the model magma (see section 2.3). Thermal effects caused by the intrusion-related heating on the rheology of the crustal rocks were not taken into consideration for our modelling as for all other models of this type (Román-Berdiel et al., 1997; Corti et al., 2003; Galland et al., 2003, 2006, 2007; Montanari et al., 2010; Mazzarini et al., 2010). At shallow crustal levels as those targeted here, intrusion of rather small amounts of hot material into cold crust has likely a minor effect on the geotherm and thereby on the rheology in general. However, the brittle-ductile transition might be more sensitive to even small fluctuations in the geotherm caused by episodic heat advection by veining and long-term emplacement of the intrusion (e.g. Handy and Streit, 1999; Handy et al., 2001; Brown, 2013, Fig. 1B). Any modification of the rheology around the base of our models including temperature and strain-rate dependent viscosity changes or even switches in the dominant deformation mechanisms (and thereby the geometry of the brittle-viscous transition) is however beyond the scope of this modelling approach. While we consider this drawback of the method more significant at a small scale, numerical modelling might help in verifying the validity of our more stationary approach on a more regional scale.

#### 4.2.3 What drives deformation in the model versus nature?

In our experiments model magma is rising due to two different forces: pressure applied externally and internal buoyancy forces (e.g. Ribe and Davaille, 2013; Wouter et al., 2016). Though qualitative similar mechanisms act in nature the dynamic similarity is hard to verify. Pressure in the model is

controlled by the applied intrusion rate and decreases over an experimental run as the intrusion rate is kept constant while the volumetric fraction added to the growing intrusion decreases with  $1/t$  systematically. Given the geometric and kinematic similarities described above we suspect a realistic de-pressurization scenario in the model. However, given the lack of quantitative observations in nature a conclusion remains elusive. Buoyancy in the model is likely more important than in nature because the density ratio between PDMS and sand is low (1:1.7) while it may be closer to equality (1:1) or even  $>1$  (negatively buoyant) in nature, depending on magma composition. As we observe silicone dikes intruding the overburden in a similar fashion as in nature (e.g. roof dikes, see below), we suspect however, that buoyancy driven intrusion (i.e. diapirism) mimics residual melt injection driven by local pressure anomalies in the prototype.

### 4.3 Comparison with nature

Despite the limitations described above, analogue modelling is a powerful tool and here provides new insights on the reliability of the finite pluton shape as a diagnostic feature for constraining the temporal timing (pre-, syn- and post-tectonic) and kinematic conditions (tectonic setting) of shallow intrusions. To validate our findings, we compare our models here with six cases of well-defined natural examples, emplaced in simple shear and transtensional zones (Fig. 14).

#### 4.3.1 Natural examples of intrusions along simple shear zones

##### 4.3.1.1 Pre-tectonic intrusion

a) *Teixeira Pluton, NE Brazil* (Fig. 14a,d). This elongated ENE-trending batholith (80 km x 25 km) is situated in NE Brazil and within a zone that is defined by the E-W-trending Patos, the So Josèdos Cordeiros and the Juru shear zones (Fig. 14a). The pre-tectonic Teixeira batholith is a leucocratic granite to quartz-syenite in composition that shows a crystallization age of  $591 \pm 5$  Ma (U-Pb geochronology; Archanjo et al., 2008) which pre-dates deformation. The batholith fabrics, determined by anisotropy of magnetic susceptibility (AMS) and mineral shape preferred orientation, support a pre-tectonic batholith emplacement scenario (Archanjo

et al., 2008). This natural example carries similar features to the pre-tectonic model A1 of this study (Fig. 7a-d). The pluton is characterised by high aspect ratio ( $r > 5$ ) and is orientated at an acute angle of  $\theta = 15^\circ$  to the shear zones. The comparatively high aspect ratio and low obliquity of the pluton points to a high degree (larger than in our experiments) of dextral simple shear (Fig. 14a).

*b) Tazenakht Pluton, southern Morocco.* The pluton's deformation follows its emplacement within a left lateral strike slip fault, running along its northern side (Ennih and Liegeois, 2001; Gasquet et al., 2008). The boundaries developing between the fault structure and the intrusion boundaries are sharp. The pluton was probably subject to shear and rotation during the younger deformation event. This natural example is characterised by high axis ratio ( $r = 1.6$ ) and the pluton's long axis forms an angle of  $\theta = 29^\circ$  with the shear zone pointing to similar amounts of post-emplacement shear as in Model A1. The local presence of dykes and the geometrical features of the pluton are also similar to those observed for the Model A1.

#### **4.3.1.2 Syn-tectonic intrusion**

*a) Cabeza de Araya Pluton, western Spain* (Fig. 14b,e). The plutons of the Central Extremadura batholith in the Iberian Massif (Fernández and Castro, 1999) is a natural example of syn-tectonic plutonism. This natural example was imposed to tectonic deformation during its emplacement along a right-lateral shear zone (Vigneresse and Bouchez, 1997; Fernández and Castro, 1999; Corti et al., 2005, Castro, 1985). The pluton shows an aspect ratio of  $r = 2.7$ , similarly observed in Model A2 ( $r = 2.5$ ; Fig. 7g,h). The long axis has an angle of  $\theta = 45^\circ$  which is significantly more oblique compared to our models and would be parallel to the theoretical compression direction (NW-SE direction, Fig. 14b) if an E-W shear zone trend is assumed. At the same time, the pluton parallels faults that could be interpreted as Riedel shears similar as in our Model A2 if a more ESE-WNW orientation of the shear zone is assumed.

in addition to this example, there are other important natural examples of syn-tectonic intrusion emplacement that show similarities to our observations: b) *The Karawanken pluton* (Visonà and Zanferrari, 2000; Rosenberg, 2004); c) *The Lizio pluton* (Román-Berdiel et al., 1997; Fernandez and Castro, 1999; Corti et al., 2005); d) *Syn-tectonic magmatism along the Periadriatic Fault System* (Rosenberg, 2004).

#### 4.3.1.3 Post-tectonic intrusion

a) *Vila Pouca de Aguiar pluton, northern Portugal* (Fig. 14c,f). This is a natural example of a post-tectonic granitic intrusion that is emplaced after the main left-lateral shear phase event (Sant'Ovaia et al., 2000). It is suggested that the first to be emplaced and the least evolved granite type (Vila Pouca de Aguiar Granite) upwelled from the local, NE-trending fault-zone, acting as a dike, and formed a thin sill where NE-directed magma flow was dominant. In this case, the pre-existing features exert a major role during emplacement leading to the roughly alignment of the intrusion with the shear zone ( $\theta = -4^\circ$ ; Fig. 14f). As in Model A3 the pluton's aspect ratio is rather low ( $r = 1.9$ )

### 4.3.2 Natural examples for intrusion into transtensional shear zones

#### 4.3.2.1 Pre-tectonic intrusion

a) *Eğrigöz pluton, western Anatolia* (Fig. 14g,j). This natural example regards a N-S elongated (40x15 km) granite body ( $20.5 \pm 1.1$ - $18.9 \pm 1.2$  Ma.; Catlos et al., 2012), situated in the northern Menderes metamorphic core complex and covering an area of 330 Km<sup>2</sup>. Its geometrical features show a relatively high aspect ratio of  $r = 2.6$  and a high obliquity of  $\theta = 46^\circ$  with respect to model B1 and most comparable to our experimental observations made for the higher contour levels of the strongly deformed pre-tectonic Model B1 ( $r = 1.9$ ;  $\theta = 42^\circ$ ; Fig. 12d; Table 3). The 20km-long, NE-striking Gerni shear zone is closely linked to the pulses of magmatic activity and assumed to have propagated immediately following the emplacement of the Eğrigöz pluton. Stress tensor results of the Eğrigöz pluton indicate that the shear zone has been predominant under NE-SW-trending extension. The presence of

the aplitic and pegmatitic dikes along the periphery and structurally upper parts of the pluton (Erkül et al., 2017) are rather common and similarly reproduced during the analogue Model B1 experiment (Fig. 12a-b). In addition to this example, more plutons are registered carrying similar diagnostic features of pre-tectonic emplacement mode: b) *The Totoltepec Pluton, southern Mexico* (Kirsch et al., 2013); c) *The Devonian granitoid of Pampa de Achala, Central Argentina* (Simpson et al., 2001); d) *The Koyunoba pluton, western Turkey* (Erkül et al., 2017).

#### 4.3.2.2 Syn-tectonic intrusion

- a) *Monzoni Intrusive Complex, NE Italy* (Fig. 14h,e). This 4 km-long intrusion situated in the central Dolomites has an excellent three-dimensional exposure (Fig. 1, Vardabasso, 1930; Bonadiman et al., 1994; Abbas et al., 2018; Michail, 2018). However, due to contact metamorphism around the pluton and the syn-metamorphic thermally driven fluid circulation, field observations are very limited, and still there is very poor knowledge of the kinematic setting. Based on analogue modelling observations, we here infer information about the fault structures and kinematics in the eroded crustal volumes above and around the pluton. Pluton's emplacement was in the Middle Triassic which was characterized regionally by tectonics along a left-lateral shear zone, however the temporal relation of the intrusion to tectonics is still under discussion. According to our model observations, this pluton exhibits diagnostic characteristics of syn- to late tectonic intrusion. The pluton's long axis trends with an angle of  $\theta = -14^\circ$  to the shear zone boundary and therefore roughly parallel to the maximum horizontal compression assuming a transtensional regime. It shows an aspect ratio of  $r = 2$  (Fig. 14k) comparable to the Model B2 ( $-10 < \theta < -19^\circ$ ;  $r = 1.7$ ; Fig. 12g-h). Syn-magmatic dike swarms occur (Doglioni, 1983; Blendinger, 1985; Abbas et al., 2018) while the pluton carries a NE–SW striking apophysis that trails the intrusion at its SW boundary again similar to Model B2. Further natural examples of syn-tectonic emplacement modes are b) *The Mortagne pluton, France* (Román-Berdiel et al., 1997); c) *The Los Pedroches pluton, southern Spain* (Aranguren et al., 1997; Román-Berdiel et al., 2000); d) *The Jihlava*

intrusion, Bonernian Massif (Verner et al., 2006); e) *The Hombreiro pluton, NW Spain* (Román-Berdiel et al., 2000); f) *The Gulf of Aden Ridge* (Corti et al., 2003).

#### 4.3.2.3 Post-tectonic intrusion

a) *La Tojiza Pluton, NW Spain* (Fig. 14i,l). The La Tojiza granite is cropping out in the Mondoñedo Nappe Domain (Fig. 14c) and according to geochronological data it consists with a U–Pb age of  $295 \pm 2$  Ma (Fernández-Suárez et al., 2000). This post-tectonic association is composed of granite–granodiorite–tonalite–monzogranite intrusions. The intrusion reactivated the inherited transtensional tectonic structures, leading to the emplacement and formation of a sub-circular pluton of 16 km-diameter (Aranguren et al., 2003). Its thickness is estimated of 1 km and the root zone is located at its eastern border. The pluton shows an axis trend of  $\theta = -6^\circ$  sub-parallel to the shear zone with a low pluton's aspect ratio  $r = 1.2$  (Fig. 14l). Most of the observed aplitic dikes are present on the roof of the pluton and oblique to the magnetic lineation. These features are in great accordance to the lower contour levels of the post-tectonic Model B3 ( $\theta = 0^\circ$ ;  $r = 1.4$ ; Fig. 12k-l). Similar natural example of post-tectonic emplacement is b) *The Plasenzuela Intrusion, NW Spain* (Fernandez and Castro, 1999) which is characterised by a well-defined rounded pluton shape of low aspect ratio ( $r \sim 1$ ).

## 4 Conclusions

This study provides new insights into pluton emplacement in tectonically active regions and their diagnostic potential. Three scenarios on pluton emplacement (pre-, syn- and post-tectonic) in two different tectonic settings (simple shear vs. transtension) are here presented. The intrusion shapes (characterized by the aspect ratio, principal axis trend/elongation, amplitude) and the model surface deformation are quantified, providing useful insights for the understanding of the interactions occurring between tectonics and magmatism.

According to our analysis strong interactions between tectonics and magma emplacement result in characteristic fault pattern and pluton shapes:

Pre-tectonic intrusion models accumulate regional strain during shearing of the intrusion, resulting in the delay and deviation of the brittle structures during their up-ward propagation. Here, the final shear zone appears wider than the respective reference model and crosscut but more than one well-defined fault. Syn-tectonic emplacement causes the major boundary faults to swing around the intrusion forming a narrow fault-controlled pull-apart basin overprinted by the master fault in a late stage. Inversion of the sense of shear along lateral faults occurs during post-tectonic intrusion in the vicinity of the pluton reactivating faults to accommodate space.

Plutons in the different emplacement scenarios show diagnostic differences in their shape: The pre-tectonic intrusions appear strongly elongated parallel to the extension field with the lowest amplitude (especially in transtension) and the highest aspect ratios (especially in simple shear). Syn-tectonic models are characterised by high amplitude and moderate aspect ratios. They bear acute roofs, oriented parallel to Riedel shears (in simple shear) or the compression direction (in transtension) and show typical scissor-tail apophyses railing the main body of intrusion. The sub-circular post-tectonic models show the lowest aspect ratios, medium amplitudes and explore inherited structures which let them follow Riedel shear orientation.

The applicability of the diagnostic attributes proposed by our modelling is tested against well constrained natural case studies. It is suggested that they serve as a model-based guide to differentiate between tectonic regimes and relative timing in tectonically and magmatically active regions.

## Data Availability

Supplementary data to this article can be found at: <http://doi.org/10.5880/GFZ.4.1.2021.004>.

## 5 Acknowledgments

The experiments were performed at the HelTec - Helmholtz Laboratory for Tectonic Modelling of the Helmholtz Centre Potsdam - German Research Centre for Geosciences (GFZ), in Potsdam (Germany). The authors wish to thank F. Neumann and T. Ziegenhagen (GFZ German Research Centre for Geosciences) for their technical support and engineering, T. Dooley for his valuable and constructive review, T. Román-Berdiel for her valuable reviews on a previous version of the manuscript, as well as E. Carminati (*Sapienza University*), M. Mattei (*Roma Tre University*) and C. Bonadiman (University of Ferrara) for their constructive discussions and contributions. Part of this research was funded by the IUSS-PhD mobility grant (University of Ferrara). This project has been supported by the Deutsche Forschungsgemeinschaft (DFG) through grant CRC 1114 "Scaling Cascades in Complex Systems", Project Number 235221301, Project B01. and EPOS – the European Plate Observing System.

## 6 References

- Abbas, H., Michail, M., Cifelli, F., Mattei, M., Gianolla, P., Lustrino, M., Carminati, E., 2018. Emplacement modes of the Ladinian plutonic rocks of the Dolomites: Insights from anisotropy of magnetic susceptibility. *J. Struct. Geol.* 113, 42-61. <https://doi:10.1016/j.jsg.2018.05.012>.
- Adam, J., Urai, J.L., Wieneke, B., Oncken, O., Pfeiffer, K., Kukowski, N., Lohrmann, J., Hoth, S., Van der Zee, W., Schmatz, J., 2005. Shear localisation and strain distribution during tectonic faulting - new insights from granular-flow experiments and high-resolution optical image correlation techniques. *J. Struct. Geol.* 27, 283-301. <https://doi:10.1016/j.jsg.2004.08.008>.
- Aranguren, A., Cuevas, J., Tubia, J.M., Román-Berdiel, T., Casas-Sainz, A., Casas-Ponsati, A., 2003. Granite laccolith emplacement in the Iberian arc: AMS and gravity study of the La Tojiza pluton (NW Spain). *J. Geol. Soc. London.* 160, 435–445. <https://doi:10.1144/0016-764902-079>

- 699 Bartlett, W.L., Friedman, M., Logan, J.M., 1981. Experimental folding and faulting of rocks under  
700 confining pressure Part IX. Wrench faults in limestone layers. *Tectonophysics* 79, 255–277.  
701 [https://doi:10.1016/0040-1951\(81\)90116-5](https://doi:10.1016/0040-1951(81)90116-5).
- 702 Benn, K., Odonne, F., De Saint Blanquat, M., 1998. Pluton emplacement during transpression in  
703 brittle crust: New views from analogue experiments. *Geology* 26, 1079–1082.  
704 [https://doi:10.1130/0091-7613\(1998\)026<1079: PEDTIB>2.3.CO](https://doi:10.1130/0091-7613(1998)026<1079: PEDTIB>2.3.CO).
- 705 Benn, K., Odonne, F., Lee, S.K.Y., Darcovich, K., 2000. Analogue scale models of pluton emplace-  
706 ment during transpression in brittle and ductile crust. *Trans. R. Soc. Edinb. Earth Sci.* 91, 111–  
707 121. <https://doi:10.1130/0-8137-2350-7.111>.
- 708 Blendinger, W., 1985. Middle Triassic strike-slip tectonics and igneous activity of the Dolomites  
709 (southern Alps). *Tectonophysics* 113, 105–121. [http://dx.doi.org/10.1016/0040-](http://dx.doi.org/10.1016/0040-1951(85)90112-X)  
710 [1951\(85\)90112-X](http://dx.doi.org/10.1016/0040-1951(85)90112-X).
- 711 Bonadiman, C., Coltorti, M., Siena, F., 1994. Petrogenesis and T-fO<sub>2</sub> estimates of Mt. Monzoni  
712 Complex (central Dolomites, Southern Alps); a Triassic shoshonitic intrusion in a transcurrent  
713 geodynamic setting. *Eur. J. Mineral.* 6, 943–966.
- 714 Brown, M., 2013. Granite: From genesis to emplacement. *Geol. Soc. Am. Bull.* 125, 1079–1113.  
715 <https://doi:10.1130/B30877.1>.
- 716 Burov, E., Jaupart, C., and Guillou-Frottier, L., 2003. Ascent and emplacement of buoyant magma  
717 bodies in brittle-ductile upper crust. *J. Geophys. Res.* 108. [https://doi: 10.1029/2002JB001904](https://doi:10.1029/2002JB001904)
- 718 Catlos, E. J., Jacob, L., Oyman, T., & Sorensen, S., 2012. Long-term exhumation of an Aegean  
719 metamorphic core complex granitoids in the Northern Menderes Massif, western Turkey. *Amer-*  
720 *ican Journal of Science*, 312(5), 534-571.

- 721 Castro, A., Fernandez, C., 1998. Granite intrusion by externally induced growth and deformation of  
 722 the magma reservoir, the example of the Plasenzuela pluton, Spain. *J. Struct. Geol.* 20, 1219–  
 723 1228. [https://doi.org/10.1016/S0191-8141\(98\)00056-X](https://doi.org/10.1016/S0191-8141(98)00056-X).
- 724 Corti, G., Bonini, M., Conticelli, S., Innocenti, F., Manetti, P., Sokoutis, D., 2003. Analogue modelling  
 725 of continental extension: A review focused on the relations between the patterns of deformation  
 726 and the presence of magma. *Earth-Science Rev.* 63, 169–247. [https://doi.org/10.1016/S0012-](https://doi.org/10.1016/S0012-8252(03)00035-7)  
 727 8252(03)00035-7.
- 728 Corti, G., Moratti, G., Sani, F., 2005. Relations between surface faulting and granite intrusions in  
 729 analogue models of strike-slip deformation. *J. Struct. Geol.* 27, 1547–1562.  
 730 <https://doi.org/10.1016/j.jsg.2005.05.011>.
- 731 De Saint Blanquat, M., Horsman, E., Habert, G., Morgan, S., Vanderhaeghe, O., Law, R., Tikoff, B.,  
 732 2011. Multiscale magmatic cyclicity, duration of pluton construction, and the paradoxical rela-  
 733 tionship between tectonism and plutonism in continental arcs. *Tectonophysics* 500, 20–33.  
 734 <https://doi.org/10.1016/j.tecto.2009.12.009>.
- 735 Doglioni, C., 1983. Duomo medio-Triassico nelle Dolomiti. *Rend. della Soc. Geol. Ital.* 6, 13–16
- 736 Dooley, T. P., Hudec, M. R., 2020. Extension and inversion of salt-bearing rift systems. *Solid Earth*  
 737 11, 1187–1204, <https://doi.org/10.5194/se-11-1187-2020>, 2020.
- 738 Dooley, T.P., Schreurs, G., 2012. Analogue modelling of intraplate strike-slip tectonics: A review  
 739 and new experimental results. *Tectonophysics* 790, 574–575, 1–71.  
 740 <https://doi.org/10.1016/j.tecto.2012.05.030>.
- 741 Erkül F., Erkül, S.T., Manap, H.S., Çolak, C., 2017. An extensional and transtensional origin of elon-  
 742 gated magmatic domes and localised transfer faults in the northern Menderes metamorphic

- 743 core complex, western Turkey. *Geodinamica Acta* 29, 139–159.  
744 <https://doi.org/10.1080/09853111.2017.1343523>.
- 745 Ennih, N., Liégeois, J.P., 2001. The Moroccan Anti-Atlas: The West African craton passive margin  
746 with limited Pan-African activity. Implications for the northern limit of the craton. *Precambrian*  
747 *Res.* 112, 289–302. [https://doi.org/10.1016/S0301-9268\(01\)00195-4](https://doi.org/10.1016/S0301-9268(01)00195-4).
- 748 Fernández, C., Castro, A., 1999. Pluton accommodation at high strain rates in the upper continental  
749 crust. The example of the Central Extremadura batholith, Spain. *J. Struct. Geol.* 21, 1143–1149.  
750 [https://doi.org/10.1016/S0191-8141\(99\)00086-3](https://doi.org/10.1016/S0191-8141(99)00086-3).
- 751 Fernández, C., Castro, A., 1999. Pluton accommodation at high strain rates in the upper continental  
752 crust. The example of the Central Extremadura batholith, Spain. *J. Struct. Geol.* 21, 1143–1149.  
753 [https://doi.org/10.1016/S0191-8141\(99\)00086-3](https://doi.org/10.1016/S0191-8141(99)00086-3).
- 754 Fernández-Suárez, J., Dunning, G.R., Jenner, G.A., and Gutiérrez-Alonso, G., (2000). Variscan col-  
755 lisional magmatism and deformation in NW Iberia: constraints from U-Pb geochronology of  
756 granitoids. *J. Geol. Soc.* 157, 565–576.
- 757 Ferré, E.C., Galland, O., Montanari, D., Kalakay, T.J., 2012. Granite magma migration and emplace-  
758 ment along thrusts. *Int. J. Earth Sci.* 101, 1673–1688. <https://doi.org/10.1007/s00531-012-0747-6>.
- 759 Fossen, H., Teyssier, C., Whitney, D.L., 2013. Transtensional folding. *J. Struct. Geol.* 56, 89–102.  
760 <https://doi.org/10.1016/j.jsg.2013.09.004>.
- 761 Galland, O., Holohan, E., van Wyk de Vries, B., Burchardt, S., 2015. Laboratory Modelling of Vol-  
762 cano Plumbing Systems: A Review. In: Breitzkreuz C., Rocchi S. (eds) *Physical Geology of Shal-*  
763 *low Magmatic Systems*. Adv. Volcanol. Springer, 1–68. [https://doi.org/10.1007/11157\\_2015\\_9](https://doi.org/10.1007/11157_2015_9).

- 764 Galland, O., Cobbold, P.R., de Bremond d'Ars, J., Hallot, E., 2007b. Rise and emplacement of  
 765 magma during horizontal shortening of the brittle crust: Insights from experimental modeling. *J.*  
 766 *Geophys. Res. Solid Earth* 112, 1–21. <https://doi:10.1029/2006JB004604>.
- 767 Galland, O., Cobbold, P.R., Hallot, E., de Bremond d'Ars, J., Delavaud, G., 2006. Use of vegetable  
 768 oil and silica powder for scale modelling of magmatic intrusion in a deforming brittle crust. *Earth*  
 769 *Planet. Sci. Lett.* 243, 786–804. <https://doi:10.1016/j.epsl.2006.01.014>.
- 770 Galland, O., de Bremond d'Ars, J., Cobbold, P.R., Hallot, E., 2003. Physical models of magmatic  
 771 intrusion during thrusting. *Terra Nova* 15, 405–409. [https://doi:10.1046/j.1365-](https://doi:10.1046/j.1365-3121.2003.00512.x)  
 772 [3121.2003.00512.x](https://doi:10.1046/j.1365-3121.2003.00512.x).
- 773 Galland, O., Hallot, E., Cobbold, P.R., Ruffet, G., de Bremond d'Ars, J., 2007a. Volcanism in a  
 774 compressional Andean setting: A structural and geochronological study of Tromen volcano  
 775 (Neuquén province, Argentina). *Tectonics* 26. <https://doi:10.1029/2006TC002011>.
- 776 Gasquet, D., Ennih, N., Liegeois, J.P., Soulaïmani, A., Michard, A., 2008. The Pan-African Belt, in:  
 777 *Continental Evolution: The Geology of Morocco. Lecture Notes in Earth Sciences.* 33–64.
- 778 Gomes, A.S., Rosas F.M., Duarte J.C., Schellart W.P., Almeida J., Tomás, R., Strak, V., 2019. An-  
 779 alogue modelling of the brittle shear zone propagation across upper crustal morpho-rheological  
 780 heterogeneities. *J. Struct. Geol.* 126, 175–197. <https://doi:10.1016/j.jsg.2019.06.004>.
- 781 Handy, M.R., Mulch, A., Rosenau, M. and Rosenberg, C. L., 2001. The role of fault zones and melts  
 782 as agents of weakening, hardening and differentiation of the continental crust: a synthesis.  
 783 *Geol. Soc. Spec. Publ.*, 186, 305–332. <https://doi:10.1144/GSL.SP.2001.186.01.18>.
- 784 Handy, M.R., Streit, J.E., 1999. Mechanics and mechanisms of magmatic underplating: Inferences  
 785 from mafic veins in deep crustal mylonite. *Earth Planet. Sci. Lett.* 165, 271–286.  
 786 [https://doi:10.1016/S0012-821X\(98\)00272-6](https://doi:10.1016/S0012-821X(98)00272-6).

- Holoman, E.P., van Wyk de Vries, B., Troil, V.R., 2008. Analogue models of caldera collapse in strike-slip tectonic regimes. *Bull. Volcanol.* 70, 773–796. <https://doi.org/10.1007/s00445-007-0166-x>. Hubbert, M.K., 1937. Theory of scalable models as applied to the study of geologic structures. *Geol. Soc. Am. Bull.* 48, 1459–1520. doi:10.1130/GSAB-48-1459.
- Hutton, D.H.W., Reavy, R.J., 1992. Strike-slip tectonics and granite petrogenesis. *Tectonics* 11, 960–967. <https://doi.org/10.1029/92TC00336>.
- Hutton, D.H.W., 1988. Granite emplacement mechanisms and tectonic controls: inferences from deformation studies. *Trans. R. Soc. Edinb. Earth Sci.* 79, 245–255. <https://doi.org/10.1017/S0263593300014255>.
- Kirsch, M., Keppie, J.D., Murphy, J.B., Lee, J.K.W., 2013. Arc plutonism in a transtensional regime: The late Palaeozoic Totoltepec pluton, Acatlán Complex, southern Mexico. *Int. Geol. Rev.* 55, 263–286. <https://doi.org/10.1080/00206814.2012.693247>.
- Klinkmüller, M., Schreurs, G., Rosenau, M., Kemnitz, H., 2016. Properties of granular analogue model materials: A community wide survey. *Tectonophysics* 684, 23–38. <https://doi.org/10.1016/j.tecto.2016.01.017>.
- Koptev, A., Burov, E., Gerya, T., Le Pourhiet, L., Leroy, S., Calais, E., Jolivet, L., 2017. Plume-induced continental rifting and break-up in ultra-slow extension context: Insights from 3D numerical modeling. *Tectonophysics*. Article in press. <https://doi.org/10.1016/j.tecto.2017.03.025>.
- Koyi, H., 1998. The shaping of salt diapirs, *Journal of Structural Geology*, Volume 20, Issue 4, 1998, Pages 321-338, [https://doi.org/10.1016/S0191-8141\(97\)00092-8](https://doi.org/10.1016/S0191-8141(97)00092-8).
- Verner, K., Žák J., Hrouda, F., Holub, F., 2006. Magma emplacement during exhumation of the lower- to mid-crustal orogenic root: the Jihlava syenitoid pluton, Moldanubian Unit, Bohemian Massif. *J Struct Geol.* 28, 1553–1567.

- 810 Mandal, N., Chakraborty, C., 1990. Strain fields and foliation trajectories around pre-, syn-, and post-  
811 tectonic plutons in coaxially deformed terranes. *Geol. J.* 25, 19–33.  
812 <https://doi.org/10.1002/gj.3350250103>.
- 813 Mazzarini, F., Musumeci, G., Montanari, D., Corti, G., 2010. Relations between deformation and  
814 upper crustal magma emplacement in laboratory physical models. *Tectonophysics* 484, 139–  
815 146. <https://doi.org/10.1016/j.tecto.2009.09.013>.
- 816 Michail, M., 2018. Emplacement of the middle Triassic Monzoni Intrusive Complex (Dolomites, Italy):  
817 Insights from analogue models and field observations. PhD Thesis. University of Ferrara, Italy,  
818 pp. 215.
- 819 Michail, M., Rudolf, M., Rosenau, M., Riva A., Gianolla, P., Coltorti, M., 2021. Digital image correla-  
820 tion data from analogue modelling experiments addressing magma emplacement along simple  
821 shear and transtensional fault zones. *GFZ Data Services*.  
822 <http://doi.org/10.5880/GFZ.4.1.2021.004>.
- 823 Montanari, D., Corti, G., Sani, F., Del Ventisette, C., Bonini, M., Moratti, G., 2010. Experimental  
824 investigation on granite emplacement during shortening. *Tectonophysics* 484, 147–155.  
825 <https://doi.org/10.1016/j.tecto.2009.09.010>.
- 826 Paterson, S.R., Okaya, D., Memeti, V., Economos, R., Miller, R.B., 2011. Magma addition and flux  
827 calculations of incrementally constructed magma chambers in continental margin arcs: Com-  
828 bined field, geochronologic, and thermal modeling studies. *Geosphere* 7, 1439–1468.  
829 <https://doi.org/10.1130/GES00696.1>.
- 830 Paterson, S.R., Schmidt, K.L., 1999. Is there a close relationship between faults and plutons? *J.*  
831 *Struct. Geol.* 21, 1131–1142.

- Paterson, S.R., Tobisch, O.T., 1988. Using pluton ages to date regional deformations: problems with commonly used criteria. *Geology* 16, 1108–1111.
- Petford, N., Cruden, A.R., McCaffrey, K.J., Vigneresse, J.-L., 2000. Granite magma formation, transport and emplacement in the Earth's crust. *Nature* 408, 669–673. <https://doi.org/10.1038/35047000>.
- Ramberg, H., 1981. Gravity, deformation and the Earth's crust: In Theory, Experiments, and Geological Application. London, Academic Press, 452.
- Ribe, N.M., Davaille, A., 2013. Dynamical similarity and density (non-) proportionality in experimental tectonics. *Tectonophysics* 608, 1371–1379. <https://doi.org/10.1016/j.tecto.2013.06.005>.
- Riedel, W., 1929. Zur Mechanik geologischer Brucherscheinungen. *Zentralblatt Mineral., Geol. u. Paläont. B*, 354–368.
- Ritter, M.C., Leever, K., Rosenau, M., Oncken, O., 2016. Scaling the sandbox-Mechanical (dis) similarities of granular materials and brittle rock. *Journal of Geophysical Research: Solid Earth*, 121(9), 6863–6879. <https://doi.org/10.1002/2016jb012915>.
- Román-Berdiel, T., 1999. Geometry of granite emplacement in the upper crust: contributions of analogue modelling, in: Castro, A., Fernandez, C., Vigneresse, J.L. (Eds.), *Understanding granites: Integrating new and classical techniques*. Geological Society, London, Special Publications. 168. 77–94. <https://doi.org/10.1144/GSL.SP.1999.168.01.06>.
- Román-Berdiel, T., Aranguren, A., Cuevas, J.L., Tubia, J.M., Gapais, D., Brun, J.-P., 2000. Experiments on granite intrusion in transtension, in: Vendeville, B., Mart, Y., Vigneresse, J.L. (Eds.), *Salt, Shale and Igneous Diapirs in and around Europe*. Geological Society, London, Special Publications. 174. 21–42. <https://doi.org/10.1144/GSL.SP.1999.174.01.02>.

- Roman-Berdiel, I., Gapais, D., Brun, J.P., 1997. Granite intrusion along strike-slip zones in experiment and nature. *Am. J. Sci.* 297, 651–678. <https://doi:10.2475/ajs.297.6.651>.
- Rosenberg, C.L., 2004. Shear zones and magma ascent: A model based on a review of the Tertiary magmatism in the Alps. *Tectonics* 23, 21. <https://doi:10.1029/2003TC001526>.
- Rosenau et al. (2018): Ring-shear test data of quartz sand G12 used for analogue experiments in the Helmholtz Laboratory for Tectonic Modelling (HelTec) at the GFZ German Research Centre for Geosciences in Potsdam. GFZ Data Services. <https://doi:10.5880/GFZ.4.1.2019.003>.
- Rudolf, M., Boutelier, D., Rosenau, M., Schreurs, G., Oncken, O., 2016. Rheological benchmark of silicone oils used for analog modeling of short- and long-term lithospheric deformation. *Tectonophysics* 684, 12–22. <https://doi:10.1016/j.tecto.2015.11.028>.
- Sant’Ovaia, H., Bouchez, J.L., Noronha, F., Leblanc, D., Vigneresse, J.L., 2000. Composite-laccolith emplacement of the post-tectonic Vila Pouca de Aguiar granite pluton (northern Portugal): A combined AMS and gravity study. *Trans. R. Soc. Edinb. Earth Sci.* 91, 123–137. <https://doi:10.1017/S026359330000732X>.
- Schellart, W.P., Strak, V., 2016. A review of analogue modelling of geodynamic processes: Approaches, scaling, materials and quantification, with an application to subduction experiments. *J. Geodyn.* 100, 7-32. <https://doi:10.1016/j.jog.2016.03.009>.
- Schöpfer, M.P.J., Steyrer, H.P., 2001. Experimental modeling of strike-slip faults and the self-similar behavior. *Geol. Soc. Am. Mem.* 193, 21–27. <https://doi:10.1130/0-8137-1193-2.21>.
- Schreurs, G., 2003. Fault development and interaction in distributed strike-slip shear zones: an experimental approach, in: Storti, F., Holdsworth, R.E., Salvini, F. (Eds.), *Intraplate Strike-Slip deformation belts*. Geological Society, London, Special Publications. 35–52. <https://doi:10.1144/GSL.SP.2003.210.01.03>.

- Shinevar, W.J., Benn, M.D., Hirth, G., 2015. Compositional dependence lower crustal viscosity, *Geophys. Res. Lett.* 42, 8333–8340. <https://doi.org/10.1002/2015GL065459>.
- Simpson, C., Whitmeyer, S.J., De Paor, D., Gromet, L.P., Miro, R., Krol, M., and Short, H., 2001. Sequential ductile to brittle reactivation of major fault zones along the accretionary margin of Gondwana in Central Argentina. In: Holdsworth, R.E. et al. (eds.) *The Nature and Tectonic Significance of Fault Zone Weakening*. Geol. Soc. London, Special Publications, 186, 233-255.
- Sloman, L., 1989. Triassic shoshonites from the Dolomites, northern Italy: alkaline arc rocks in a strike-slip setting. *J. Geophys. Res.* 94, 4655–4666.
- Vardabasso, S., 1930. Carta geologica del territorio eruttivo di Predazzo e Monzoni: ufficio Idrografico del Magistrato alle Acque di Venezia. scale 1, 25000 2 sheet.
- Vendeville, B.C., Jackson, M.P.A., 1992, The fall of diapirs during thin-skinned extension, *Marine and Petroleum Geology*, 9, 4, 354-371. [https://doi.org/10.1016/0264-8172\(92\)90048-J](https://doi.org/10.1016/0264-8172(92)90048-J).
- Vigneresse, J.L., 1995. Control of granite emplacement by regional deformation. *Tectonophysics* 249, 173–186. [https://doi.org/10.1016/0040-1951\(95\)00004-7](https://doi.org/10.1016/0040-1951(95)00004-7).
- Vigneresse, J.L., Bouchez, J.L., 1997. Successive Granitic Magma Batches During Pluton Emplacement: the Case of Cabeza de Araya (Spain). *J. Petrol.* 38, 1767–1776. <https://doi.org/10.1093/petroj/38.12.1767>.
- Visonà, D., Zanferrari, A., 2002. Some constraints on geochemical features in the Triassic mantle of the easternmost Austroalpine-Southalpine domain: evidence from the Karawanken pluton (Carinthia, Austria). *International Journal of Earth Sciences*, 89 (2000), 40-51.

Weijermars, R., Schmeeling, H., 1986. Scaling of Newtonian and non-Newtonian fluid dynamics without inertia for quantitative modelling of rock flow due to gravity (including the concept of rheological similarity). *Phys. Earth Planet. Inter.* 43, 316–330. [https://doi.org/10.1016/0031-9201\(86\)90021-X](https://doi.org/10.1016/0031-9201(86)90021-X).

Westoby, M.J., Brasington, J., Glasser, N.F., Hambrey, M.J. & Reynolds, J.M., 2012. Structure-from-Motion photogrammetry: A low-cost, effective tool for geoscience applications. *Geomorphology*, 179, 300-314. <https://doi.org/10.1016/j.geomorph.2012.08.021>.

Xiao, Y., Wu, G., Lei, Y., Chen, T., 2017. Analogue modeling of through-going process and development pattern of strike-slip fault zone. *Pet. Explor. Dev.* 44, 368–376. [https://doi.org/10.1016/S1876-3804\(17\)30043-5](https://doi.org/10.1016/S1876-3804(17)30043-5).

**Table 1 Model characteristics and experimental conditions**

Models	Thickness of brittle layer	Thickness of ductile layer	Intrusion rate, $I_r$	Injected Volume, $I_v$	Relative displacement rate, $D_v$	Total horizontal displacement, $D_t$	Experiment Duration
<b>Reference models (Group R)</b>							
Simple shear RS	40mm	7mm	-	-	1.0 mm/min	30 mm	30 min
Transtension RT	40mm	7mm	-	-	1.0 mm/min	30 mm	30 min
Static Intrusion R0	40mm	7mm	21.0 mm <sup>3</sup> /s	37.7x10 <sup>3</sup> mm <sup>3</sup>	-	-	30 min
<b>Simple shear models (Group A)</b>							
Pre-tectonic intrusion A1	40mm	7mm	21.0 mm <sup>3</sup> /s	37.7x10 <sup>3</sup> mm <sup>3</sup>	1.0 mm/min	30 mm	60 min
Syn-Tectonic Intrusion A2	40mm	7mm	21.0 mm <sup>3</sup> /s	37.7x10 <sup>3</sup> mm <sup>3</sup>	1.0 mm/min	30 mm	30 min
Post-tectonic intrusion A3	40mm	7mm	21.0 mm <sup>3</sup> /s	37.7x10 <sup>3</sup> mm <sup>3</sup>	1.0 mm/min	30 mm	60 min
<b>Transtension models (Group B)</b>							
Pre-tectonic intrusion B1	40mm	7mm	21.0 mm <sup>3</sup> /s	37.7x10 <sup>3</sup> mm <sup>3</sup>	1.0 mm/min	30 mm	60 min
Syn-Tectonic Intrusion B2	40mm	7mm	21.0 mm <sup>3</sup> /s	37.7x10 <sup>3</sup> mm <sup>3</sup>	1.0 mm/min	30 mm	30 min
Post-tectonic intrusion B3	40mm	7mm	21.0 mm <sup>3</sup> /s	37.7x10 <sup>3</sup> mm <sup>3</sup>	1.0 mm/min	30 mm	60 min

Table 2 material properties and scaling factors

Parameters	Models	Nature	Model/ Nature (Scaling factor)
Brittle material	Quartz Sand	Upper Crust	
Length, L	0.01 m	0.6 - 6 km	$0.6 - 6 \times 10^{-6}$
Cohesion, C	10-100 Pa	10 MPa	$1-10 \times 10^{-6}$
Density, $\rho$	1600 Kg/m	2600 kg/m	0.615
Gravity, g	9.81 m/s	9.81 m/s	1
Viscous material	Silicone oil	Intrusion/ shear zone	
Viscosity, $\eta$	$3 \times 10^{-4}$ Pa s	$>10^{18}$ Pa s	$3.0 \times 10^{-14}$
Density, $\rho$	965 kg/m	1600 kg/m	0.603
Time, t	1 sec	30000 yrs	$10^{-13}$

**Table 3** Summarizing table of diagnostic attributes as suggested by the analogue models for the different emplacement scenarios and kinematic settings.

Model	Pluton Elongation $r = L/W^a$		Orientation $\Theta^a$		Dike system		Pluton amplitude A	
	Simple shear (A)	Transtension (B)	Simple shear (A)	Transtension (B)	Simple shear (A)	Transtension (B)	Simple shear (A)	Transtension (B)
<b>Kinematic setting</b>								
<b>Pre-tectonic</b>	<b>Very high</b> ( $r_{A1} > 3$ )	<b>Medium</b> ( $r_{B1} > 1.5$ )	Long axis // <b>extension</b>	Long axis // <b>extension</b>	Roof & lateral	Lateral	<b>Low</b>	<b>Very low</b>
<b>Syn-Tectonic</b>	<b>High</b> ( $r_{A2} > 2$ )	<b>Medium<sup>b</sup></b> ( $r_{B2} > 1.5$ )	Long axis // <b>Riedel</b>	Long axis // <b>compression</b>	Lateral & apophysis	Roof & lateral & apophysis	<b>High</b>	<b>High</b>
<b>Post-tectonic</b>	<b>Low</b> ( $r_{A3} < 2$ )	<b>Low</b> ( $r_{B3} < 2$ )	Long axis // <b>Riedel</b>	Long axis // <b>Riedel</b>	Roof & lateral	Roof & lateral	<b>Medium</b>	<b>Medium</b>

<sup>a</sup> Based on an ellipse fitted to the lower ( $C_1$ ) and higher ( $C_2$ ) contour level of the intrusion.

<sup>b</sup> Based on repetition models (100, 59, 95; see Appendix A.1)

## 8 Figures and Captions

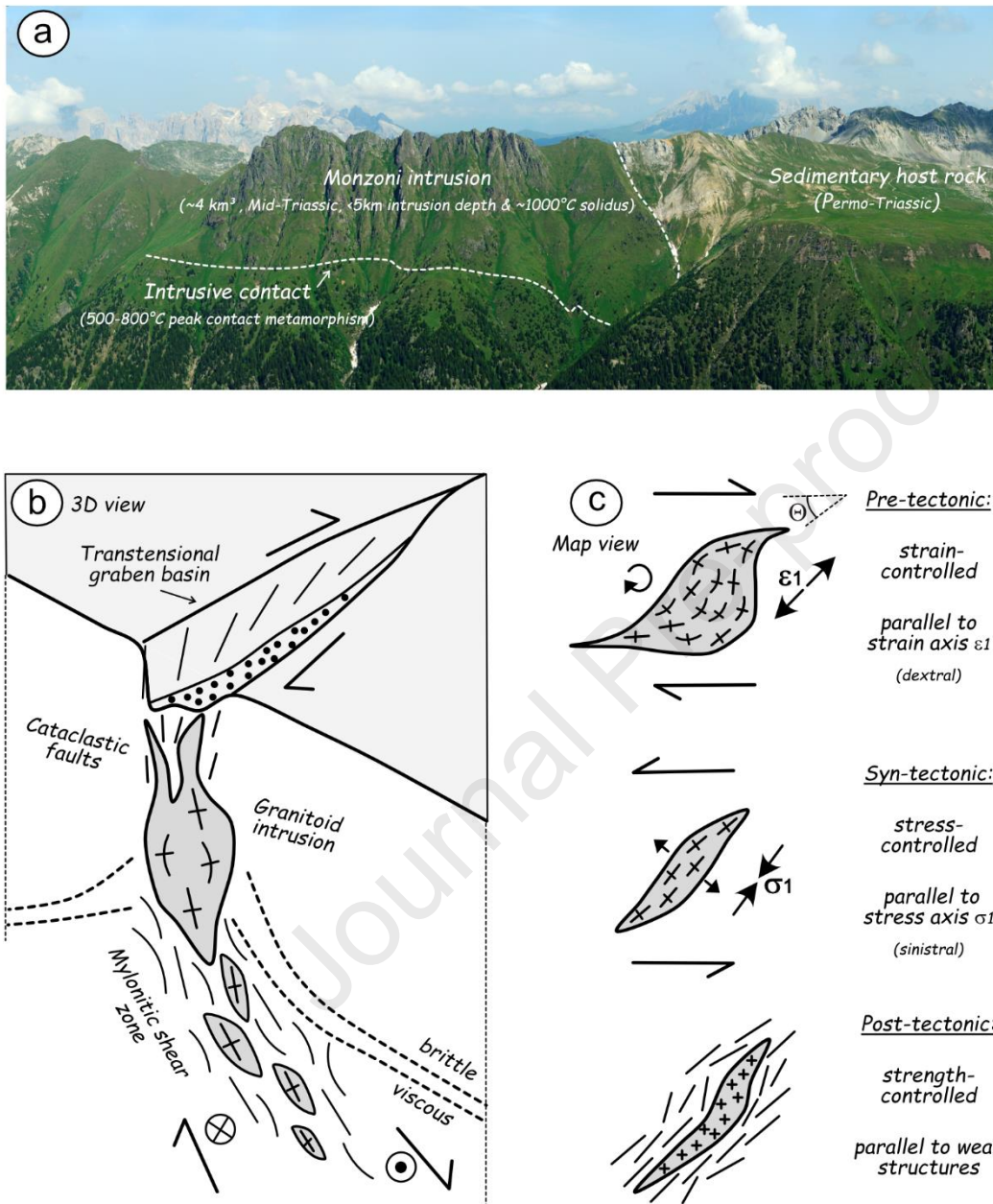


**Figure 1:** Introducing the scientific problem: (a) Field view of the Monzoni granitoid intrusion in the Dolomites (Photo credit: Matteo Visintainer), (b) 3 D sketch of granitoids intruding along crustal scale shear zones, (c) key scenarios of tectono-magmatic relations. Note the ambiguity of the overall elongate shape and orientation with respect to shear zone (angle  $\theta$ ) with respect to temporal relation and kinematics.

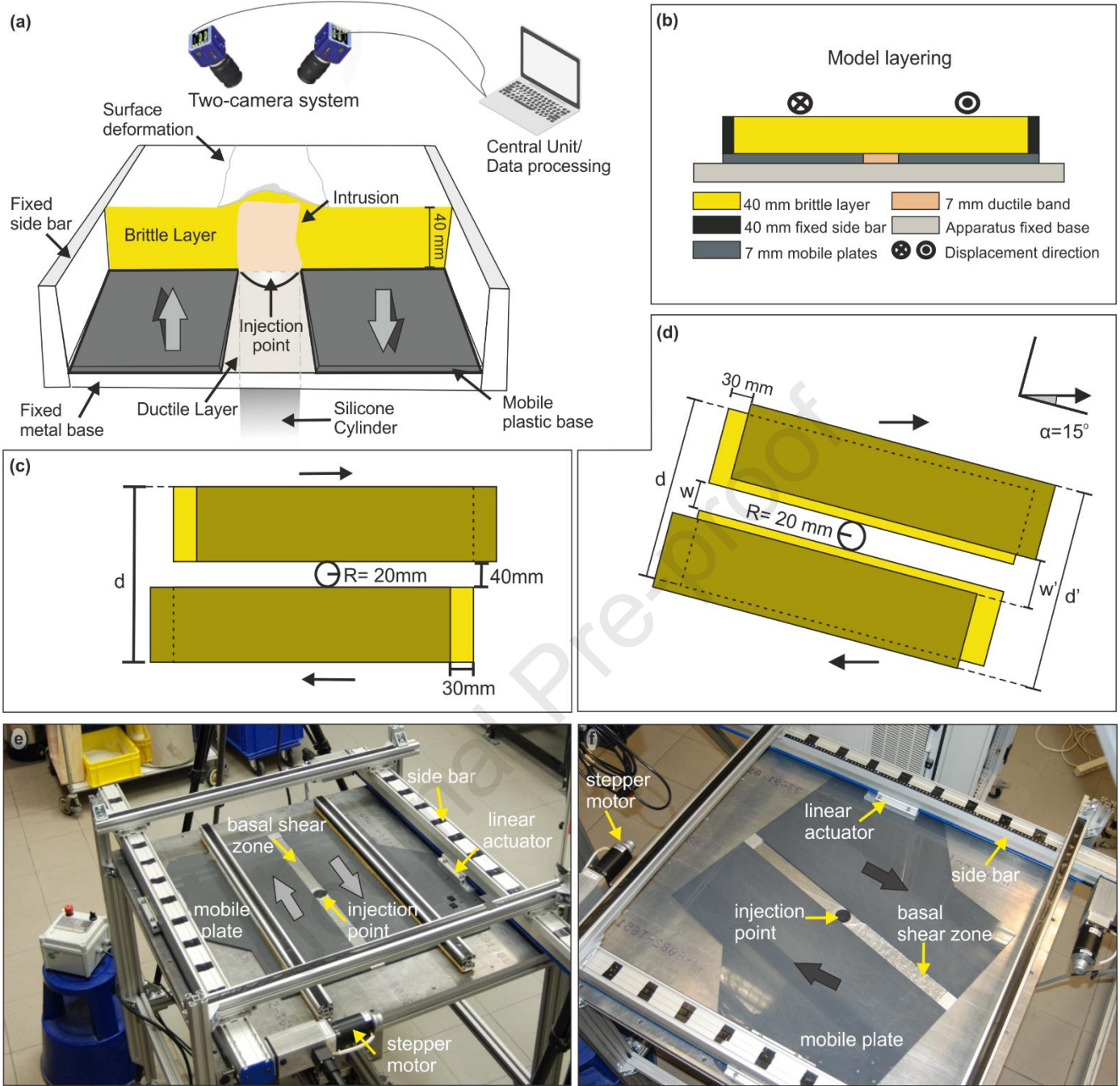


**Figure 2:** Details of the experimental apparatus. Details of the experimental set-up. (a) Schematic cut-out 3D view depicting its various components; (b) Model layering; kinematic basal boundary conditions for (c) Sketch of the experimental setting of the simple shear deformation ( $d = 310$  mm) and (d) the transtensional deformation (obliquity  $\alpha = 15^\circ$ ) with the initial (yellow) and final (green) positions of the mobile plates ( $w = 40$  mm,  $w' = 55.5$  mm,  $d = 360$  mm,  $d' = 375.5$  mm); Oblique view of experimental settings for (e) simple shear and (f) transtensional deformation. Arrows indicate the direction of plates relative motion.

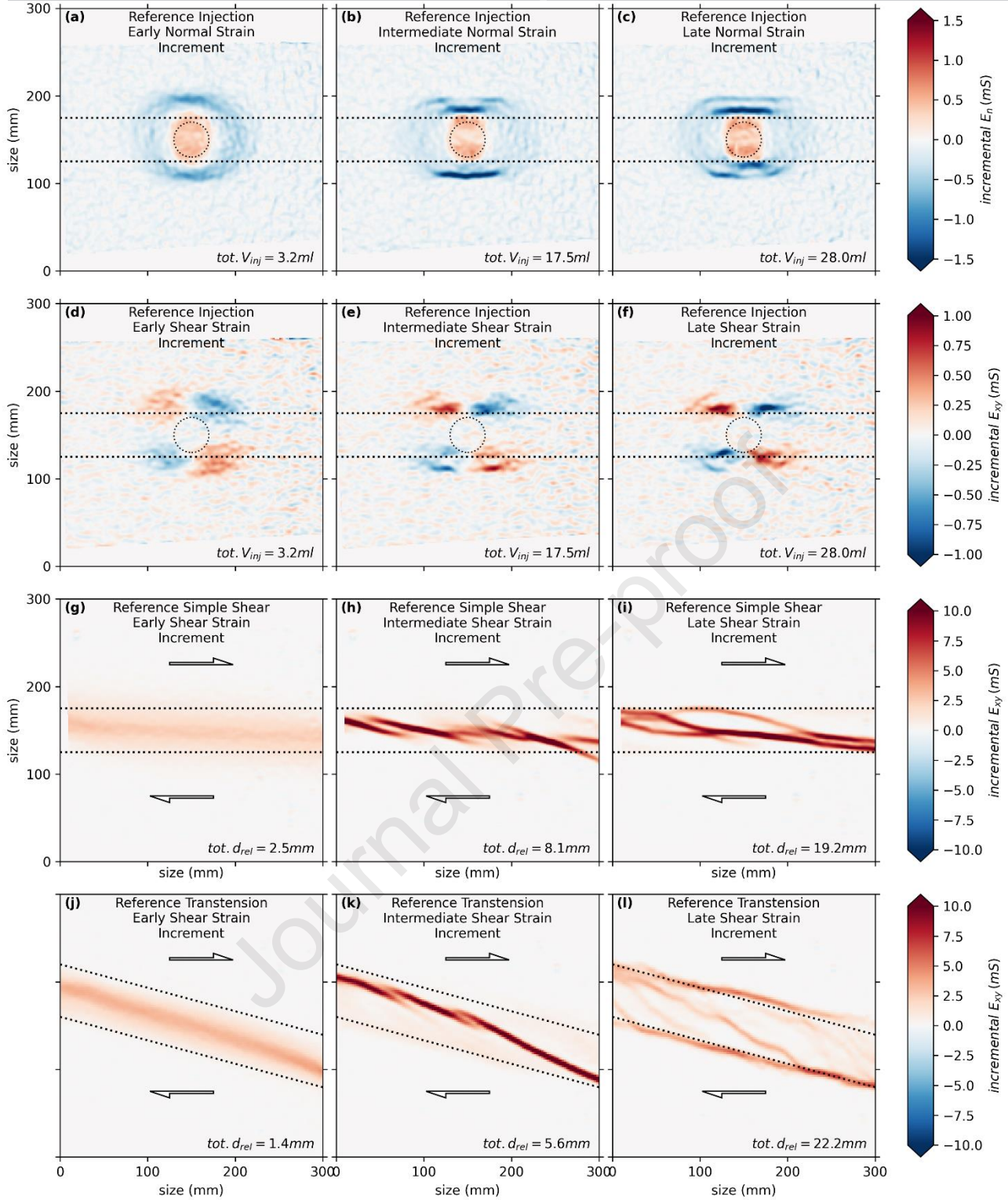


**Figure 3:** Surface deformation of the reference experiments (Group R): representative increments of the surface normal strain evolution ( $E_n$ , a-c) and shear strain ( $E_{xy}$ , d-f) of the static intrusion reference model R0 and surface shear strain evolution of the simple shear reference model RS (g-i) and the transtension reference model RT(j-l). Total volumes injected and total relative displacements achieved as indicated. Positive strain values (red color) of normal and shear strain  $E_n$  and  $E_{xy}$  indicate extension and dextral shear sense, respectively. Dotted circles indicate the position of the basal injection. Dotted lines indicate basal shear zone limits.

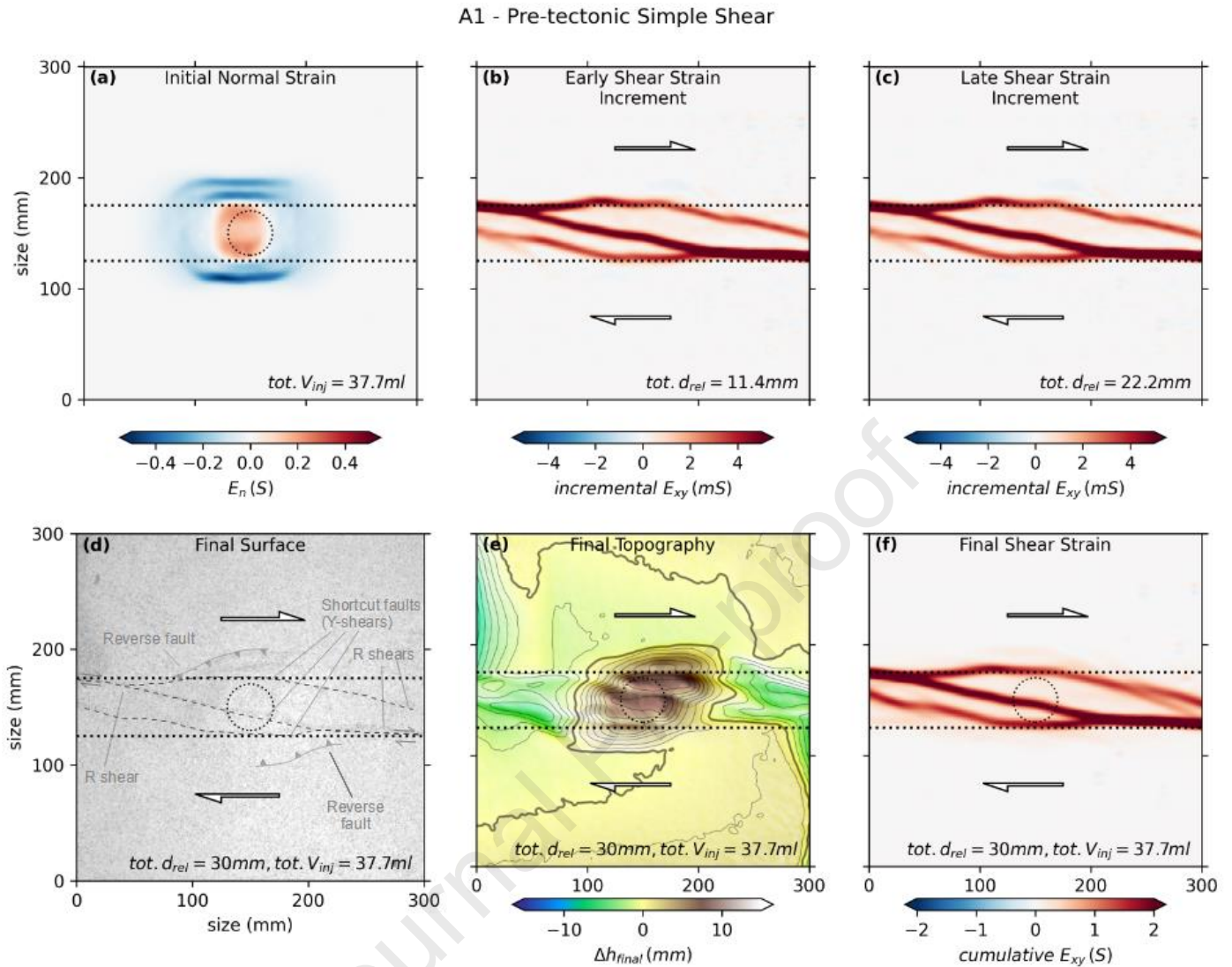


**Figure 4:** Surface deformation of the pre-tectonic intrusion model in simple shear (Model A1). Shown are snapshots of the evolution (a-c) and the final surface deformation (d-e): (a) Initial surface normal strain field showing the inherited fault pattern related to previous intrusion, (b) incremental shear strain during an early stage, and (c) late stage of shearing, (d) surface image at the end of the experiment, (e) cumulative vertical displacement, (f) cumulative shear strain. Total volumes injected and total relative displacements achieved as indicated. Positive strain values (red color) of normal and shear strain  $E_n$  and  $E_{xy}$  indicate extension and dextral shear sense, respectively. Dotted circles indicate the position of the basal injection. Dotted lines indicate basal shear zone limits.

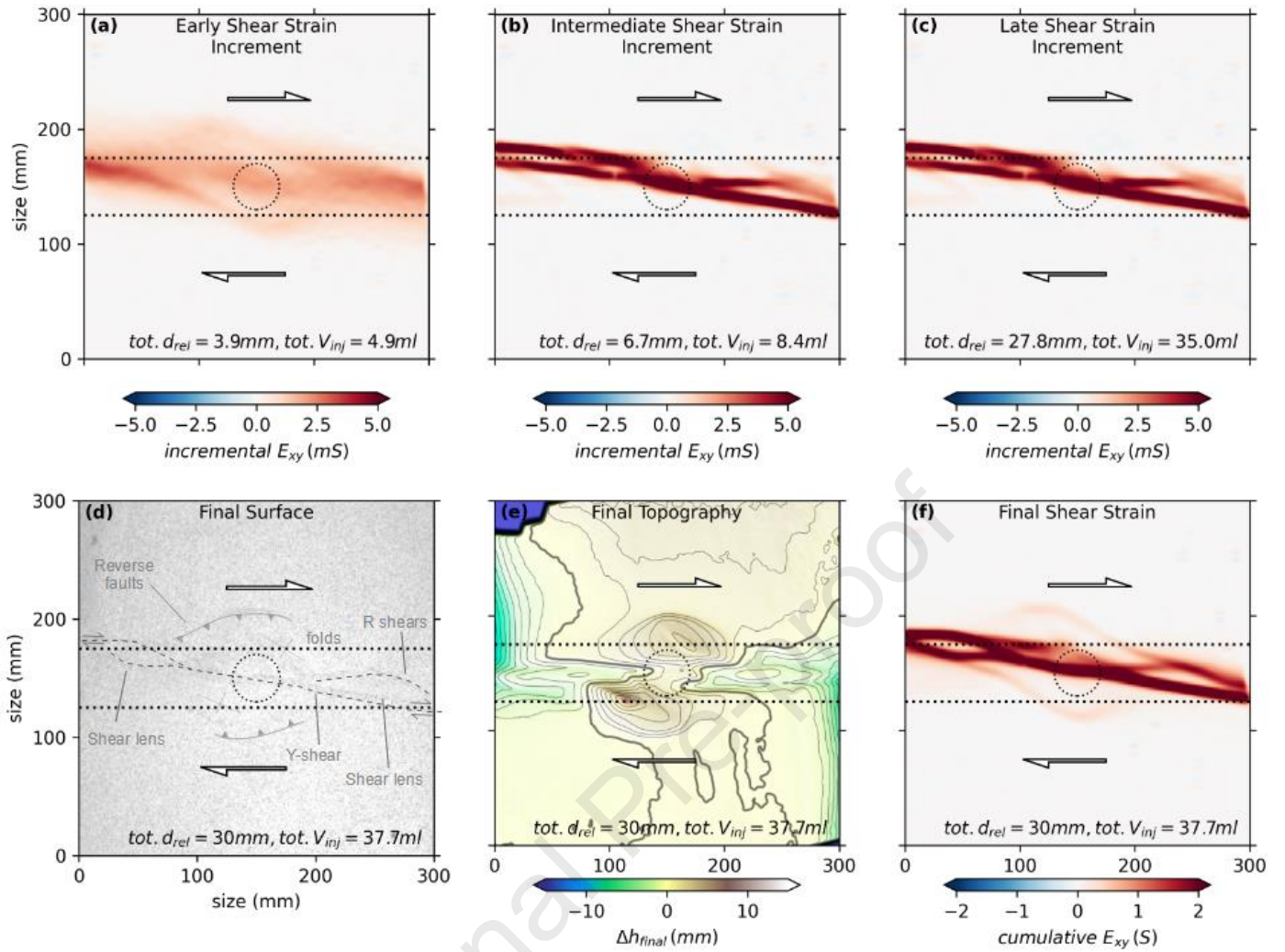


**Figure 5:** Surface deformation of the syn-tectonic intrusion model in simple shear (Model A2). Shown are snapshots of the evolution (a-c) and the final surface deformation (d-e): (a) incremental shear strain during an early stage, (b) an intermediate stage, and (c) a late stage of shearing and intrusion, (d) surface image at the end of the experiment, (e) cumulative vertical displacement, (f) cumulative shear strain. Total volumes injected and total relative displacements achieved as indicated. Positive strain values (red color) of normal and shear strain  $E_n$  and  $E_{xy}$  indicate extension and dextral shear sense, respectively. Dotted circles indicate the position of the basal injection. Dotted lines indicate basal shear zone limits.

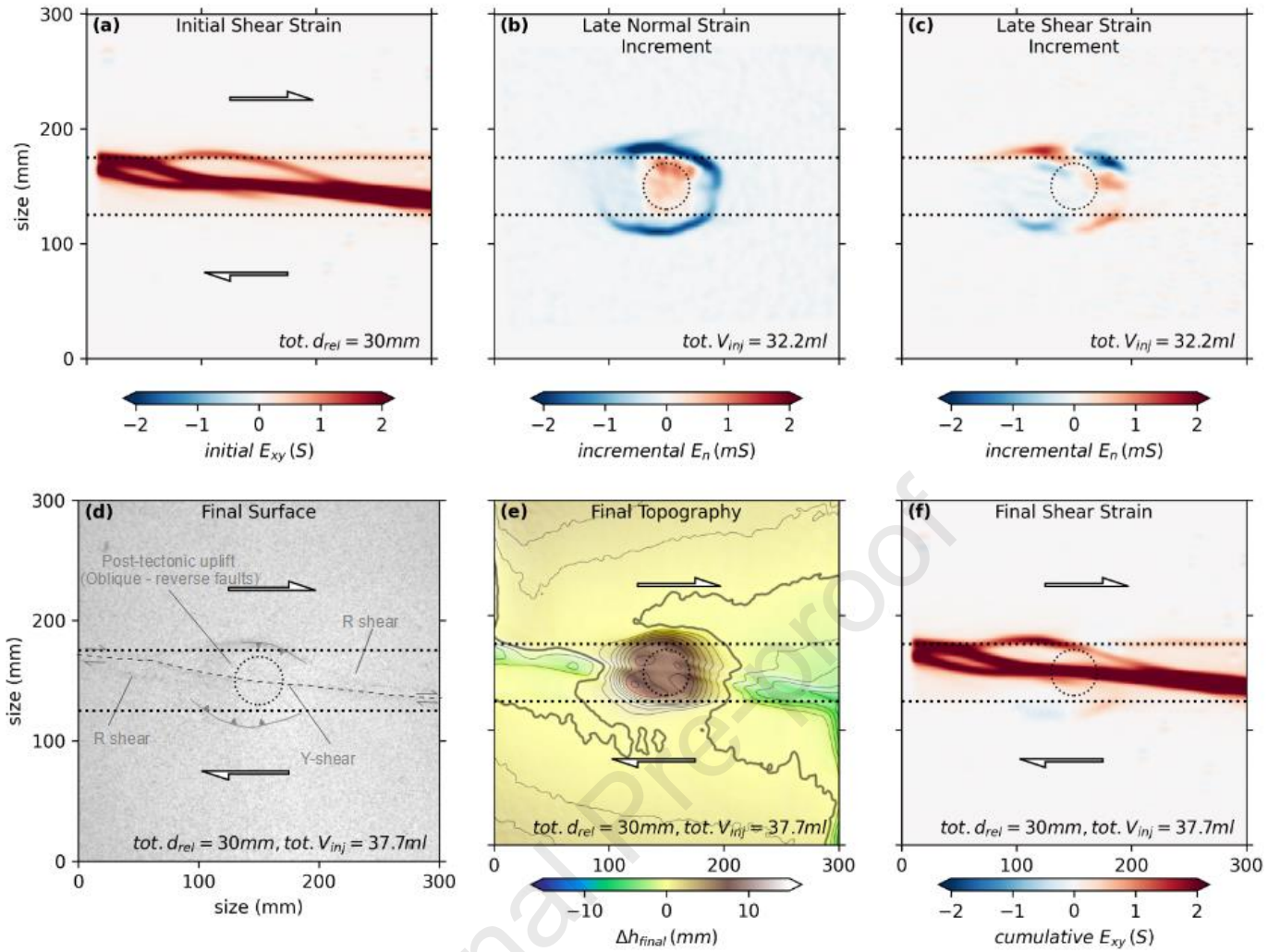


**Figure 6:** Surface deformation of the post-tectonic intrusion model in simple shear (Model A3). Shown are snapshots of the evolution (a-c) and the final surface deformation (d-e): (a) Initial surface shear strain field showing the inherited fault pattern related to previous shearing, incremental normal (b) and shear (c) strain during and late stage, (d) surface image at the end of the experiment, (e) cumulative vertical displacement, (f) cumulative shear strain. Total volumes injected and total relative displacements achieved as indicated. Positive strain values (red color) of normal and shear strain  $E_n$  and  $E_{xy}$  indicate extension and dextral shear sense, respectively. Dotted circles indicate the position of the basal injection. Dotted lines indicate basal shear zone limits.

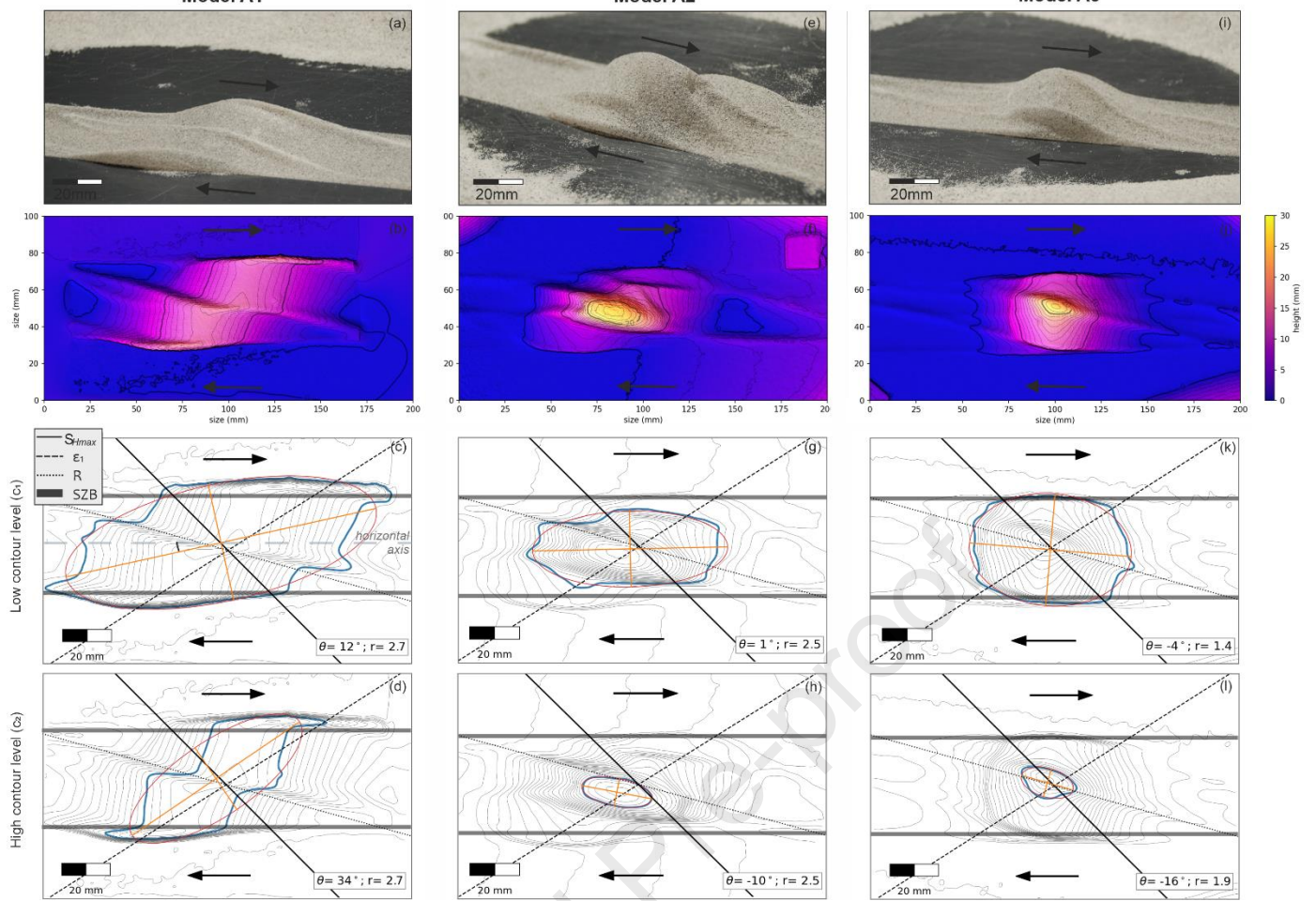


**Figure 7:** Models of the intrusions in the simple shear regime (Group A): Model A1 (a-c); Model A2 (d-f) and Model A3 (g-i). (a, d, g) Oblique views of the excavated intrusions; (b, e, h) Digital Intrusion Models (DIM) coloured and with contour lines; (c, f, i) Orientation and geometry of the intrusion (in map view), where  $\theta$  = the angle between the long axis (orange) of the fitted ellipse (red) and the strike of the basal shear zone.  $r$  is the intrusion's aspect ratio (length-to-width ratio,  $r$ ).

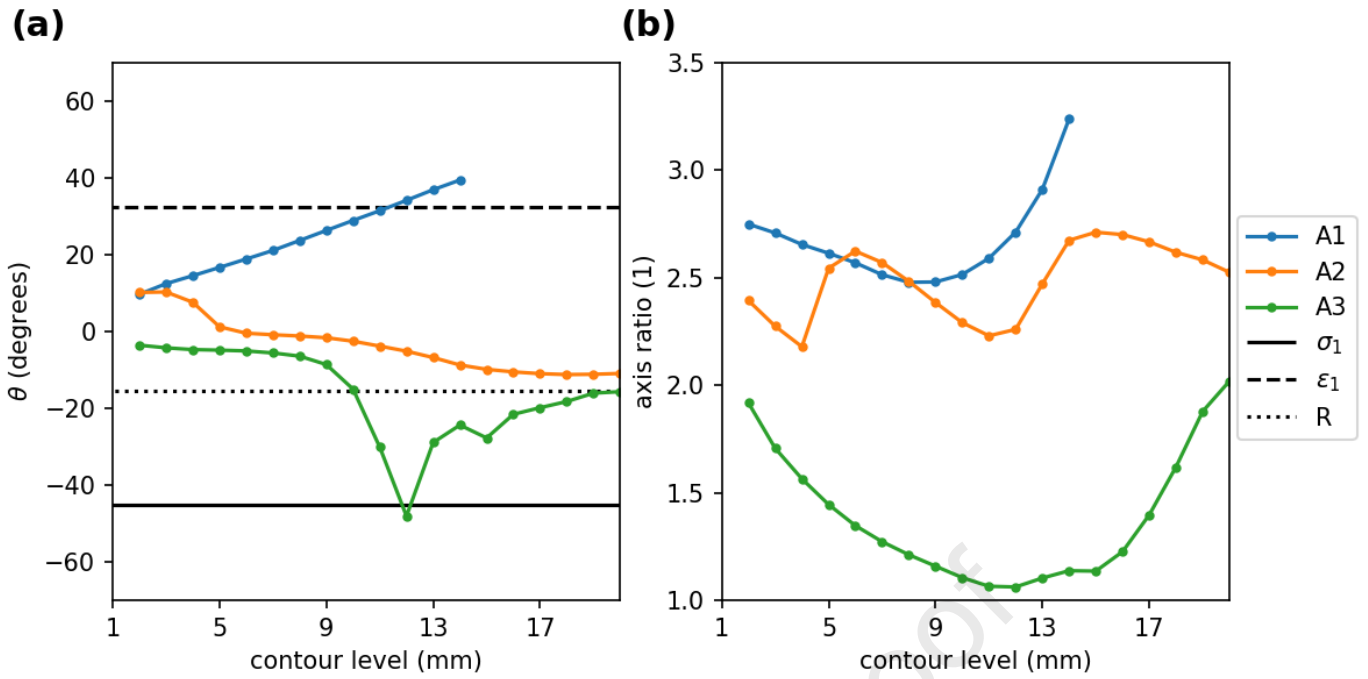


**Figure 8:** Vertical variation of pluton shape in the simple shear regime (Group A): Left: long axis angle versus height (contour level). Right: elongation (axis ratio) versus height (contour level).

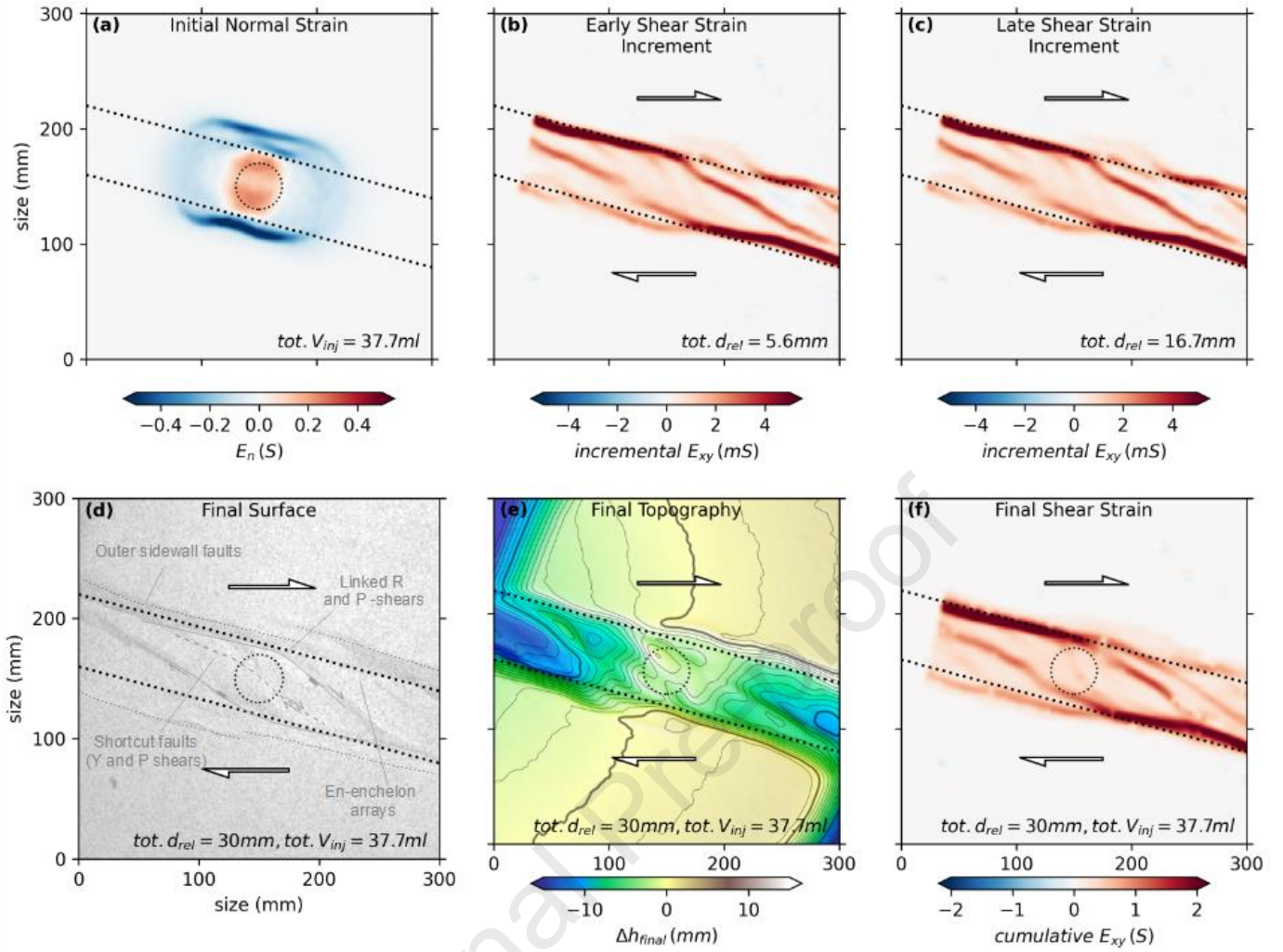


**Figure 9:** Surface deformation of the pre-tectonic intrusion model in transtension (Model B1). Shown are snapshots of the evolution (a-c) and the final surface deformation (d-e): (a) Initial surface normal strain field showing the inherited fault pattern related to previous intrusion, (b) incremental shear strain during an early stage, and (c) late stage of shear-ing, (d) surface image at the end of the experiment, (e) cumulative vertical displacement, (f) cumulative shear strain. Total volumes injected and total relative displacements achieved as indicated. Positive strain values (red color) of normal and shear strain  $E_n$  and  $E_{xy}$  indicate extension and dextral shear sense, respectively. Dotted circles indicate the position of the basal injection. Dotted lines indicate basal shear zone limits.

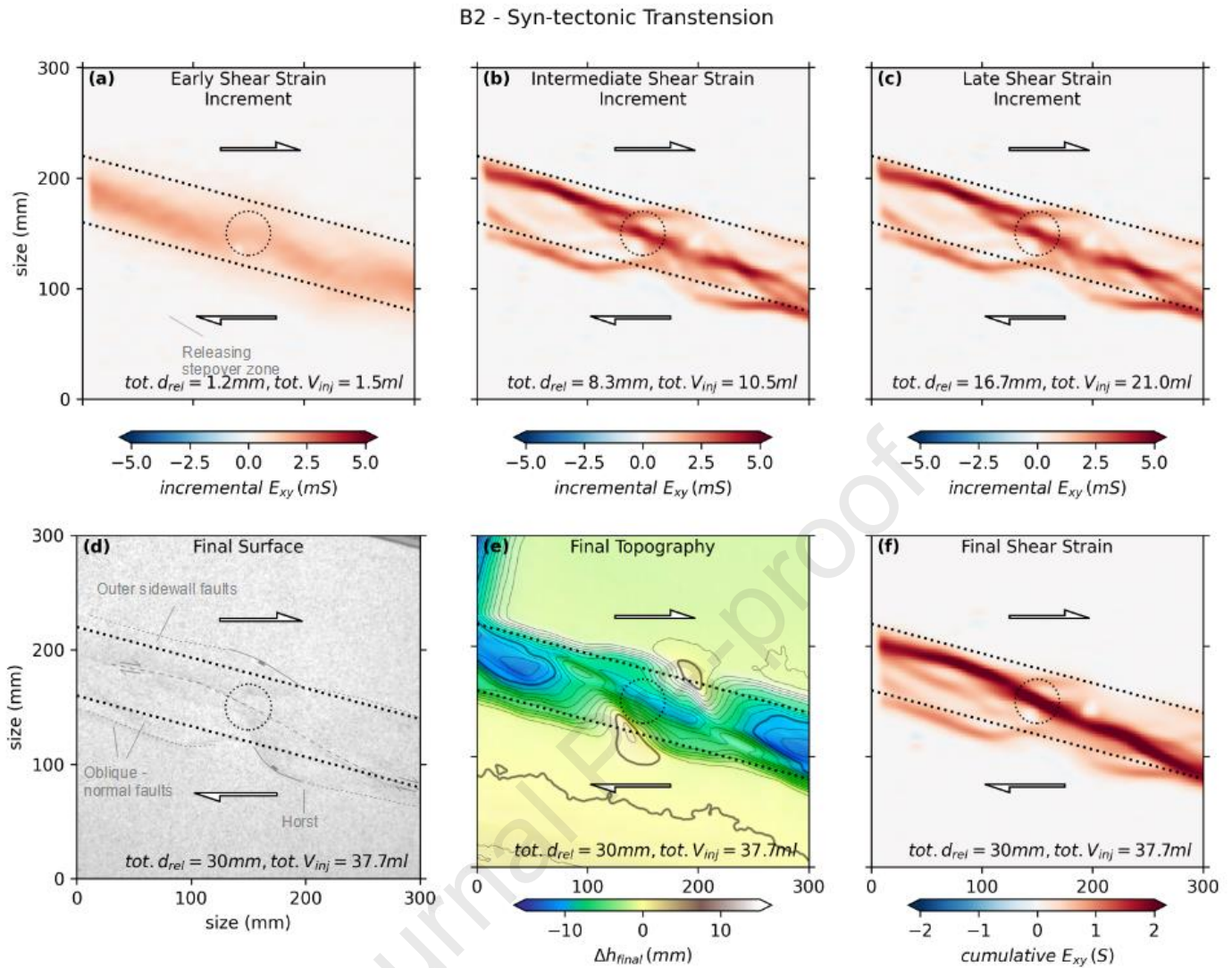


**Figure 10:** Surface deformation of the syn-tectonic intrusion model in transtension (Model B2). Shown are snapshots of the evolution (a-c) and the final surface deformation (d-e): (a) incremental shear strain during an early stage, (b) an intermediate stage, and (c) a late stage of shearing and intrusion, (d) surface image at the end of the experiment, (e) cumulative vertical displacement, (f) cumulative shear strain. Total volumes injected and total relative displacements achieved as indicated. Positive strain values (red color) of normal and shear strain  $E_n$  and  $E_{xy}$  indicate extension and dextral shear sense, respectively. Dotted circles indicate the position of the basal injection. Dotted lines indicate basal shear zone limits.

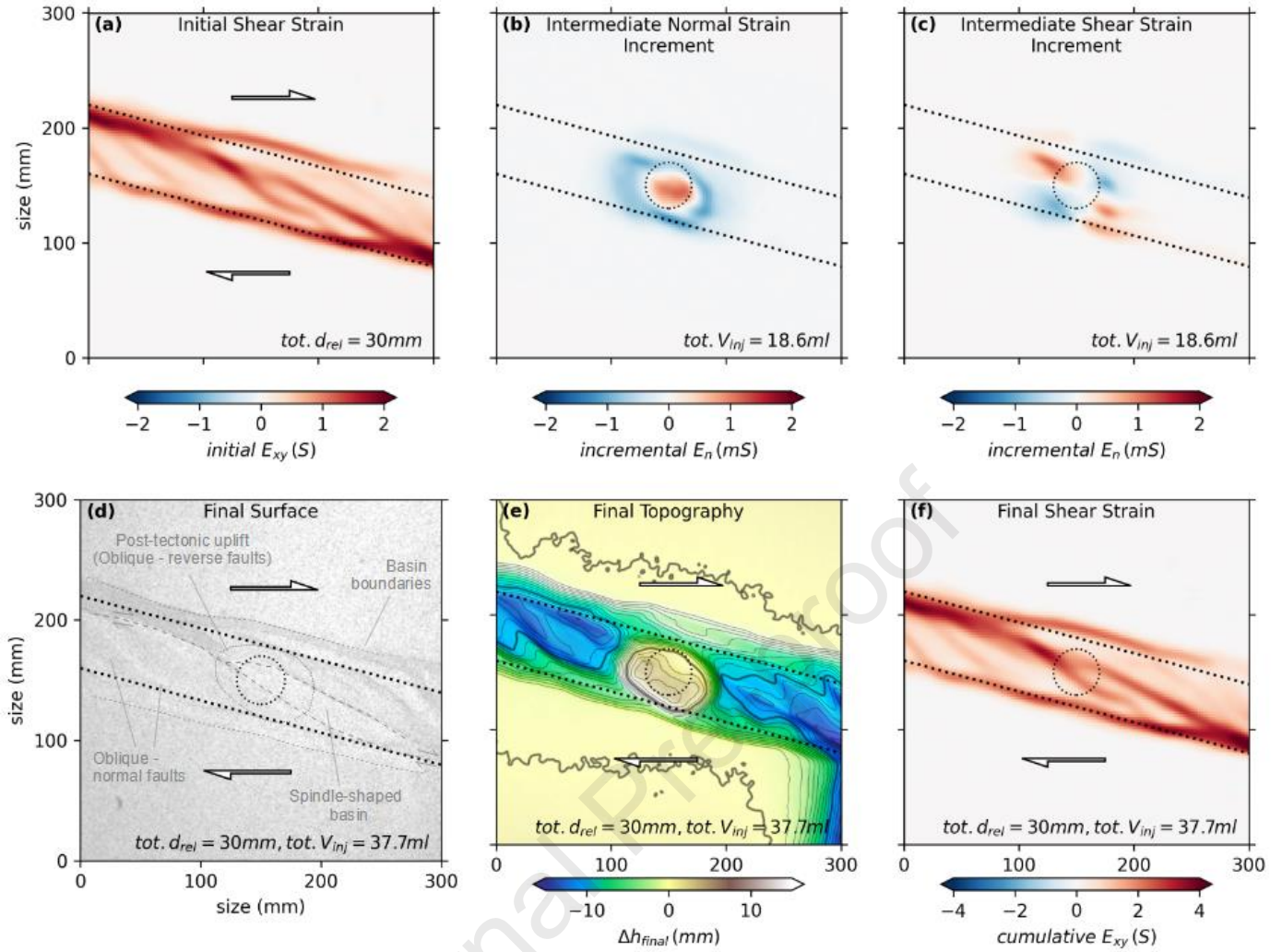


**Figure 11:** Surface deformation of the post-tectonic intrusion model in transtension (Model B3). Shown are snapshots of the evolution (a-c) and the final surface deformation (d-e): (a) Initial surface shear strain field showing the inherited fault pattern related to previous shearing, incremental normal (b) and shear (c) strain during an intermediate stage, (d) surface image at the end of the experiment, (e) cumulative vertical displacement, (f) cumulative shear strain. Total volumes injected and total relative displacements achieved as indicated. Positive strain values (red color) of normal and shear strain  $E_n$  and  $E_{xy}$  indicate extension and dextral shear sense, respectively. Dotted circles indicate the position of the basal injection. Dotted lines indicate basal shear zone limits.

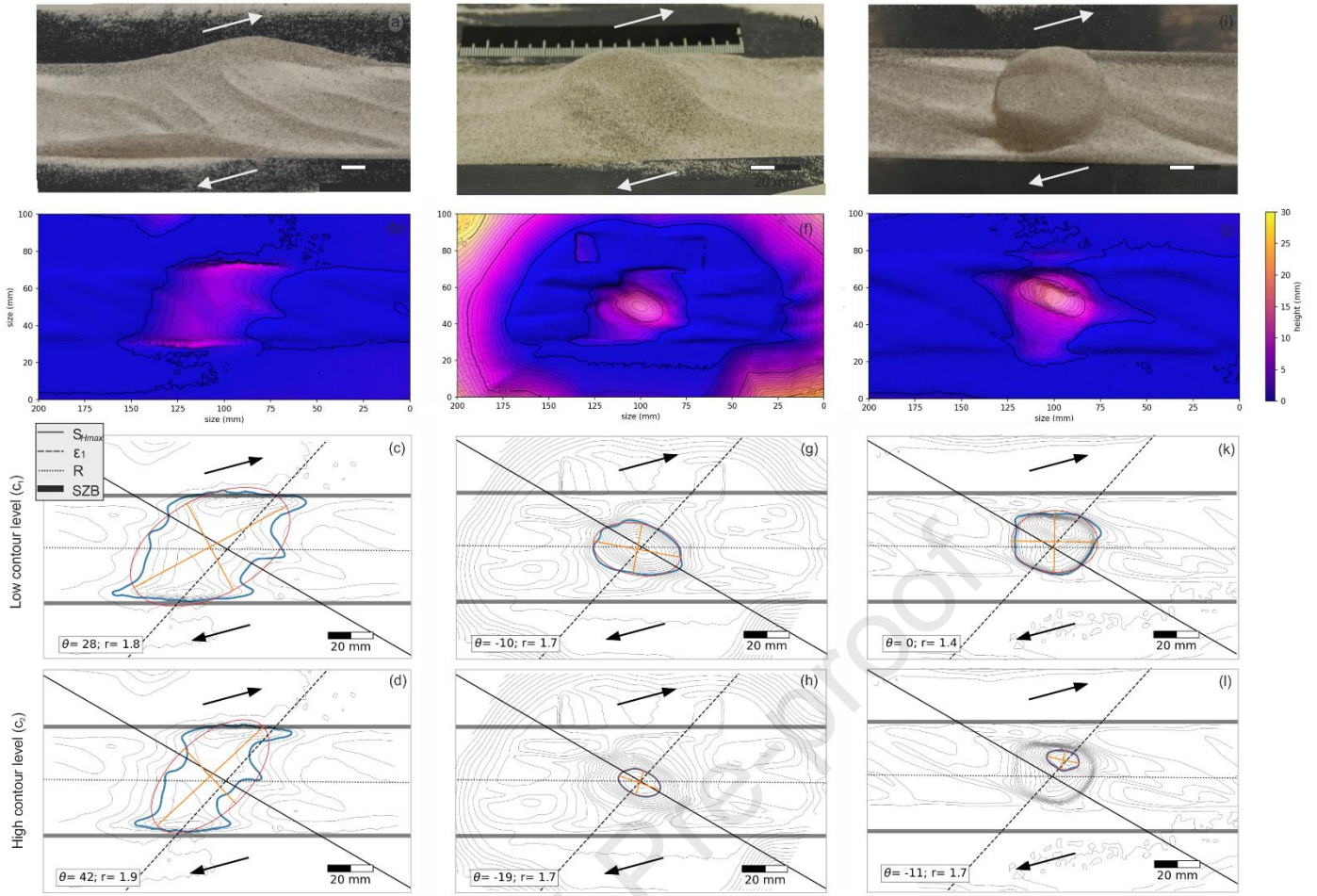


**Figure 12:** Models of the intrusions in the transtensional regime (Group B): Model B1 (a-c); Model B2 (d-f) and Model B3 (g-i). (a, d, g) Oblique views of the excavated intrusions; (b, e, h) Digital Intrusion Models (DIM) coloured and with contour lines; (c, f, i) Orientation and geometry of the intrusion (in map view), where  $\theta$  = the angle between the long axis (orange) of the fitted ellipse (red) and the strike of the basal shear zone.  $r$  is the intrusion's aspect ratio (length-to-width ratio,  $r$ ).

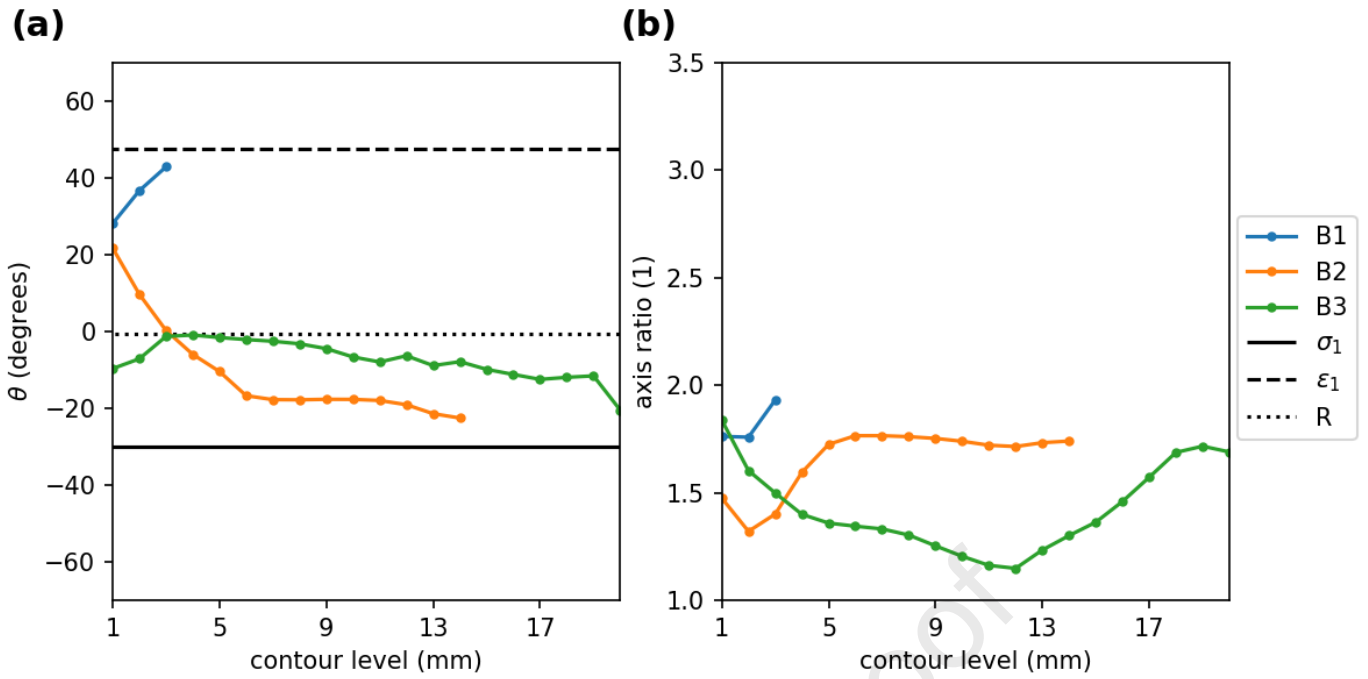
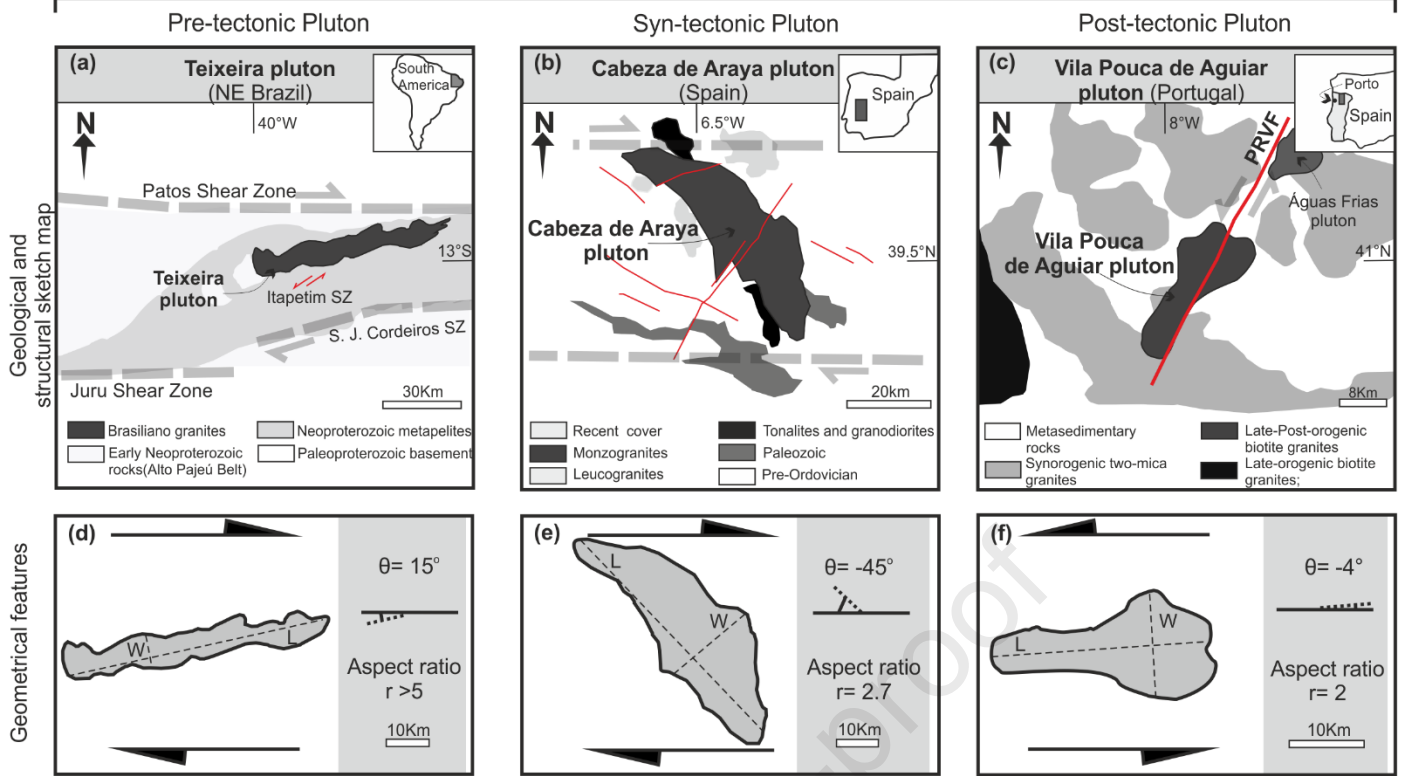


**Figure 13:** Vertical variation of pluton shape in the transtensional regime (Group B): Left: long axis angle versus height (contour level). Right: elongation (axis ratio) versus height (contour level).



### Natural Examples in Transtension

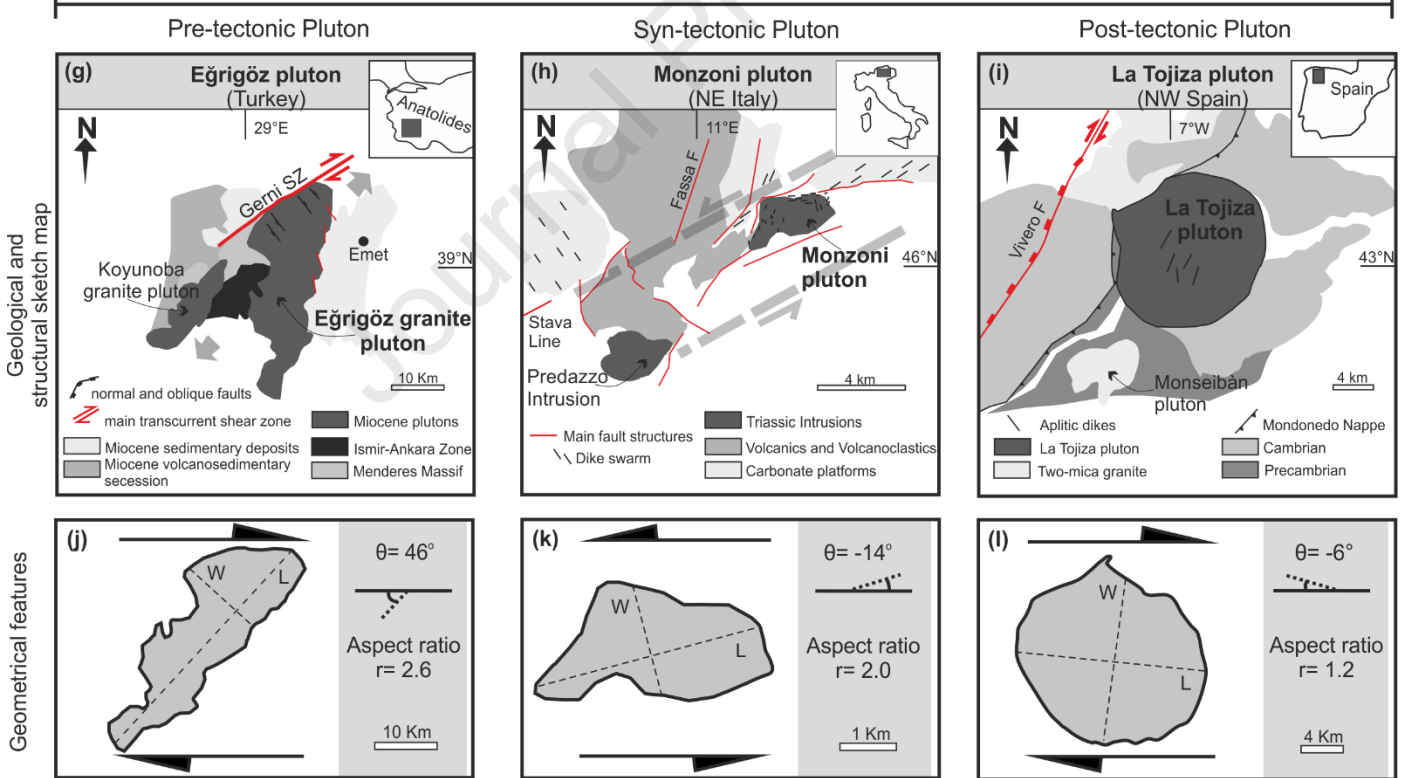


**Figure 14:** Simplified geological maps and shapes of natural plutons emplaced in simple shear and transtensional zones: (a, d) The Teixeira pluton (Archanjo et al., 2008); (b, e) The Cabeza de Araya Pluton (Vigneresse and Bouchez, 1997; Fernandez and Castro, 1999; Corti et al., 2005) and (c, f) The Vila Pouca de Aguiar pluton (Sant'Ovaia et al., 2000). Plutons emplaced in transtensional regime: (g, j) The Eğrigöz pluton is a pre-tectonic intrusion affected by rotation

due to the transtensional deformation occurring after the emplacement (Erkür et al., 2017); (n, k) The Monzonit Pluton developed within a transtensional tectonic environment (Sloman, 1989; Bonadiman et al., 1994); (i, l) La Tojiza Pluton is a clear example of post-tectonic intrusion only slightly reactivating the previous transtensional tectonic structures (Aranguren et al., 2003).

Journal Pre-proof

## 9 Appendix – Supplementary figures

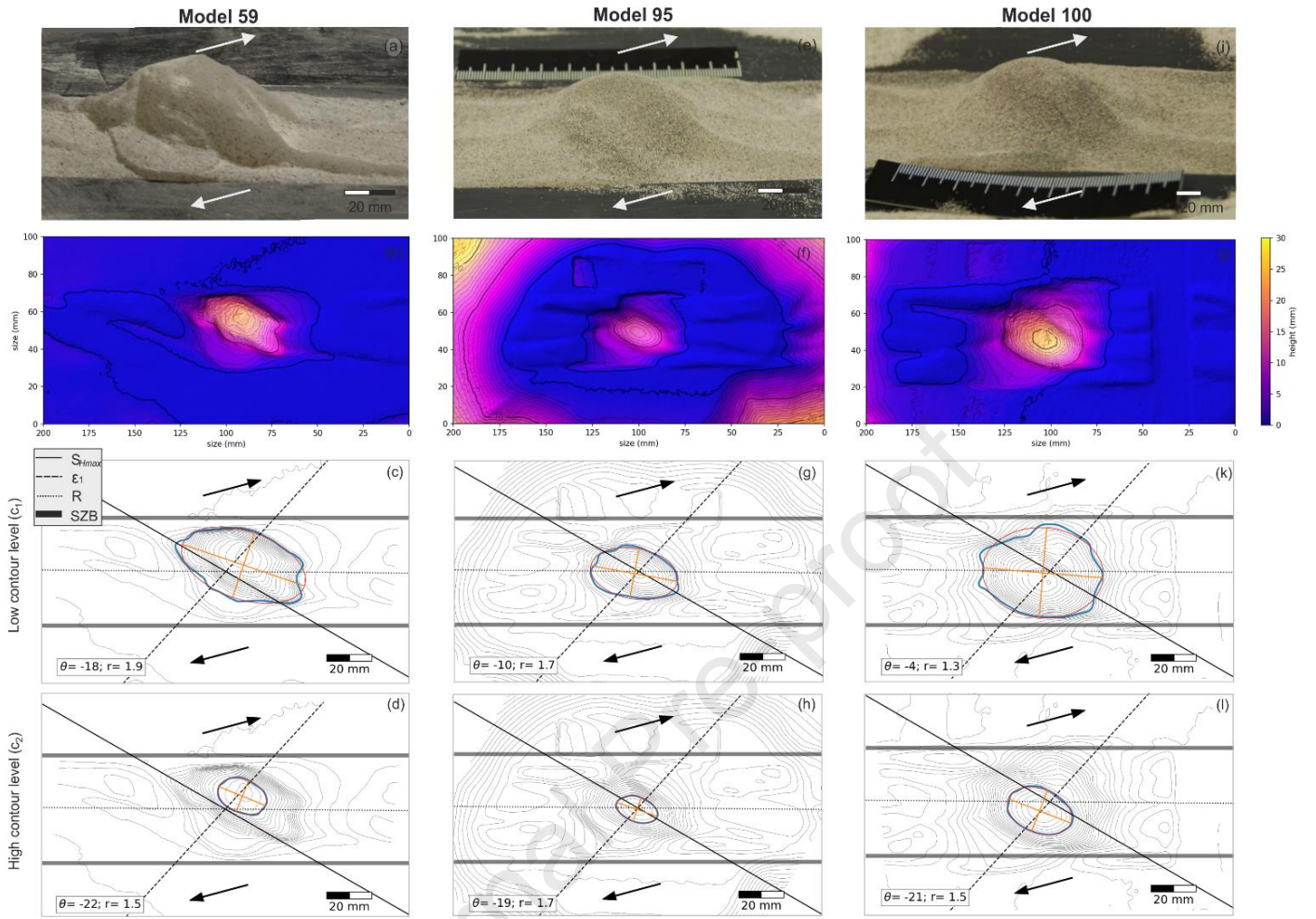


**Figure A.1:** Intrinsic variability of intrusion models verified by repeating experiments (Model B2) in syn-tectonic intrusion in transtension.

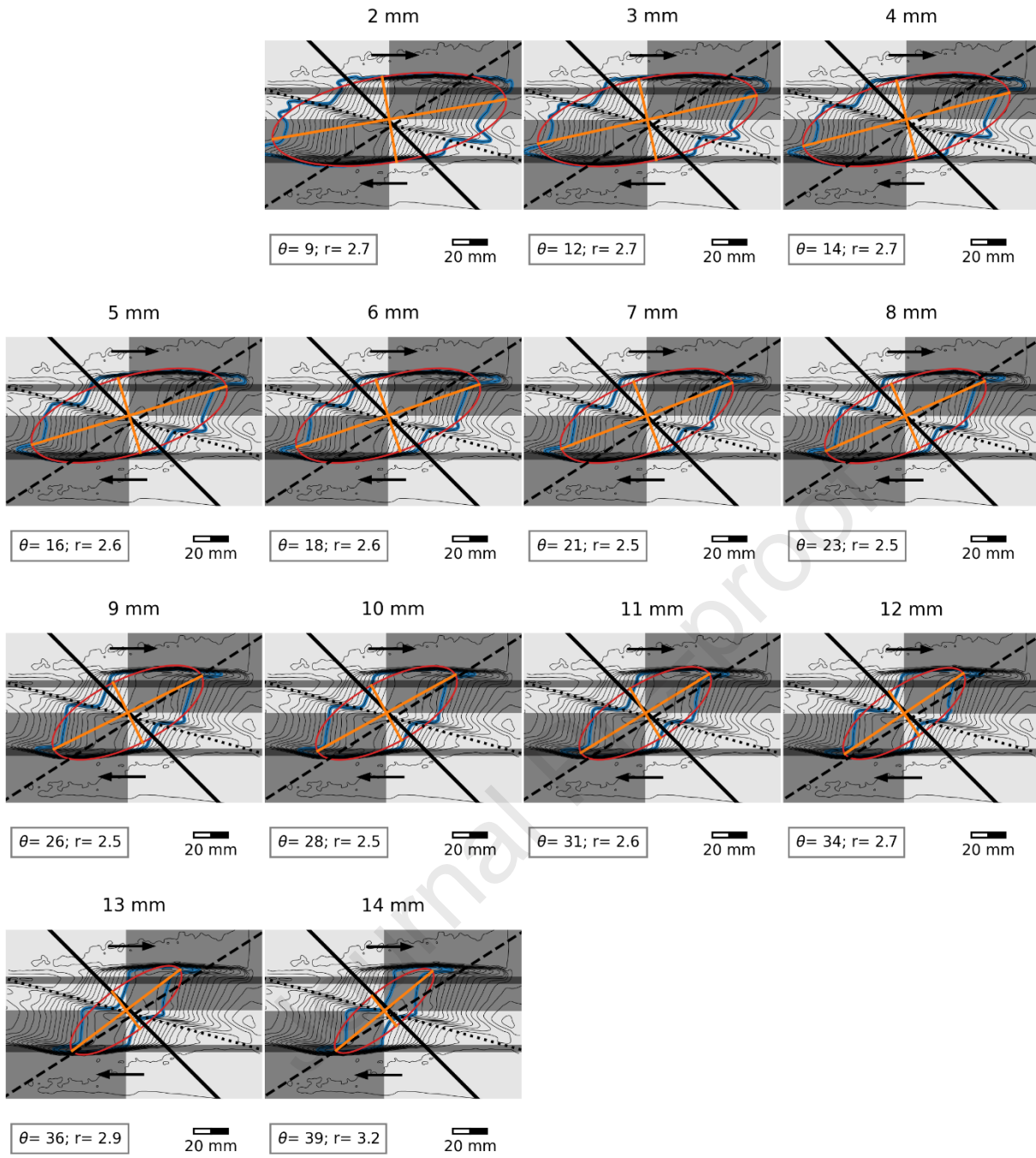


**Figure A.2:** Complete contour ellipses analysis of Model A1 shape as a function of height.

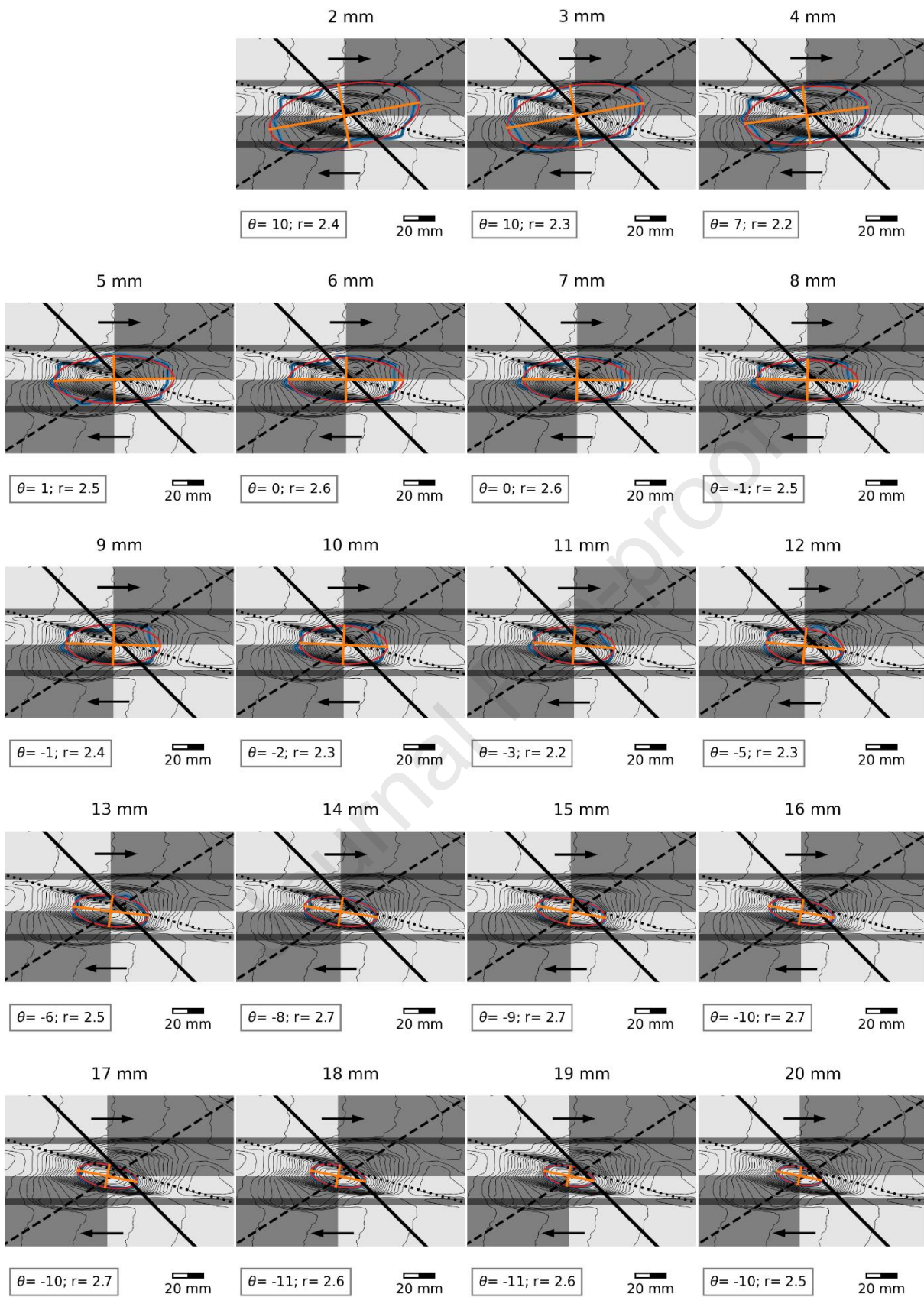


**Figure A.3:** Complete contour ellipses analysis of Model A2 shape as a function of height

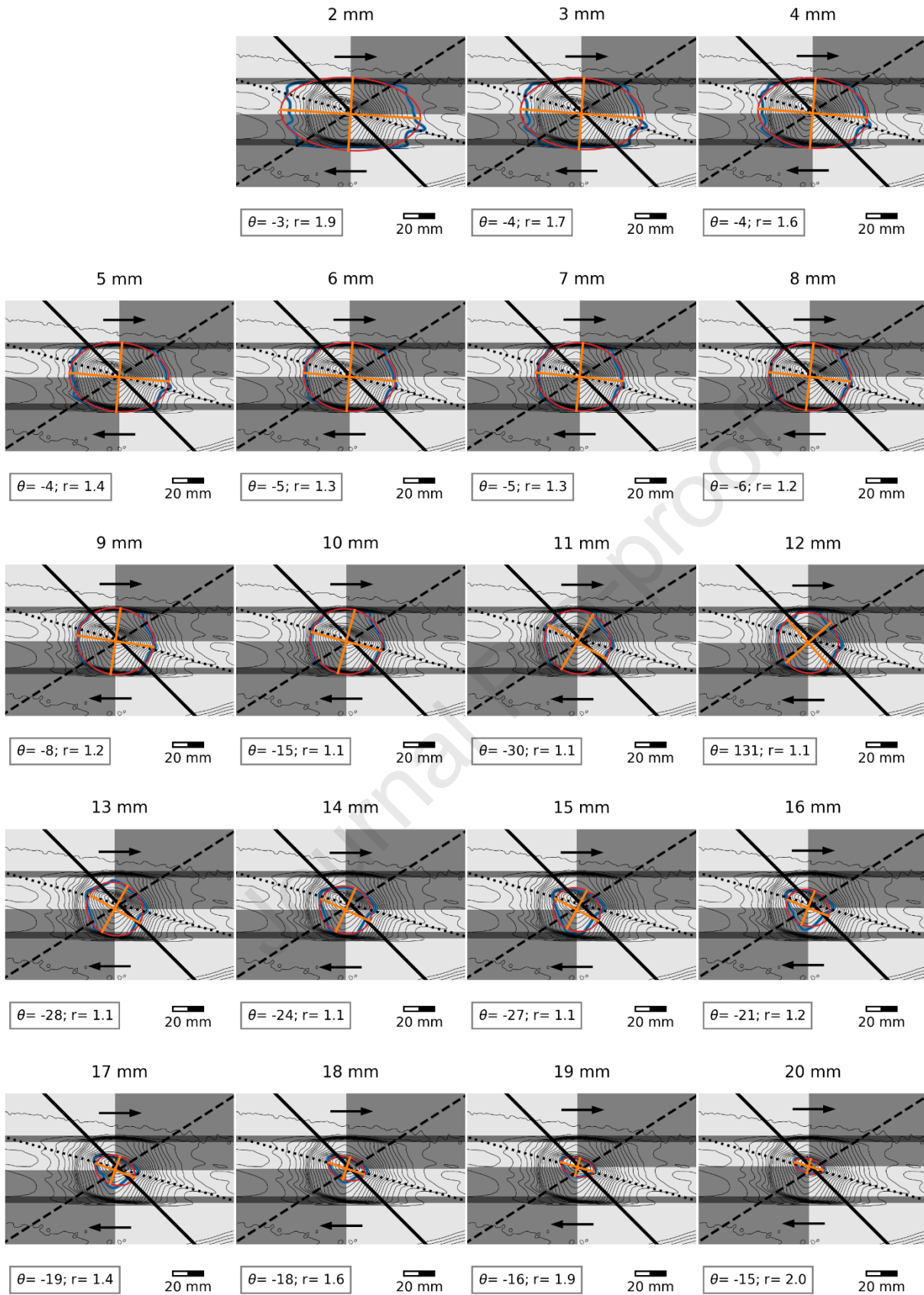


**Figure A.4:** Complete contour ellipses analysis of Model A3 shape as a function of height

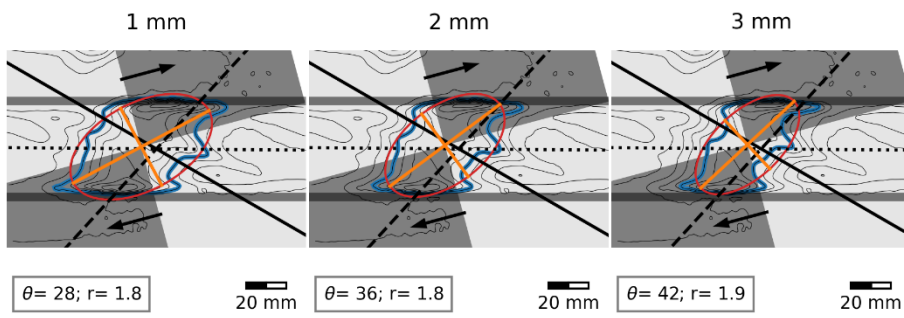
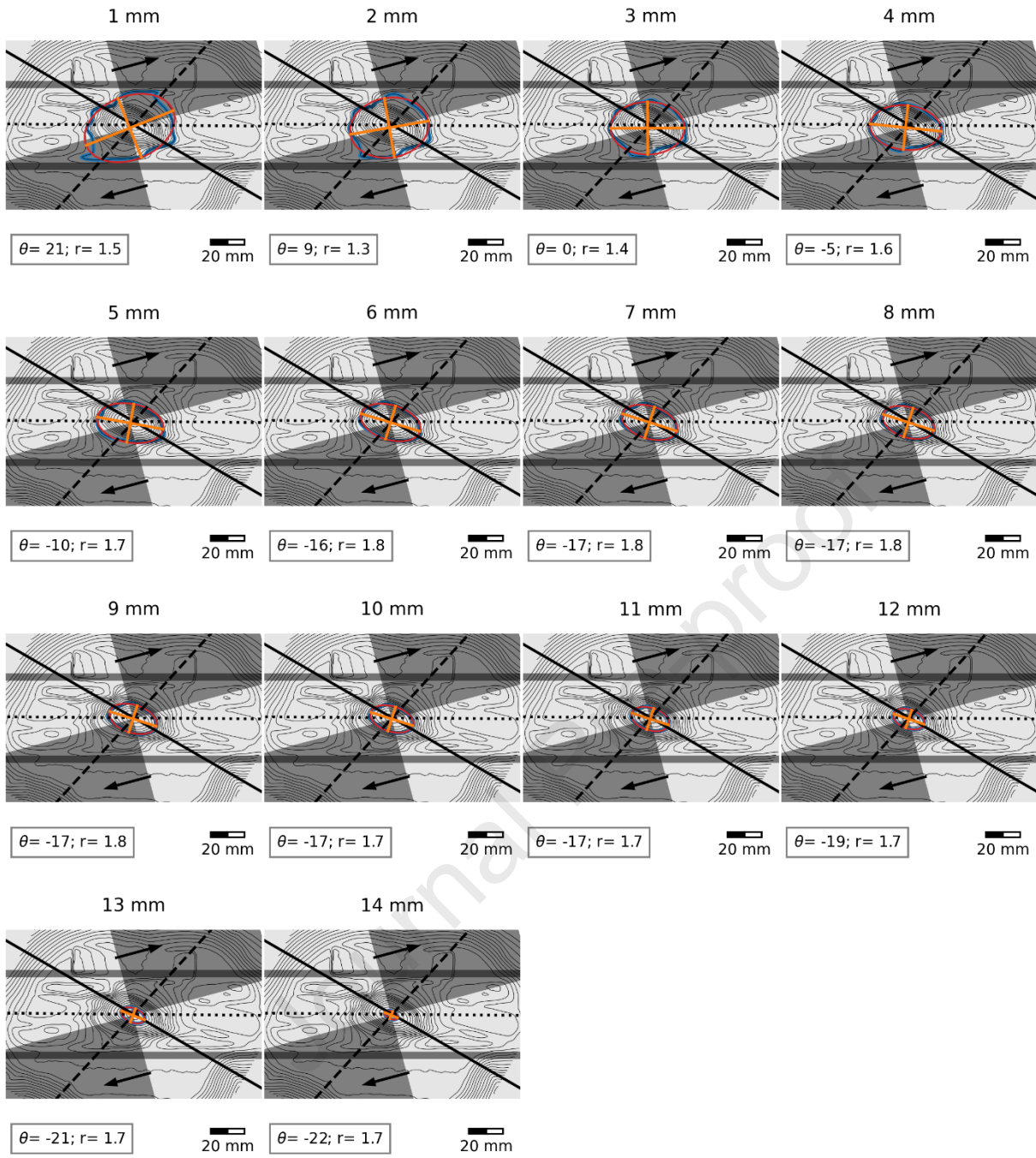
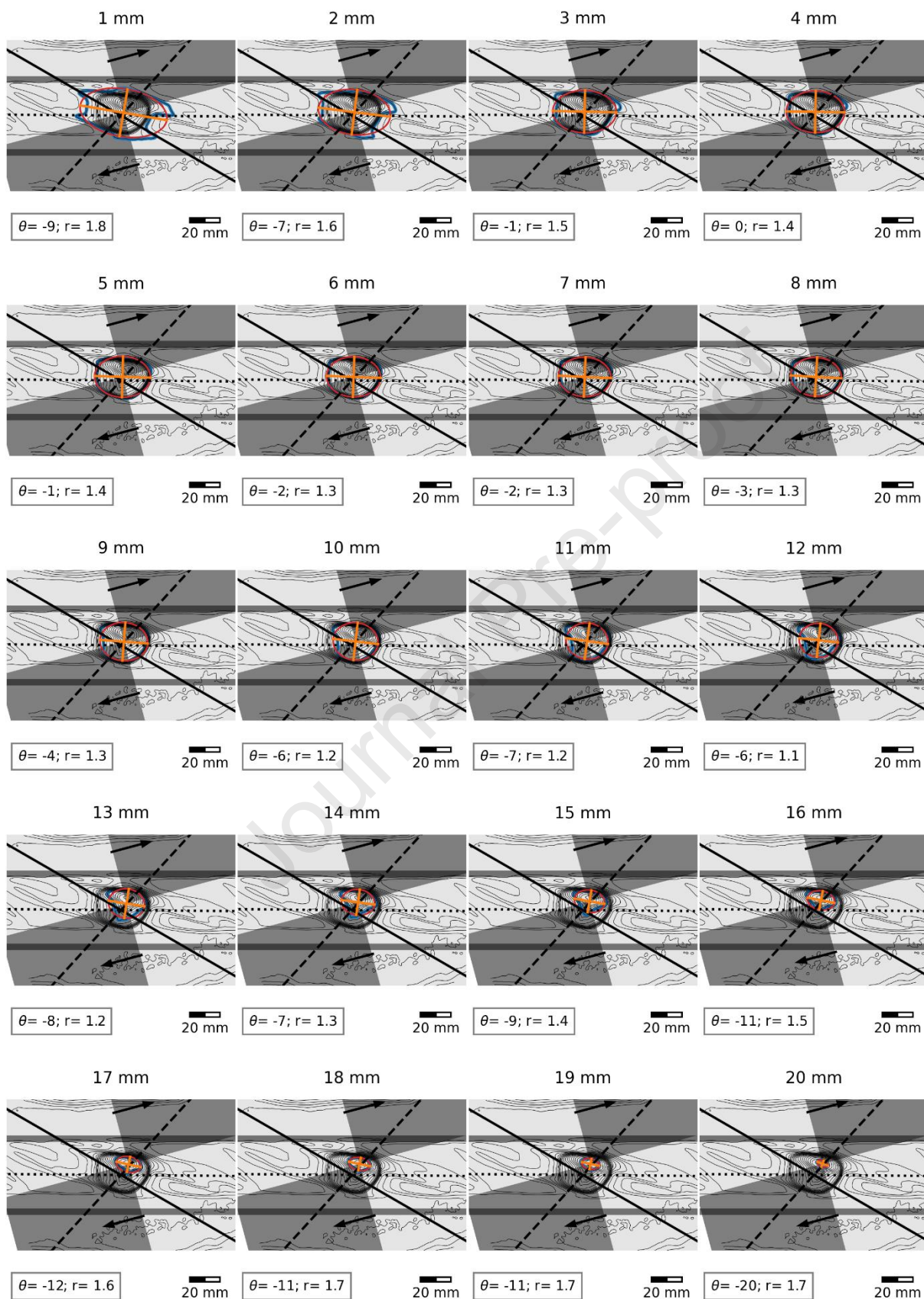


**Figure A.5:** Complete contour ellipses analysis of Model B1 shape as a function of height



**A.6 Complete contour ellipses analysis of Model B2 shape as a function of height**



# A.7 Complete contour ellipses analysis of Model B3 shape as a function of height

**Table 1 Model characteristics and experimental conditions**

<b>Models</b>	Thickness of brittle layer	Thickness of ductile layer	Intrusion rate, $I_r$	Injected Volume, $I_v$	Relative displacement rate, $D_v$	Total horizontal displacement, $D_t$	Experiment Duration
<b>Reference models (Group R)</b>							
Simple shear RS	40mm	7mm	-	-	1.0 mm/min	30 mm	30 min
Transtension RT	40mm	7mm	-	-	1.0 mm/min	30 mm	30 min
Static Intrusion R0	40mm	7mm	21.0 mm <sup>3</sup> /s	37.7x10 <sup>3</sup> mm <sup>3</sup>	-	-	30 min
<b>Simple shear models (Group A)</b>							
Pre-tectonic intrusion A1	40mm	7mm	21.0 mm <sup>3</sup> /s	37.7x10 <sup>3</sup> mm <sup>3</sup>	1.0 mm/min	30 mm	60 min
Syn-Tectonic Intrusion A2	40mm	7mm	21.0 mm <sup>3</sup> /s	37.7x10 <sup>3</sup> mm <sup>3</sup>	1.0 mm/min	30 mm	30 min
Post-tectonic intrusion A3	40mm	7mm	21.0 mm <sup>3</sup> /s	37.7x10 <sup>3</sup> mm <sup>3</sup>	1.0 mm/min	30 mm	60 min
<b>Transtension models (Group B)</b>							
Pre-tectonic intrusion B1	40mm	7mm	21.0 mm <sup>3</sup> /s	37.7x10 <sup>3</sup> mm <sup>3</sup>	1.0 mm/min	30 mm	60 min
Syn-Tectonic Intrusion B2	40mm	7mm	21.0 mm <sup>3</sup> /s	37.7x10 <sup>3</sup> mm <sup>3</sup>	1.0 mm/min	30 mm	30 min
Post-tectonic intrusion B3	40mm	7mm	21.0 mm <sup>3</sup> /s	37.7x10 <sup>3</sup> mm <sup>3</sup>	1.0 mm/min	30 mm	60 min

**Table 2 Material properties and scaling factors**

Parameters	Models	Nature	Model/ Nature (Scaling factor)
Brittle material	Quartz Sand	Upper Crust	
Length, L	0.01 m	0.6 - 6 km	$0.6 - 6 \times 10^{-6}$
Cohesion, C	10-100 Pa	10 MPa	$1-10 \times 10^{-6}$
Density, $\rho$	1600 Kg/m	2600 kg/m	0.615
Gravity, g	9.81 m/s	9.81 m/s	1
Viscous material	Silicone oil	Intrusion/ shear zone	
Viscosity, $\eta$	$3 \times 10^4$ Pa s	$>10^{18}$ Pa s	$3.0 \times 10^{-14}$
Density, $\rho$	965 kg/m	1600 kg/m	0.603
Time, t	1 sec	30000 yrs	$10^{-13}$

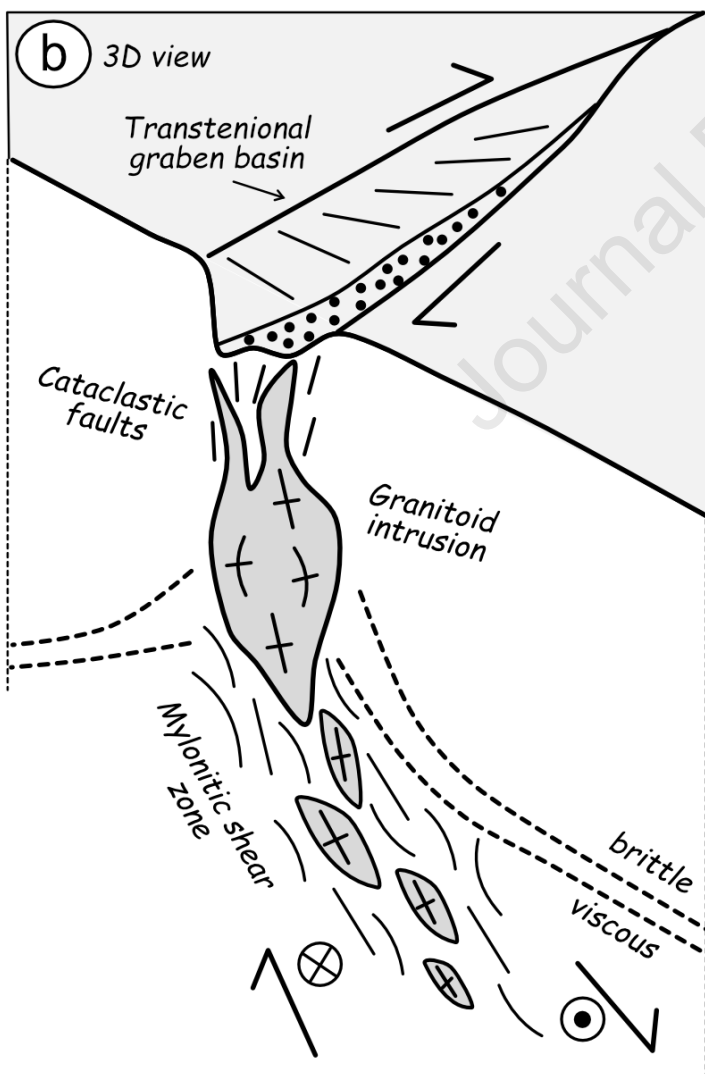
**Table 3 Summarizing table of diagnostic attributes as suggested by the analogue models for the different emplacement scenarios and kinematic settings.**

Model	Pluton Elongation $r = L/W^a$		Orientation $\Theta^a$		Dike system		Pluton amplitude A	
	<i>Simple shear (A)</i>	<i>Transtension (B)</i>	<i>Simple shear (A)</i>	<i>Transtension (B)</i>	<i>Simple shear (A)</i>	<i>Transtension (B)</i>	<i>Simple shear (A)</i>	<i>Transtension (B)</i>
<b>Pre-tectonic</b>	<b>Very high</b> ( $r_{A1} > 3$ )	<b>Medium</b> ( $r_{B1} > 1.5$ )	Long axis // <b>extension</b>	Long axis // <b>extension</b>	Roof & lateral	Lateral	<b>Low</b>	<b>Very low</b>
<b>Syn-Tectonic</b>	<b>High</b> ( $r_{A2} > 2$ )	<b>Medium<sup>b</sup></b> ( $r_{B2} > 1.5$ )	Long axis // <b>Riedel</b>	Long axis // <b>compression</b>	Lateral & apophysis	Roof & lateral & apophysis	<b>High</b>	<b>High</b>
<b>Post-tectonic</b>	<b>Low</b> ( $r_{A3} < 2$ )	<b>Low</b> ( $r_{B3} < 2$ )	Long axis // <b>Riedel</b>	Long axis // <b>Riedel</b>	Roof & lateral	Roof & lateral	<b>Medium</b>	<b>Medium</b>

<sup>a</sup> Based on an ellipse fitted to the lower ( $C_1$ ) and higher ( $C_2$ ) contour level of the intrusion.

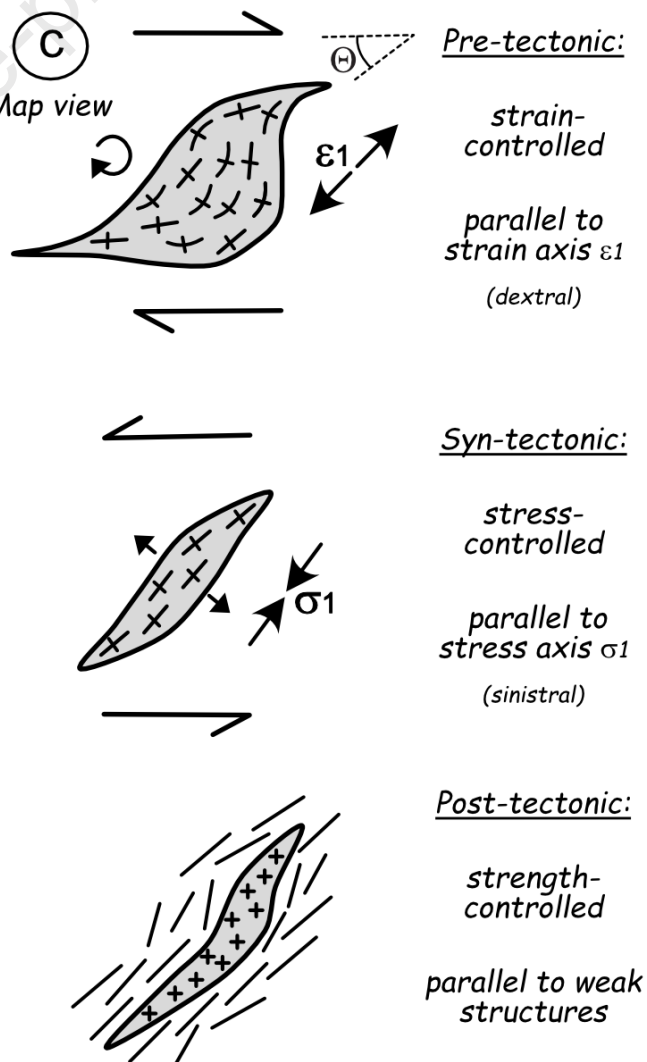
<sup>b</sup> Based on repetition models (100, 59, 95; see Appendix A.1)

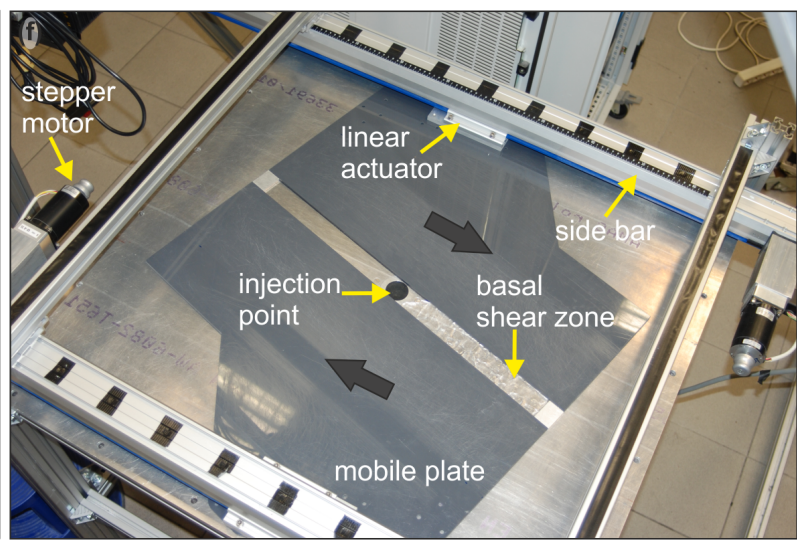
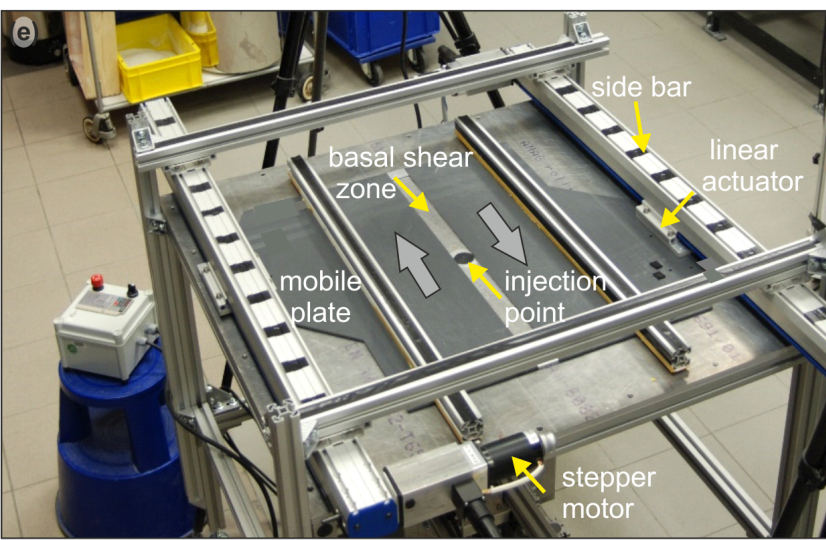
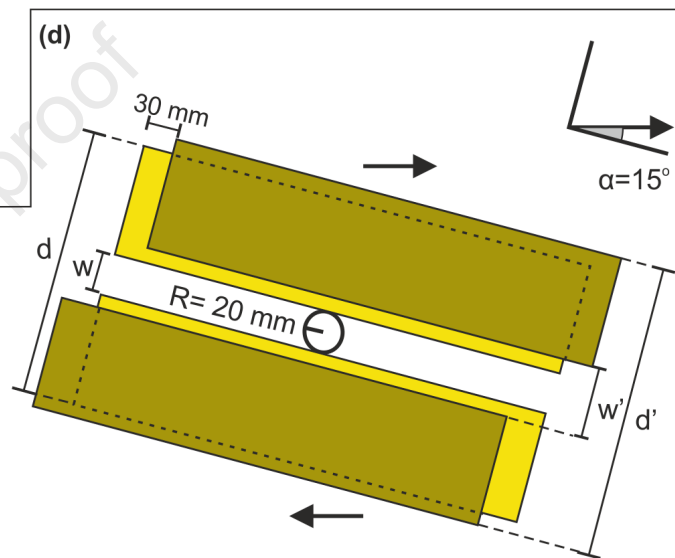
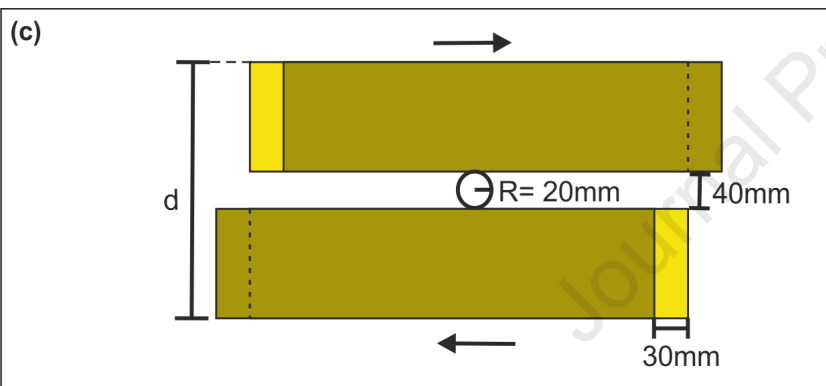
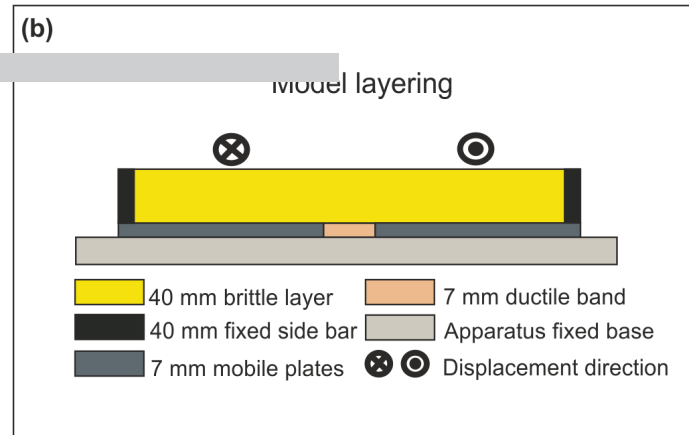
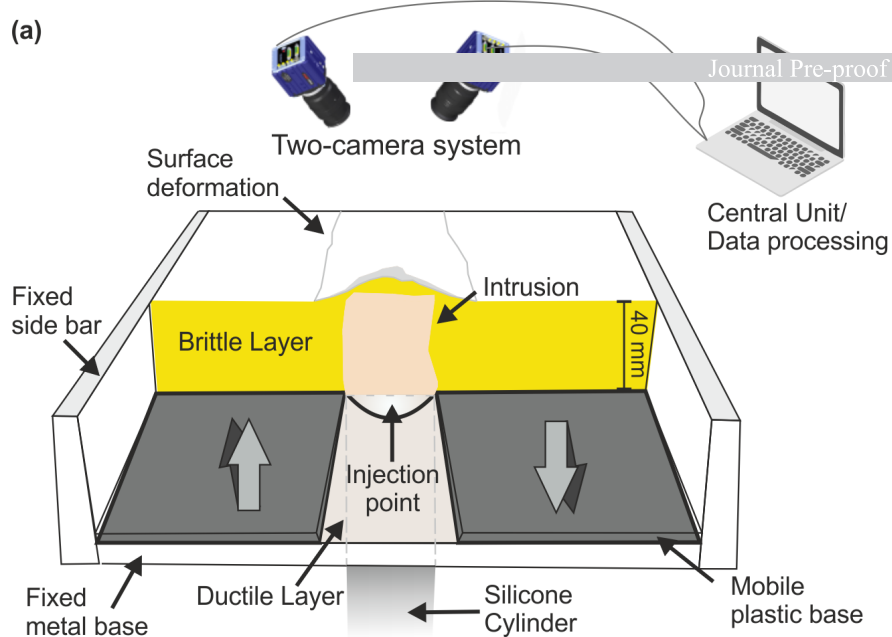
a

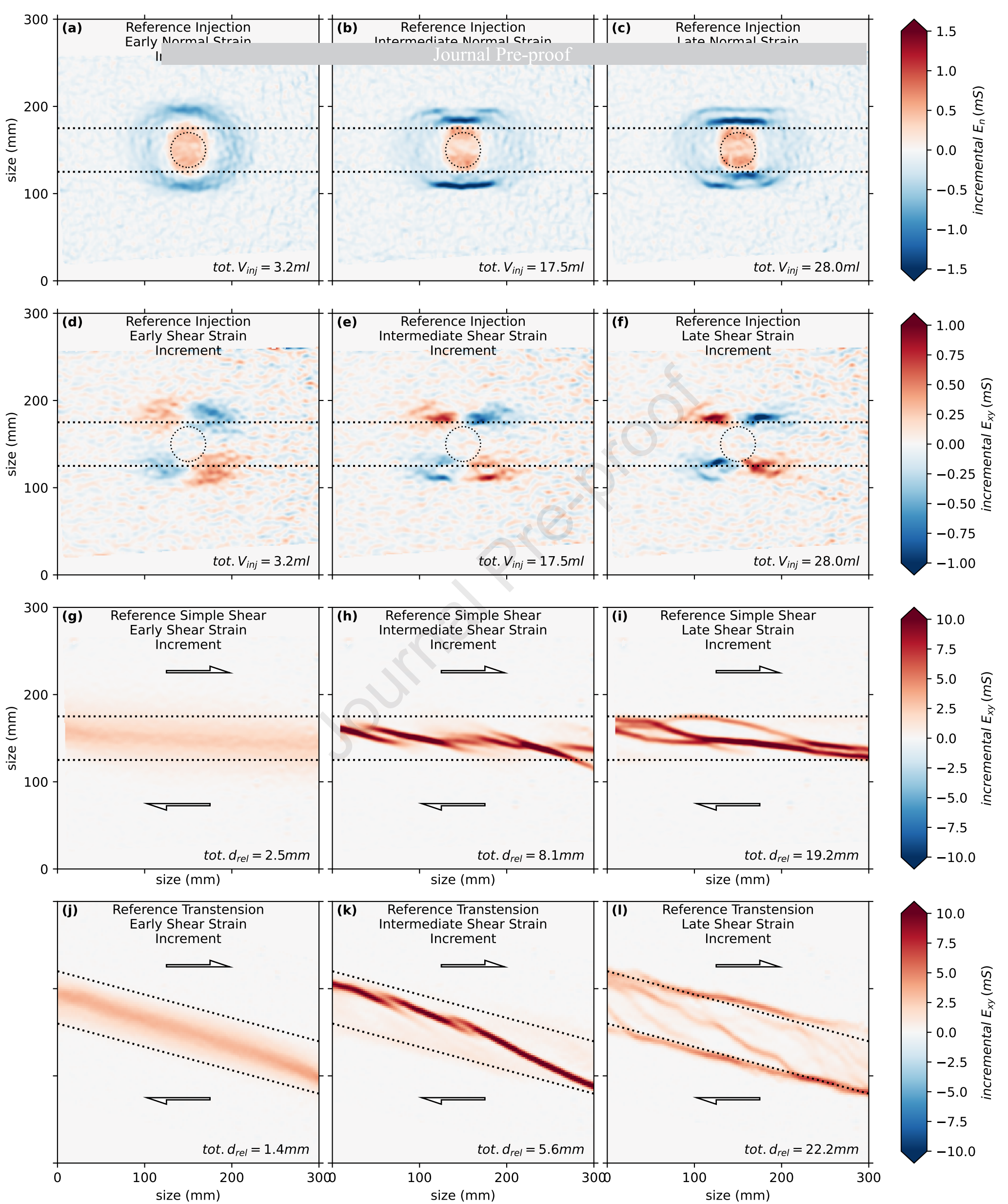


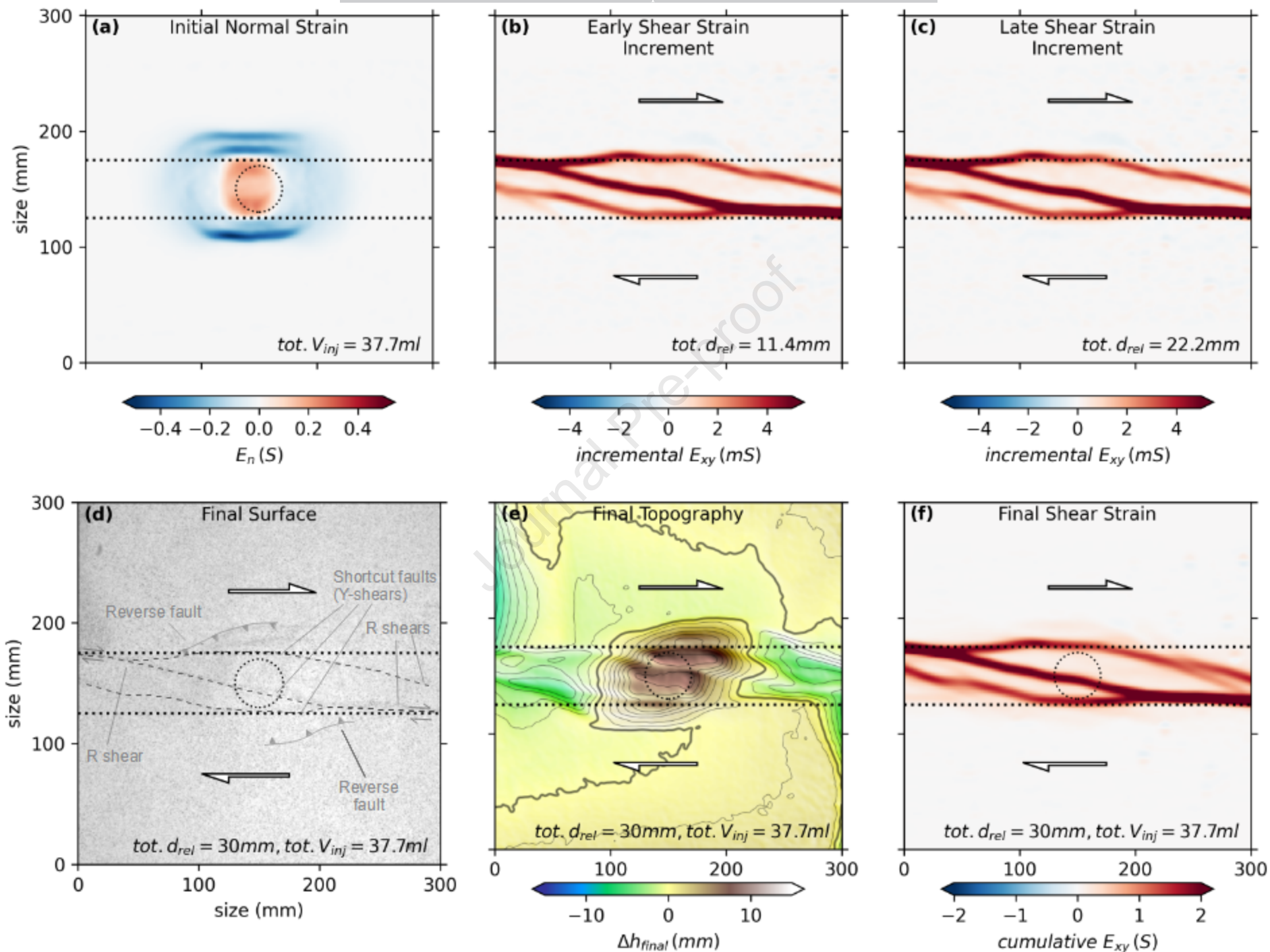
c

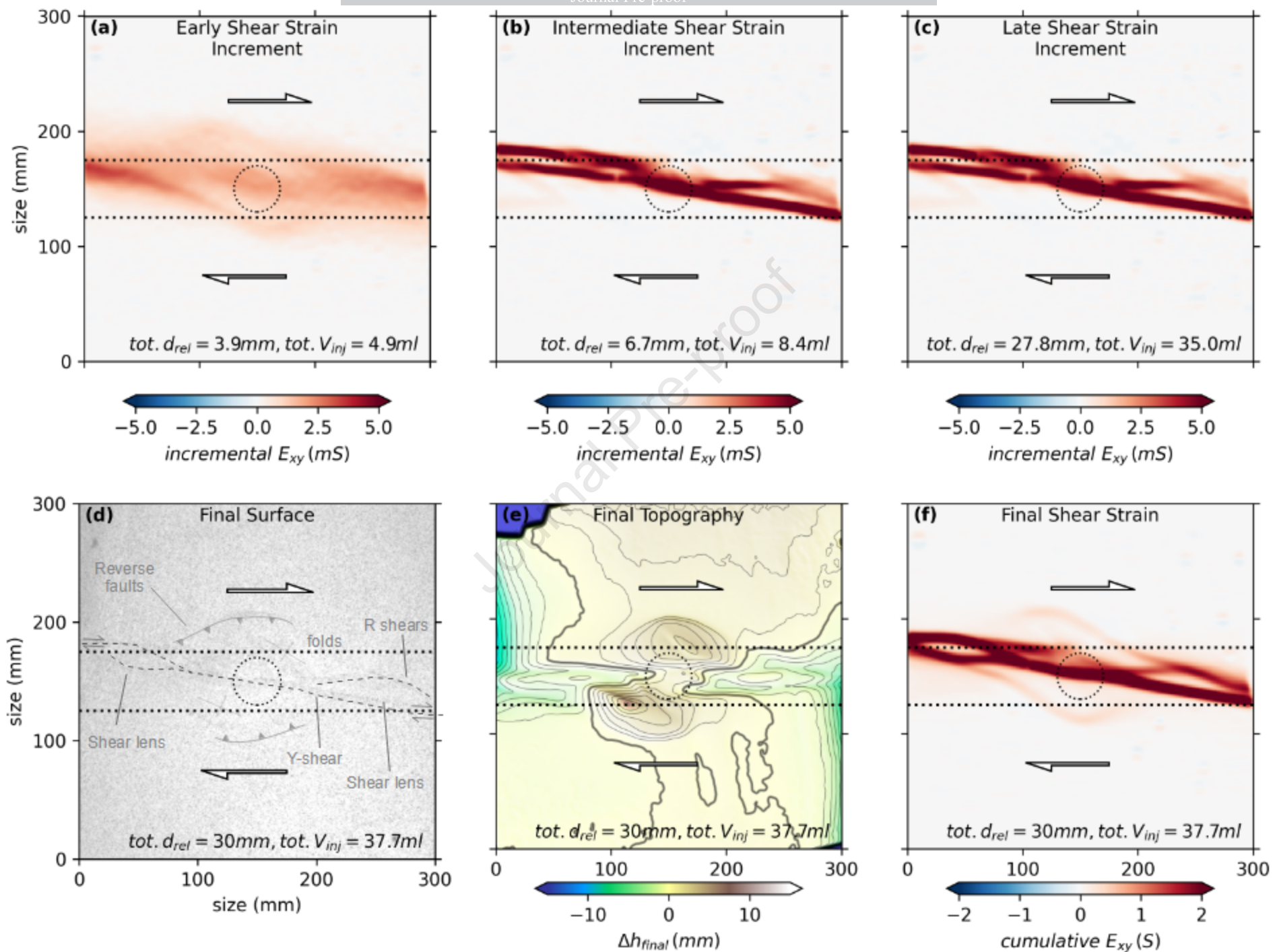
Map view

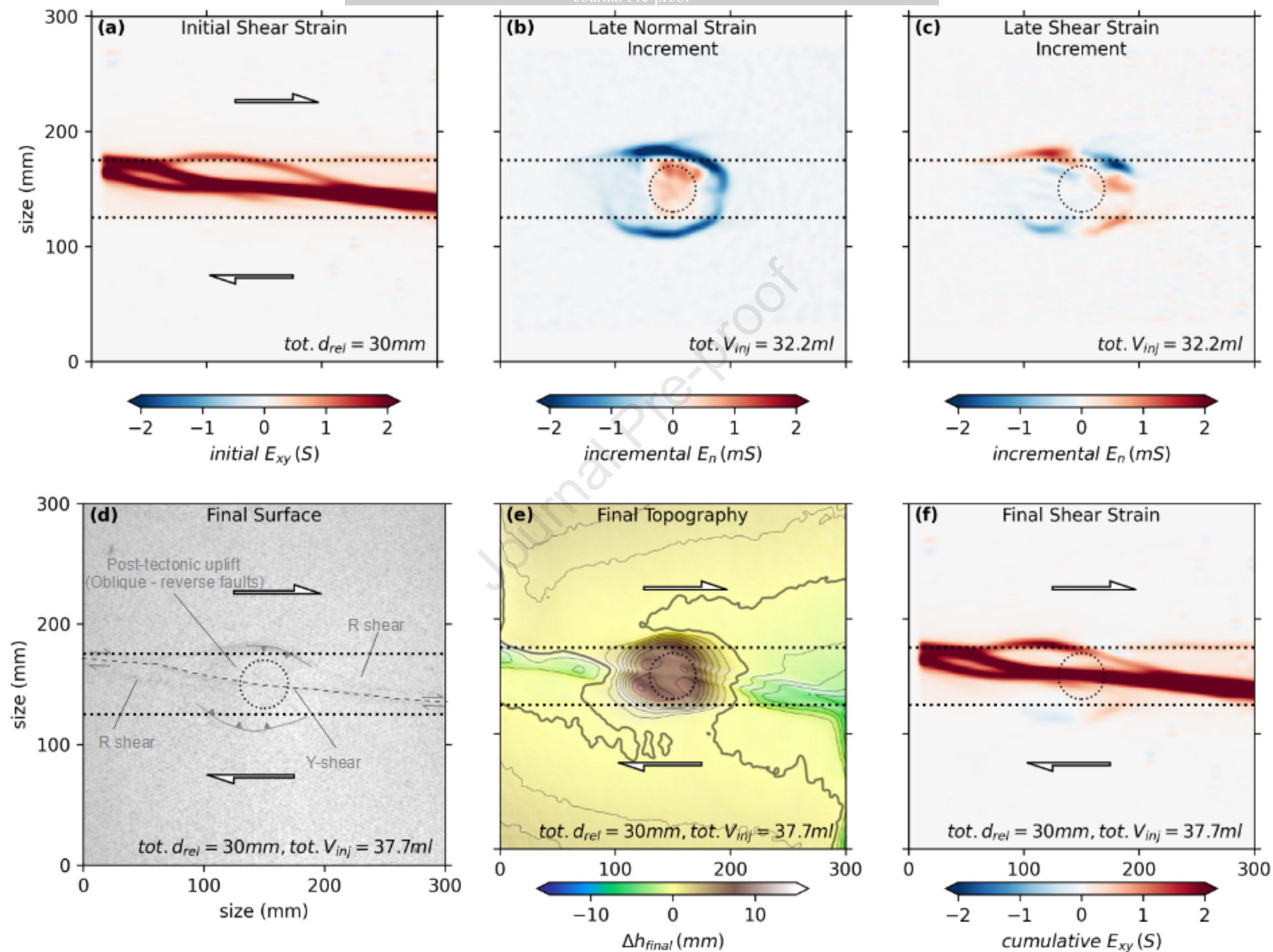




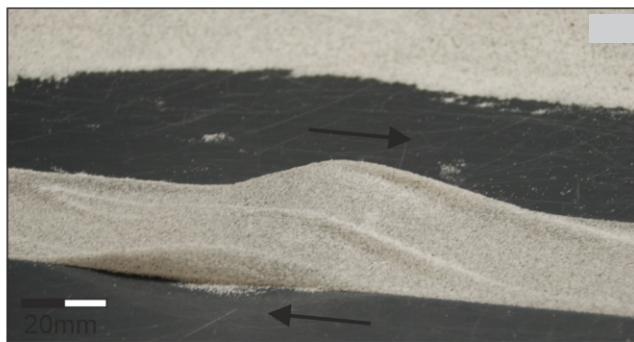








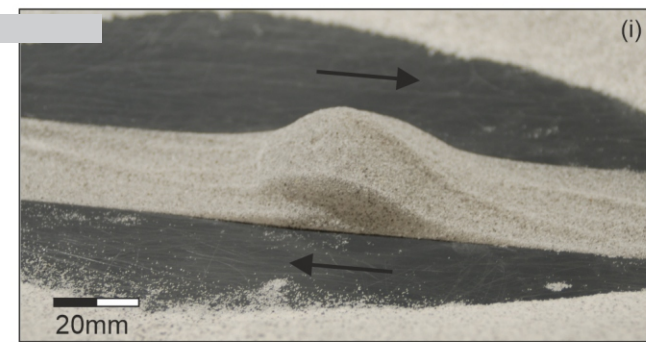
Model A1



Model A2

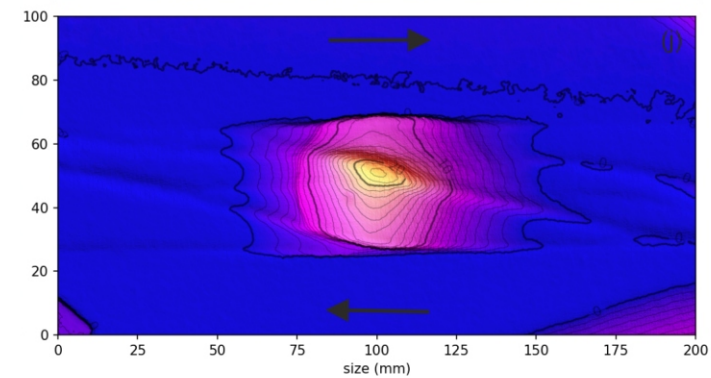
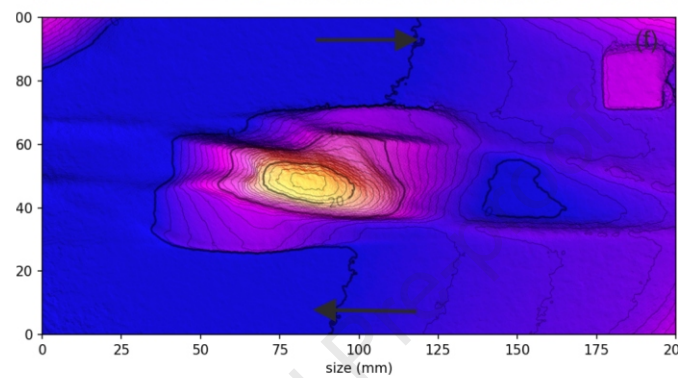
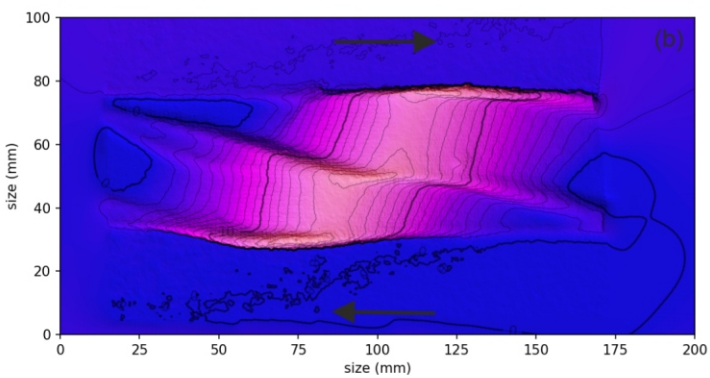


Model A3

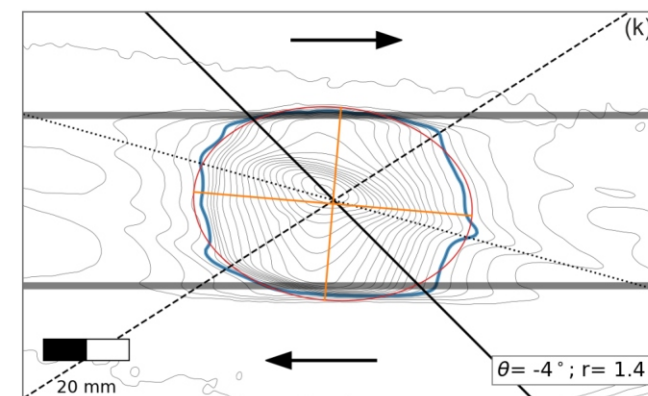
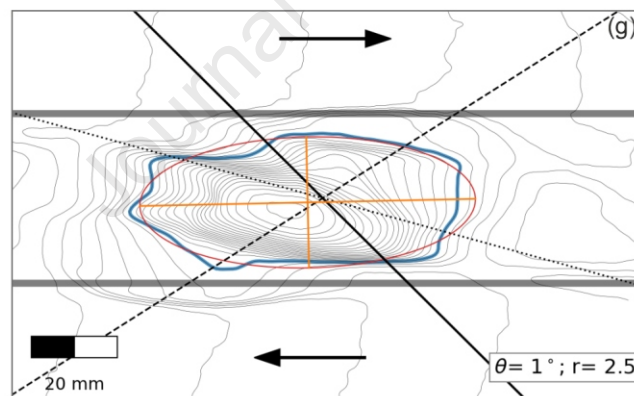
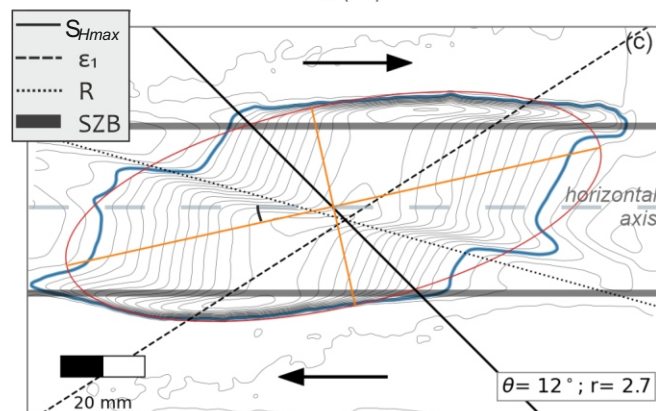
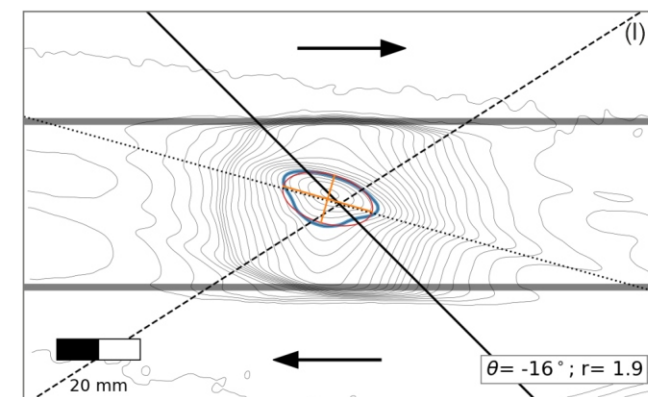
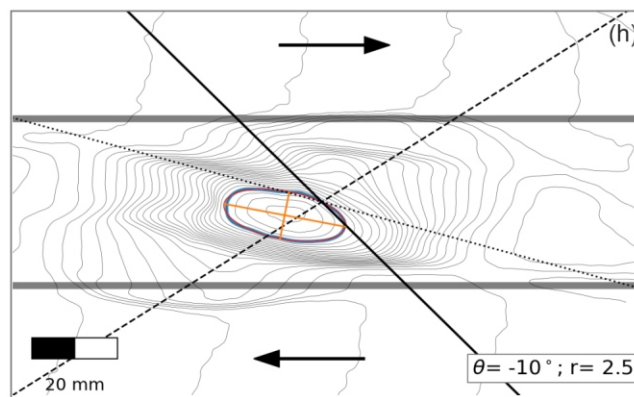
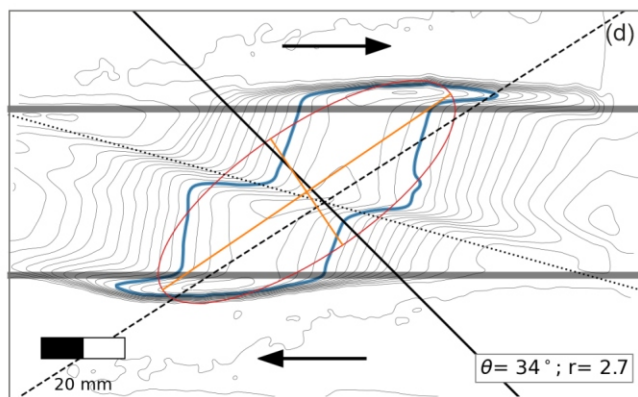


Journal Pre-proof

(i)



height (mm)

Low contour level ( $c_1$ )High contour level ( $c_2$ )

$S_{Hmax}$   
 $\epsilon_1$   
 $R$   
 $SZB$

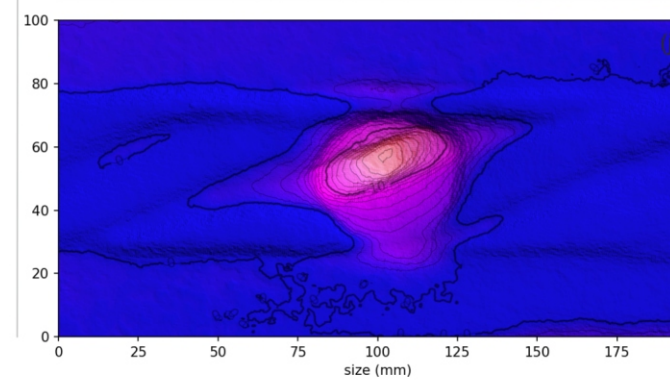
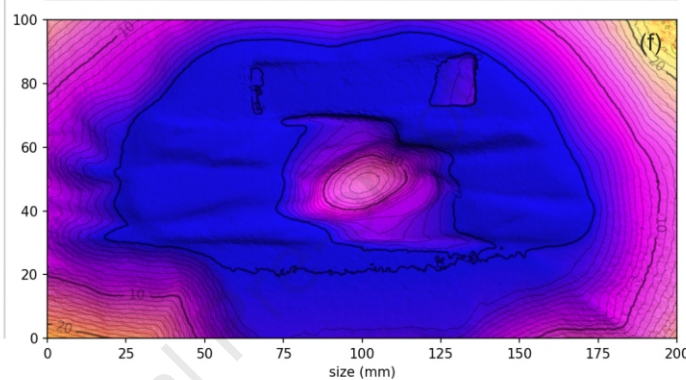
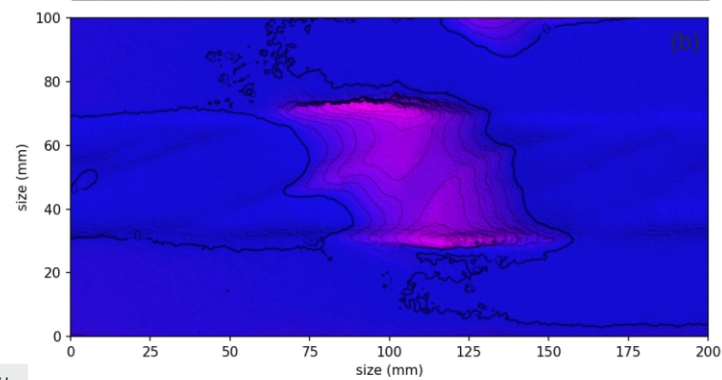
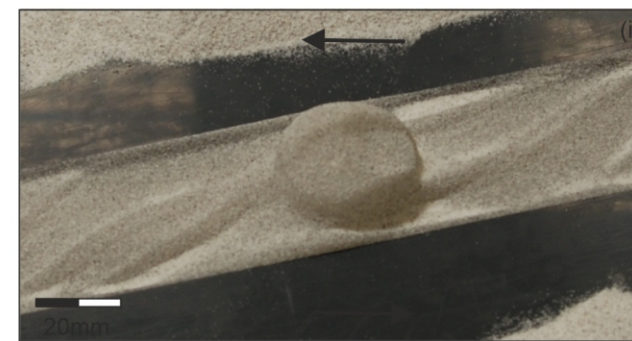
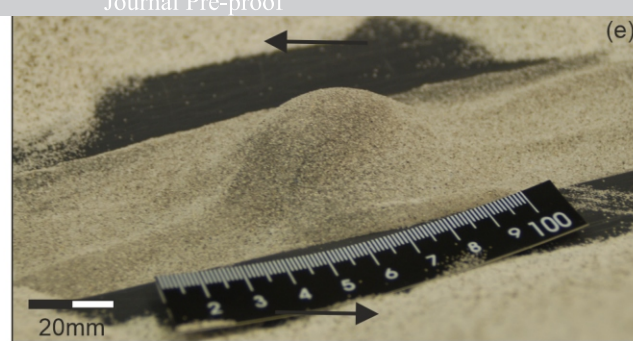
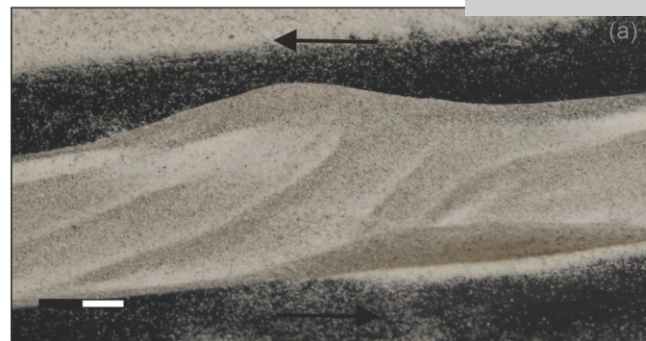
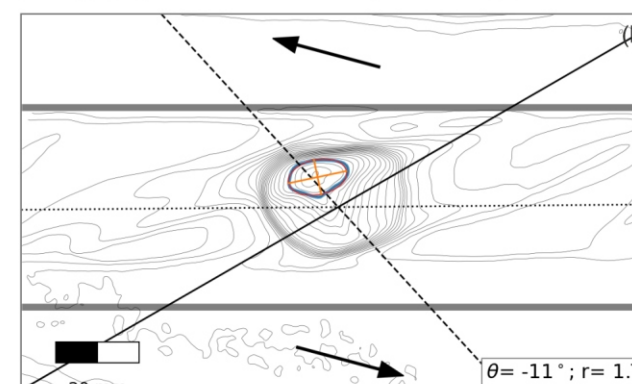
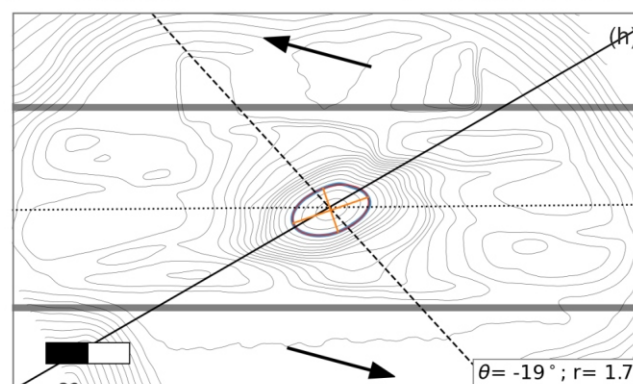
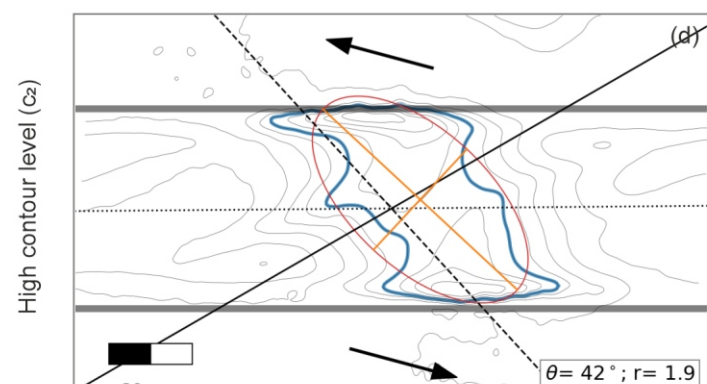
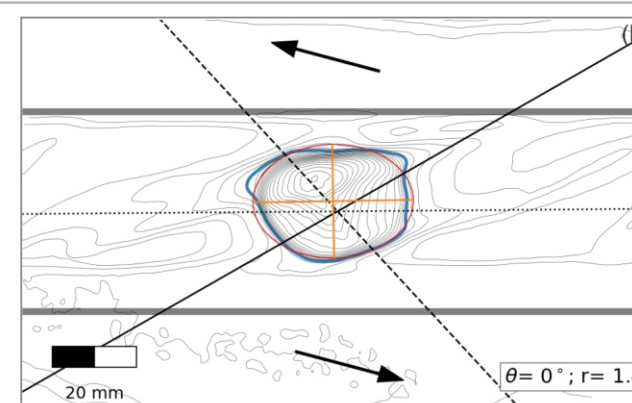
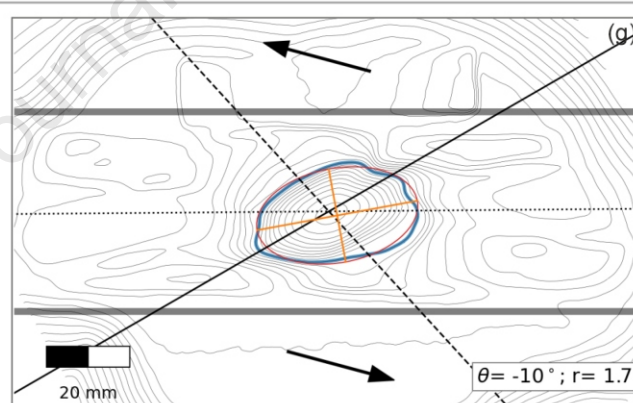
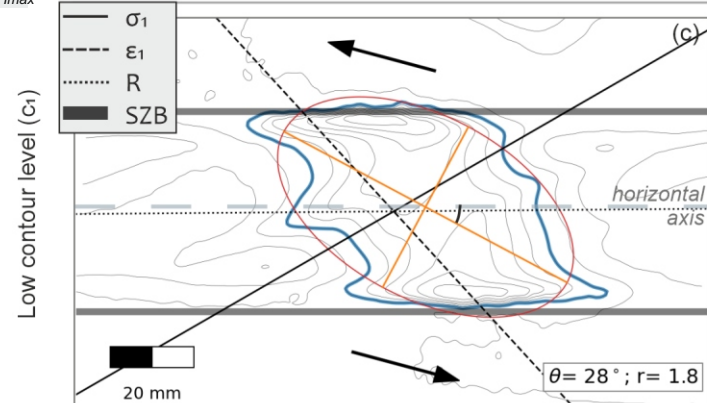
 $\theta = 12^\circ; r = 2.7$  $\theta = 1^\circ; r = 2.5$  $\theta = -4^\circ; r = 1.4$  $\theta = 34^\circ; r = 2.7$  $\theta = -10^\circ; r = 2.5$  $\theta = -16^\circ; r = 1.9$

Model B1

Model B2

Model B3

Journal Pre-proof

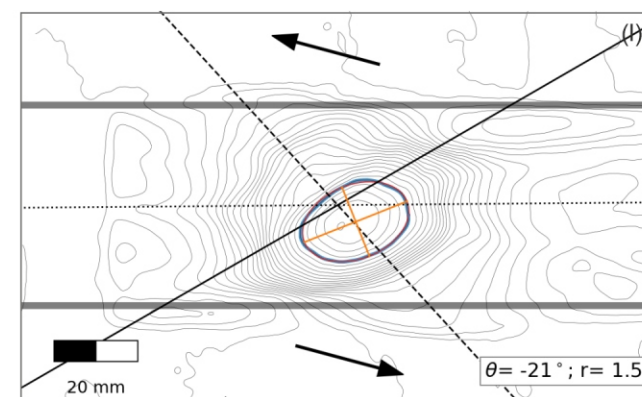
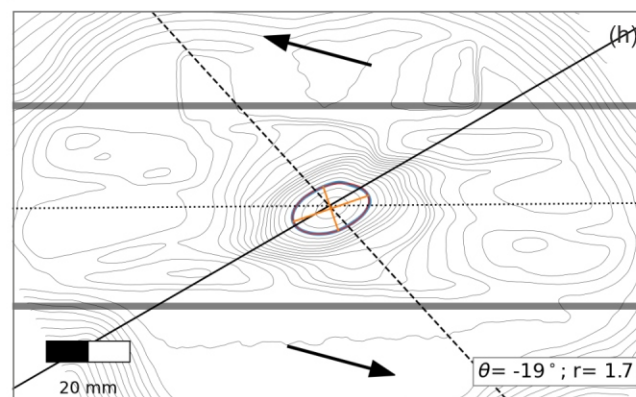
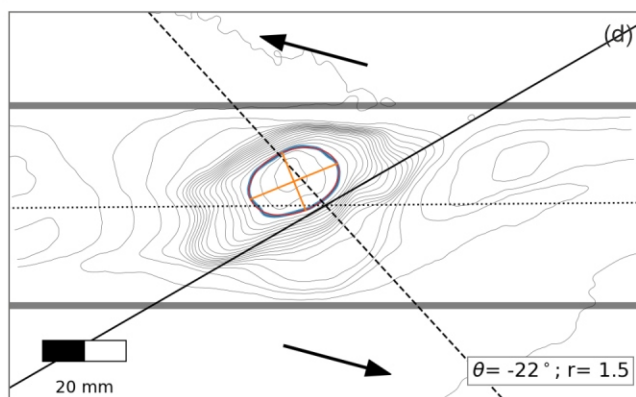
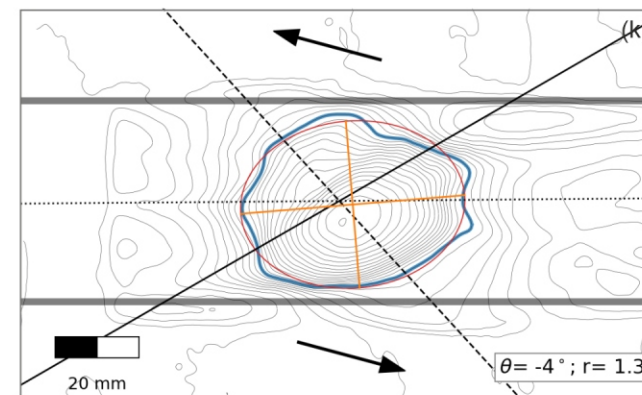
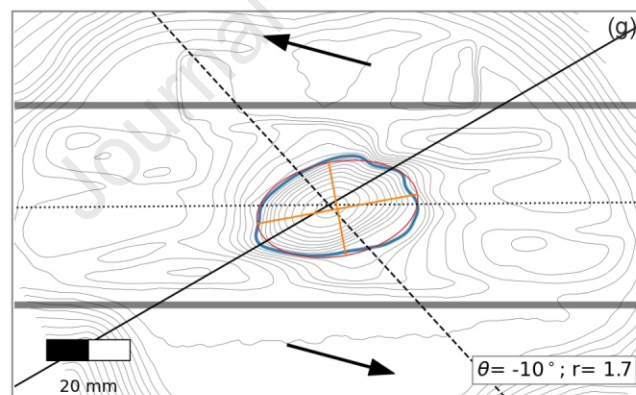
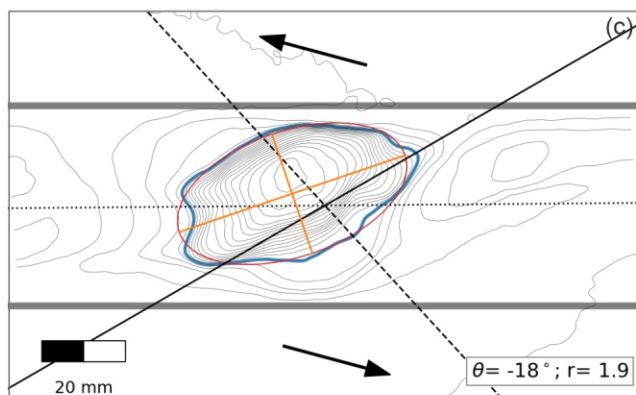
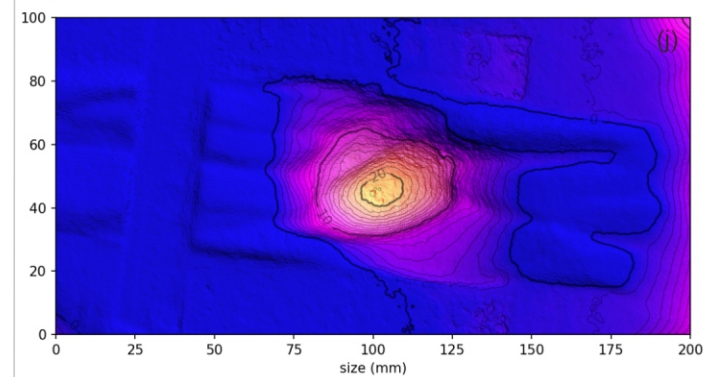
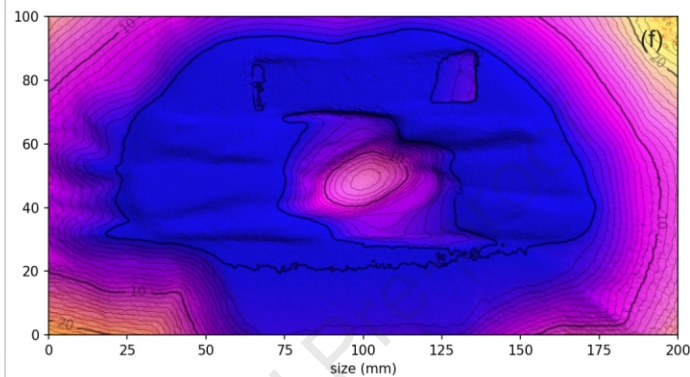
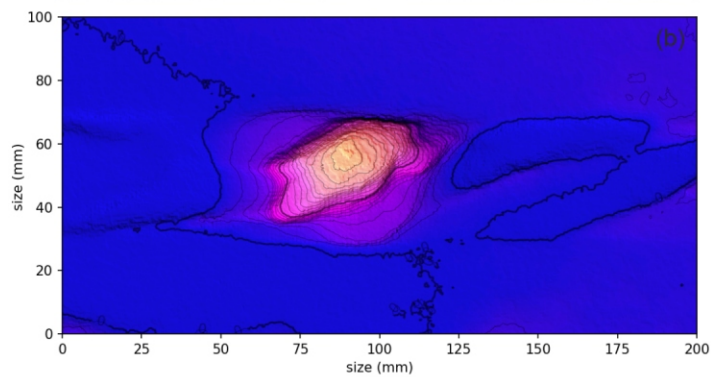
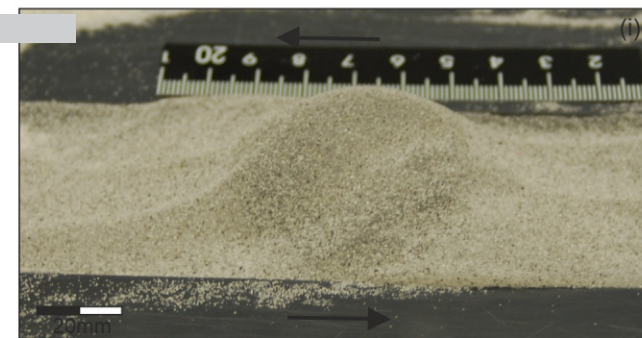
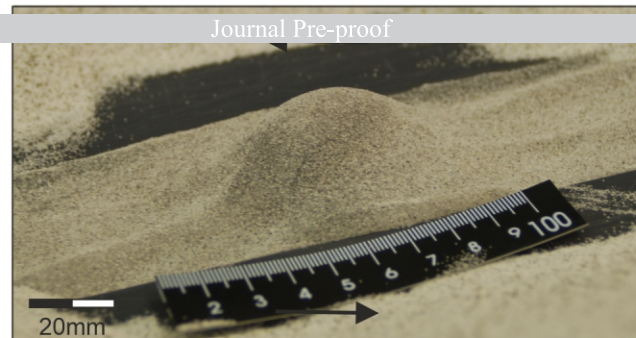
 $S_{Hmax}$ 

Model - 59

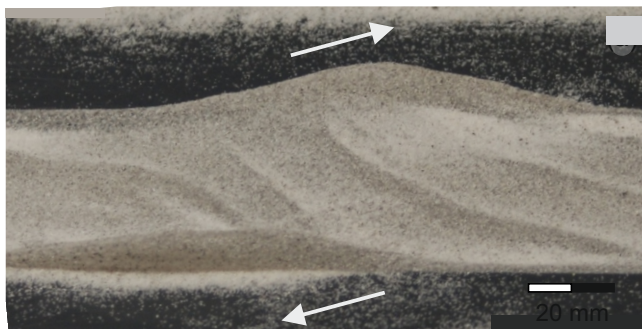
Model - 95

Model - 100

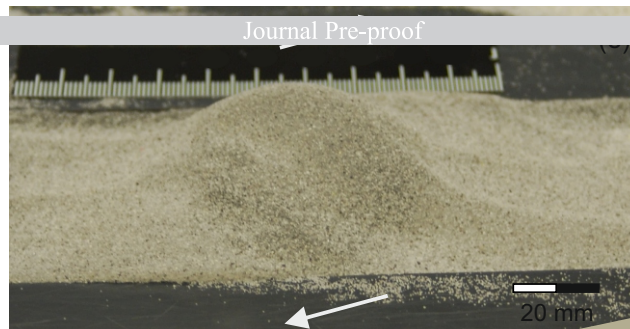
Journal Pre-proof



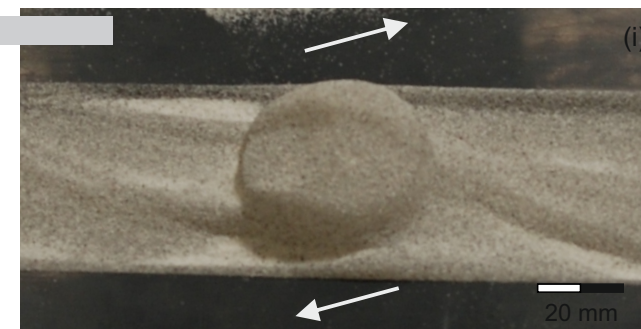
Model B1



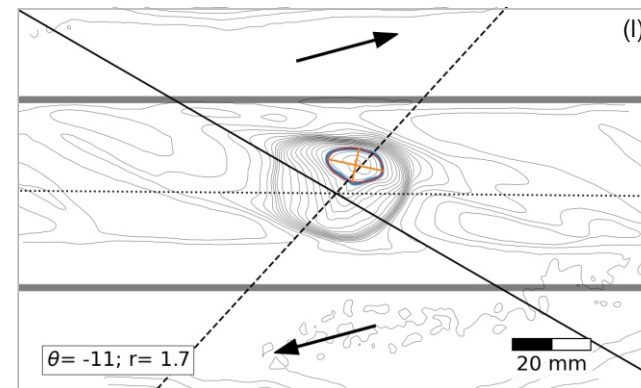
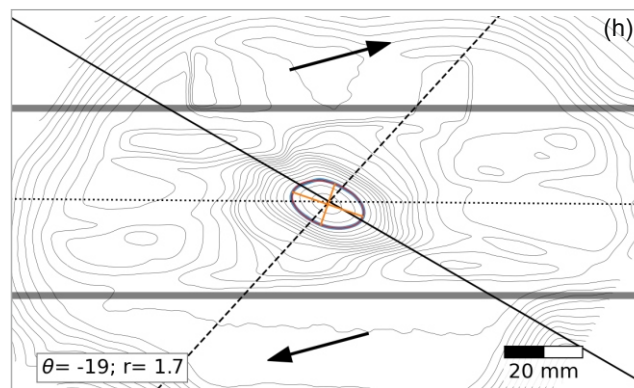
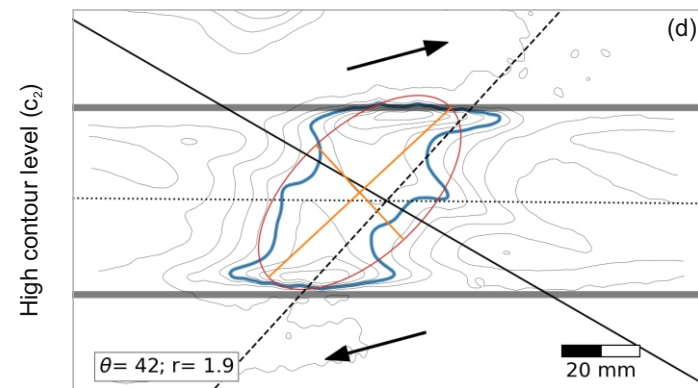
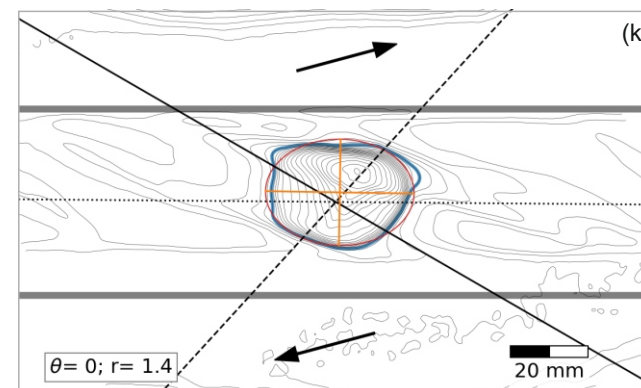
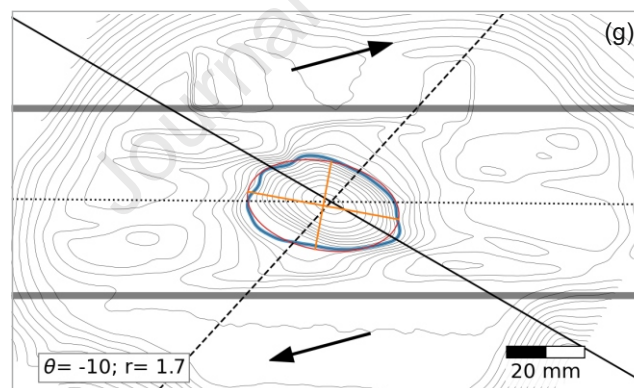
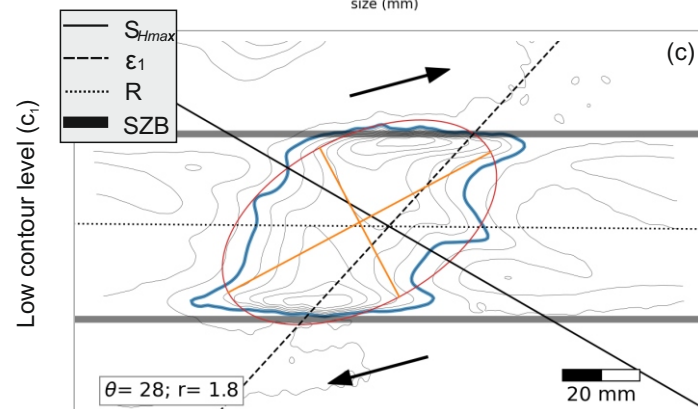
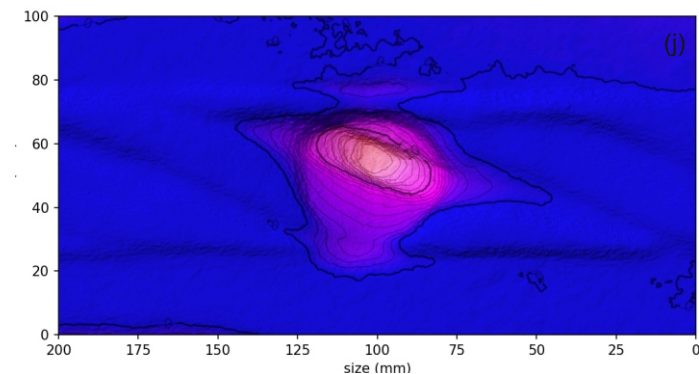
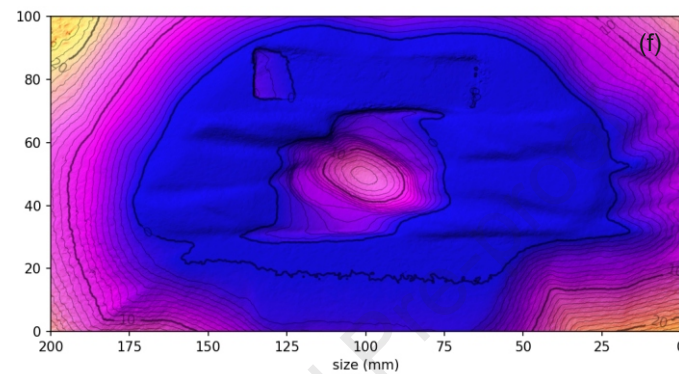
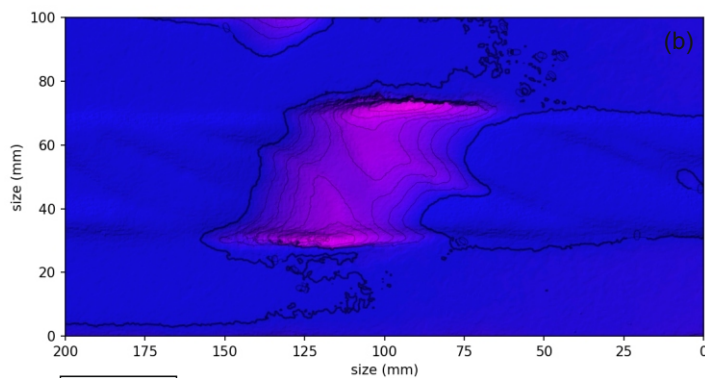
Model B2



Model B3



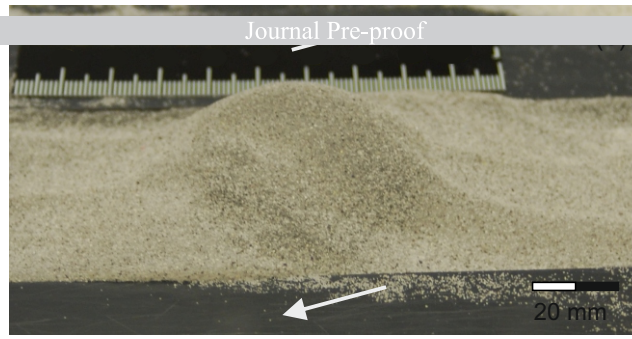
Journal Pre-proof



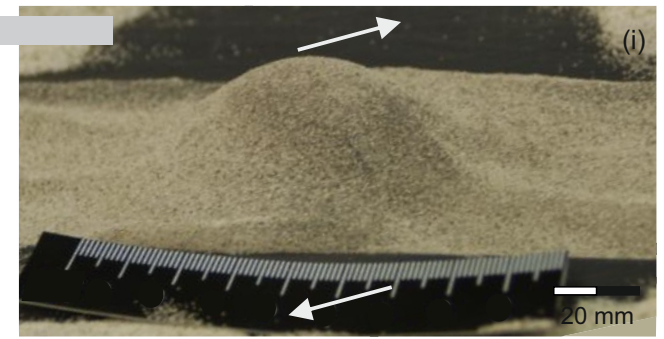
Model 59



Model 95



Model 100



Journal Pre-proof

(i)

height (mm)

30  
25  
20  
15  
10  
5  
0

(j)

(k)

(l)

(m)

(n)

(o)

(p)

(q)

(r)

(s)

(t)

(u)

(v)

(w)

(x)

(y)

(z)

(aa)

(ab)

(ac)

(ad)

(ae)

(af)

(ag)

(ah)

(ai)

(aj)

(ak)

(al)

(am)

(an)

(ao)

(ap)

(aq)

(ar)

(as)

(at)

(au)

(av)

(aw)

(ax)

(ay)

(az)

(ba)

(bb)

(bc)

(bd)

(be)

(bf)

(bg)

(bh)

(bi)

(bj)

(bk)

(bl)

(bm)

(bn)

(bo)

(bp)

(bq)

(br)

(bs)

(bt)

(bu)

(bv)

(bw)

(bx)

(by)

(bz)

(ca)

(cb)

(cc)

(cd)

(ce)

(cf)

(cg)

(ch)

(ci)

(cj)

(ck)

(cl)

(cm)

(cn)

(co)

(cp)

(cq)

(cr)

(cs)

(ct)

(cu)

(cv)

(cw)

(cx)

(cy)

(cz)

(da)

(db)

(dc)

(dd)

(de)

(df)

(dg)

(dh)

(di)

(dj)

(dk)

(dl)

(dm)

(dn)

(do)

(dp)

(dq)

(dr)

(ds)

(dt)

(du)

(dv)

(dw)

(dx)

(dy)

(dz)

(ea)

(eb)

(ec)

(ed)

(ee)

(ef)

(eg)

(eh)

(ei)

(ej)

(ek)

(el)

(em)

(en)

(eo)

(ep)

(eq)

(er)

(es)

(et)

(eu)

(ev)

(ew)

(ex)

(ey)

(ez)

(fa)

(fb)

(fc)

(fd)

(fe)

(ff)

(fg)

(fh)

(fi)

(fj)

(fk)

(fl)

(fm)

(fn)

(fo)

(fp)

(fq)

(fr)

(fs)

(ft)

(fu)

(fv)

(fw)

(fx)

(fy)

(fz)

(ga)

(gb)

(gc)

(gd)

(ge)

(gf)

(gg)

(gh)

(gi)

(gj)

(gk)

(gl)

(gm)

(gn)

(go)

(gp)

(gq)

(gr)

(gs)

(gt)

(gu)

(gv)

(gw)

(gx)

(gy)

(gz)

(ha)

(hb)

(hc)

(hd)

(he)

(hf)

(hg)

(hh)

(hi)

(hj)

(hk)

(hl)

(hm)

(hn)

(ho)

(hp)

(hq)

(hr)

(hs)

(ht)

(hu)

(hv)

(hw)

(hx)

(hy)

(hz)

(ia)

(ib)

(ic)

(id)

(ie)

(if)

(ig)

(ih)

(ii)

(ij)

(ik)

(il)

(im)

(in)

(io)

(ip)

(iq)

(ir)

(is)

(it)

(iu)

(iv)

(iw)

(ix)

(iy)

(iz)

(ja)

(jb)

(jc)

(jd)

(je)

(jf)

(jg)

(jh)

(ji)

(jj)

(jk)

(jl)

(jm)

(jn)

(jo)

(jp)

(jq)

(jr)

(js)

(jt)

(ju)

(jv)

(jw)

(jx)

(jy)

(jz)

(ka)

(kb)

(kc)

(kd)

(ke)

(kf)

(kg)

(kh)

(ki)

(kj)

(kk)

(kl)

(km)

(kn)

(ko)

(kp)

(kq)

(kr)

(ks)

(kt)

(ku)

(kv)

(kw)

(kx)

(ky)

(kz)

(la)

(lb)

(lc)

(ld)

(le)

(lf)

(lg)

(lh)

(li)

(lj)

(lk)

(ll)

(lm)

(ln)

(lo)

(lp)

(lq)

(lr)

(ls)

(lt)

(lu)

(lv)

(lw)

(lx)

(ly)

(lz)

(ma)

(mb)

(mc)

(md)

(me)

(mf)

(mg)

(mh)

(mi)

(mj)

(mk)

(ml)

(mm)

(mn)

(mo)

(mp)

(mq)

(mr)

(ms)

(mt)

(mu)

(mv)

(mw)

(mx)

(my)

(mz)

(na)

(nb)

(nc)

(nd)

(ne)

(nf)

(ng)

(nh)

(ni)

(nj)

(nk)

(nl)

(nm)

(nn)

(no)

(np)

(nq)

(nr)

(ns)

(nt)

(nu)

(nv)

(nw)

(nx)

(ny)

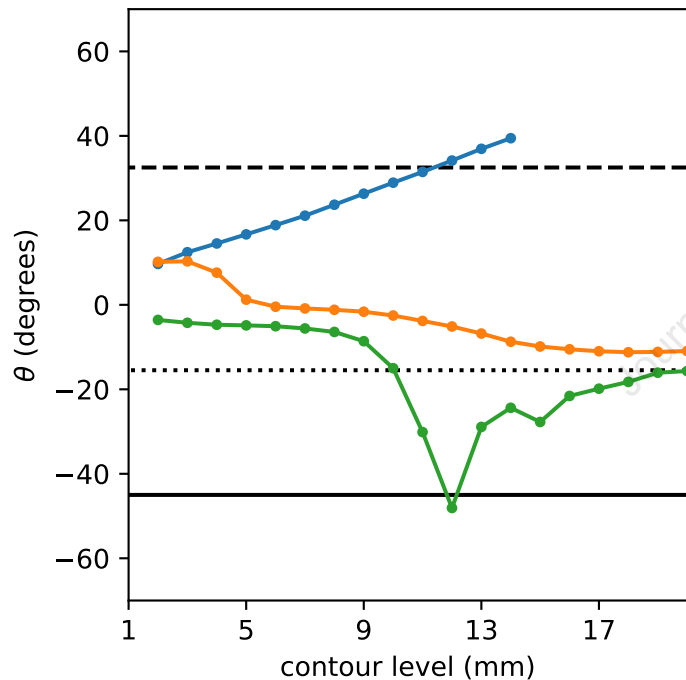
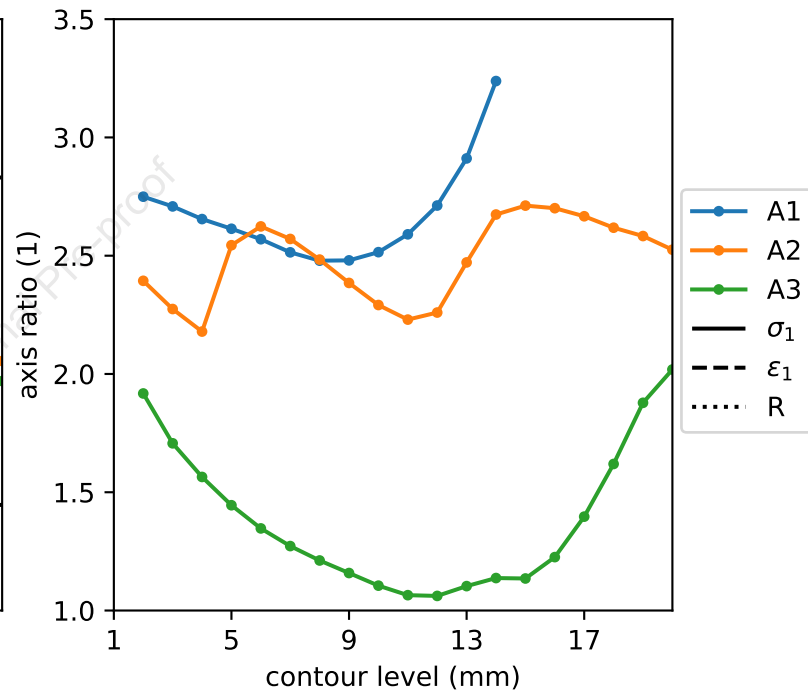
(nz)

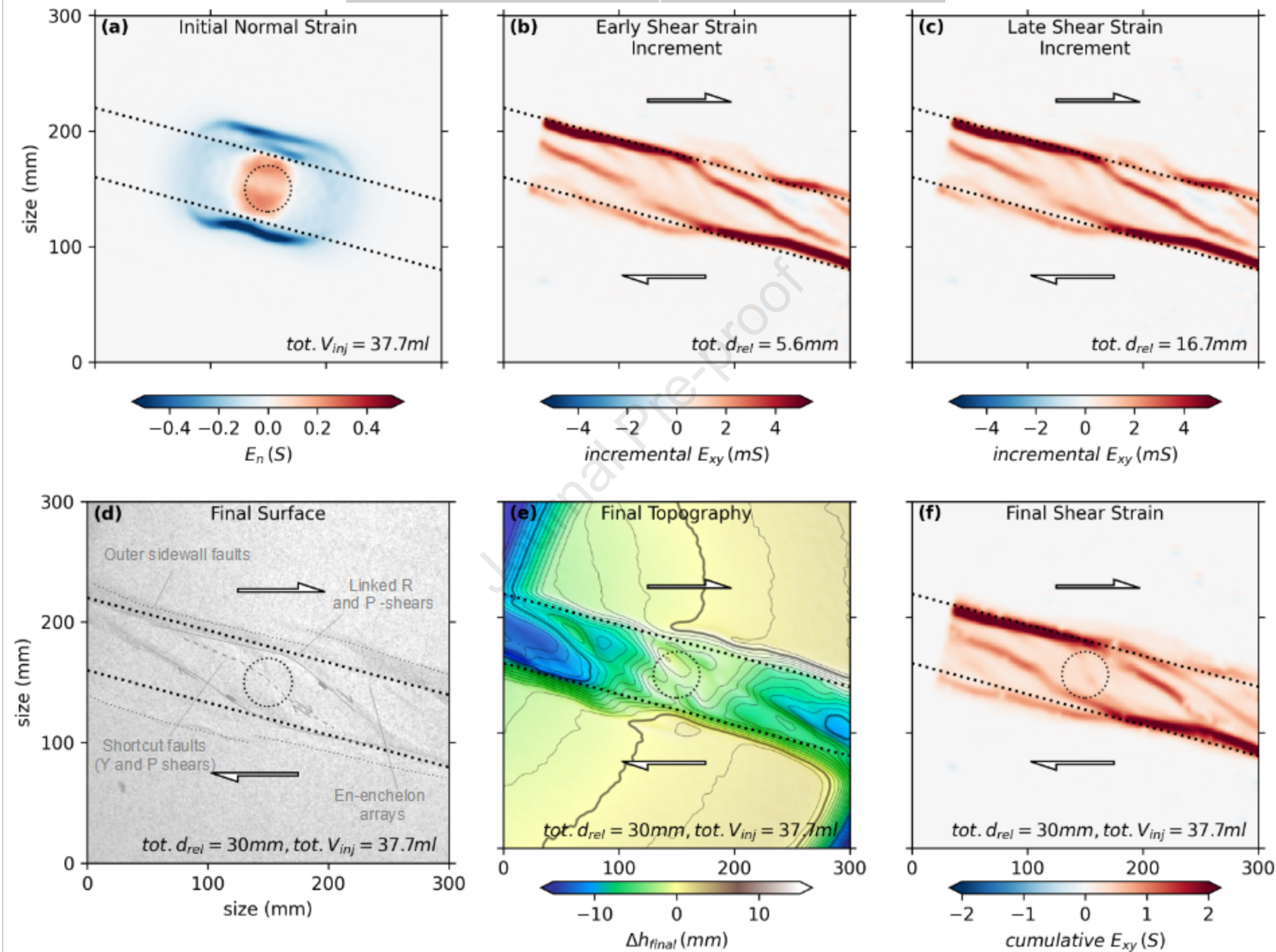
(oa)

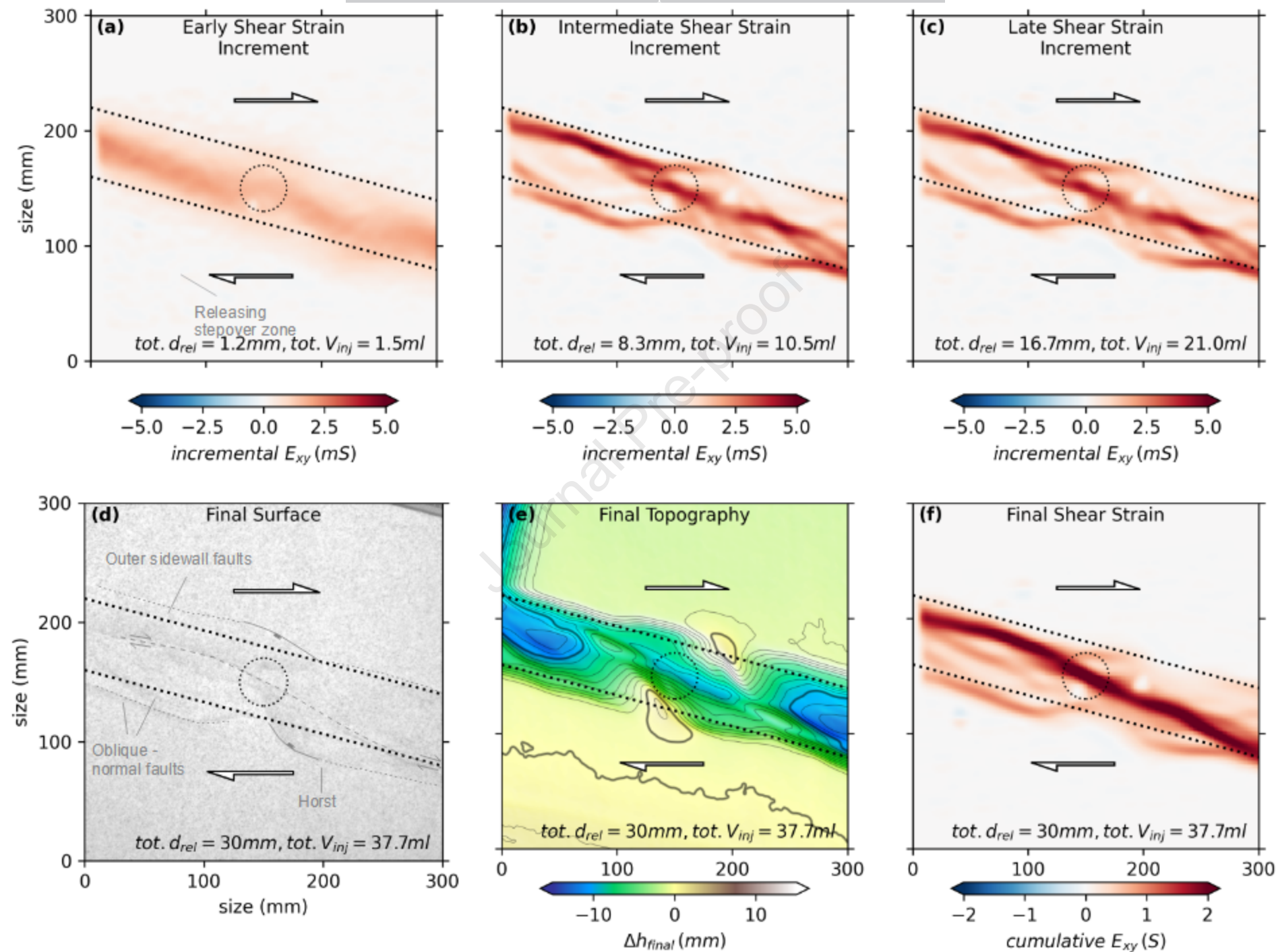
(ob)

(oc)

(od

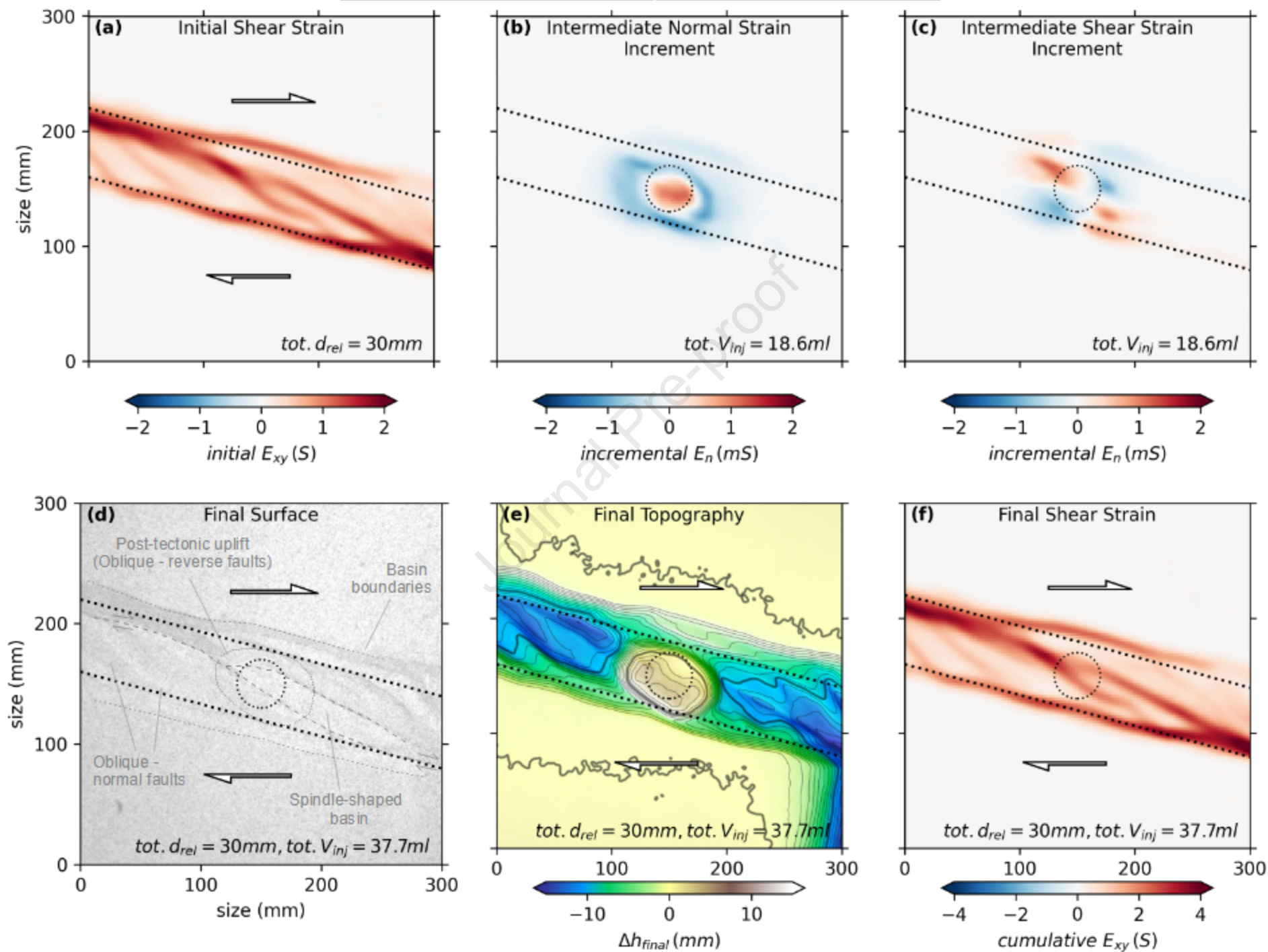
**(a)****(b)**



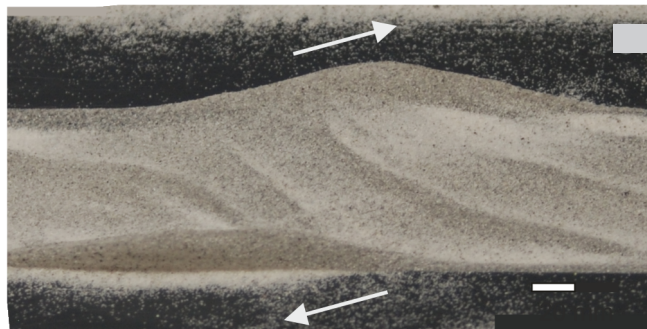


# B3 - Post-tectonic Transtension

Journal Pre-proof

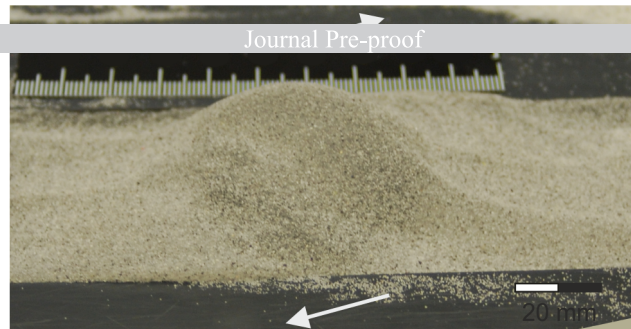


Model B1

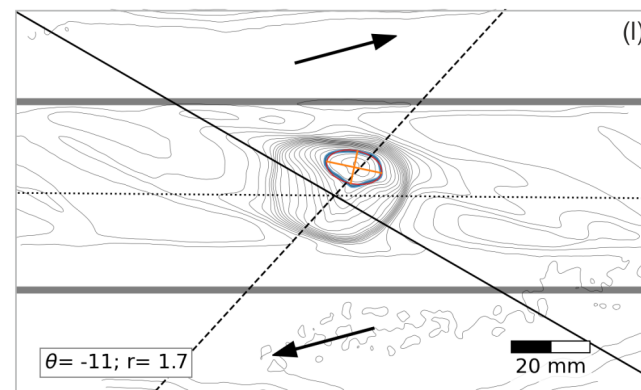
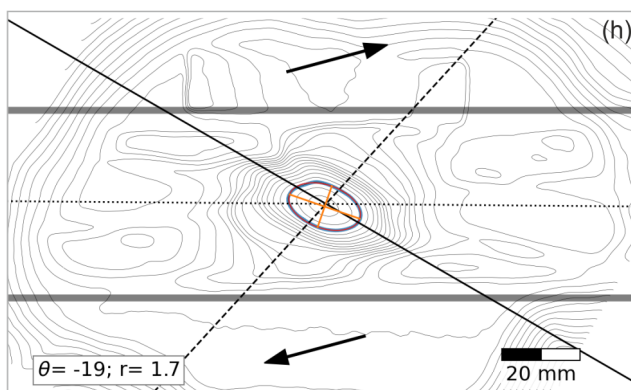
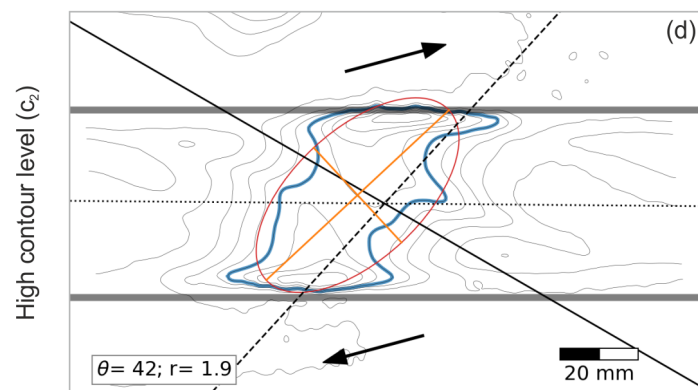
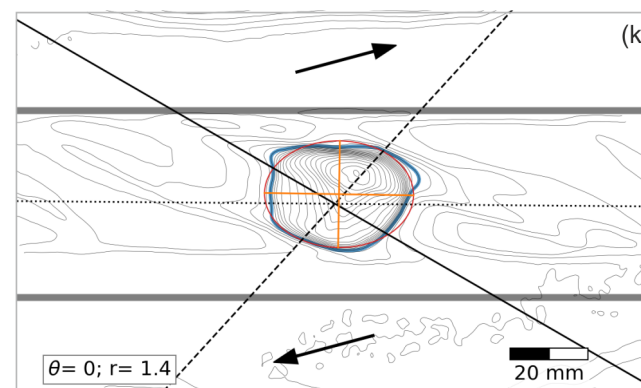
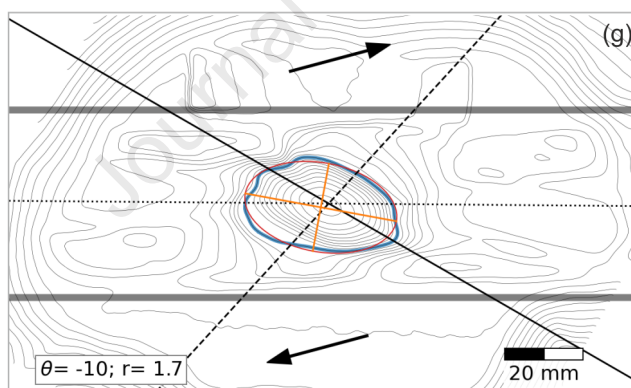
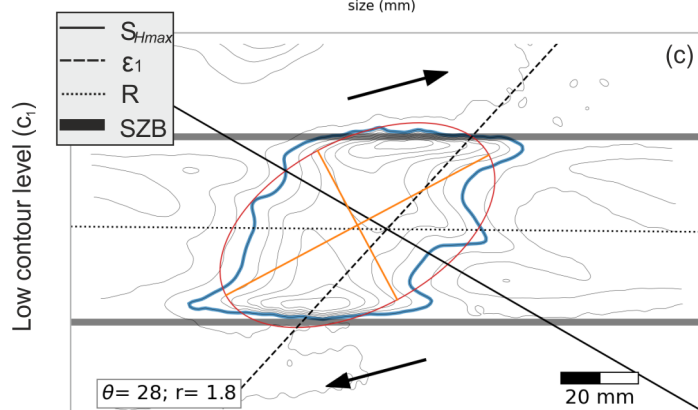
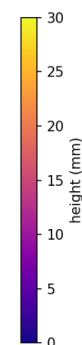
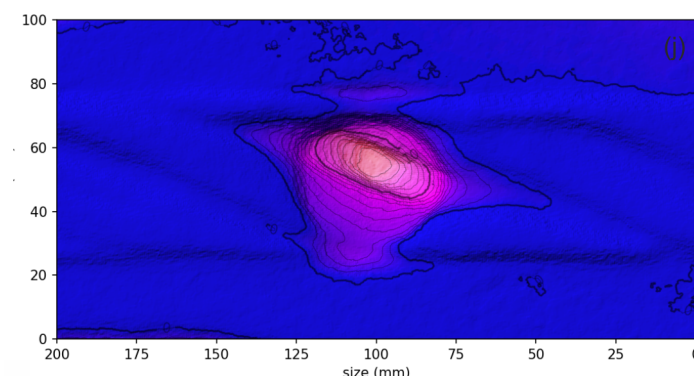
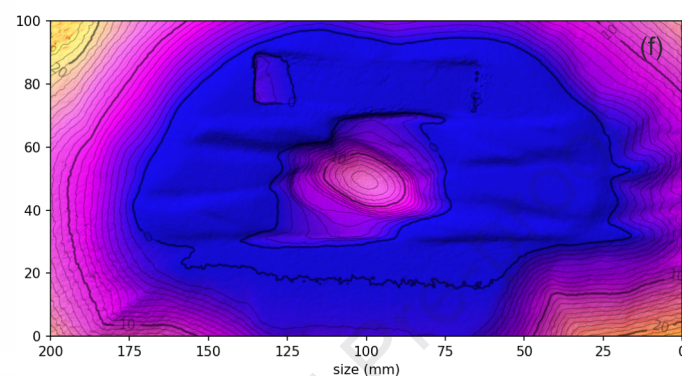
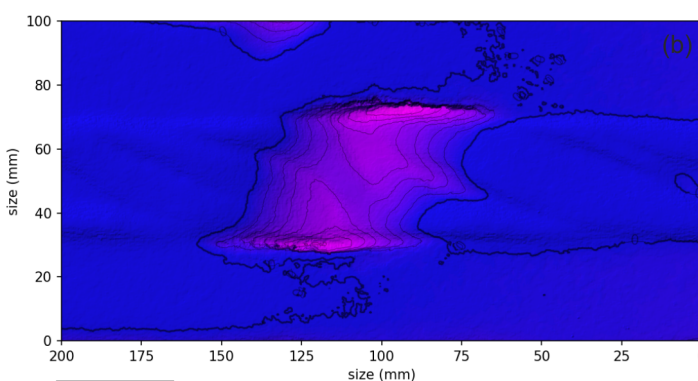
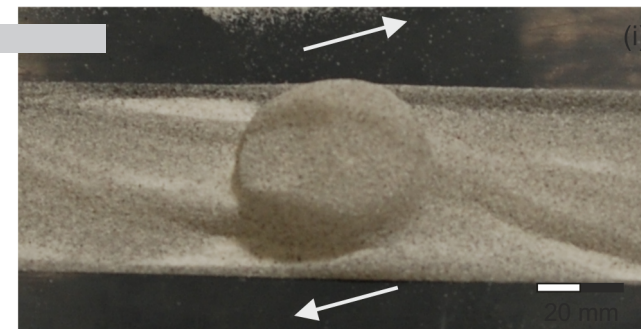


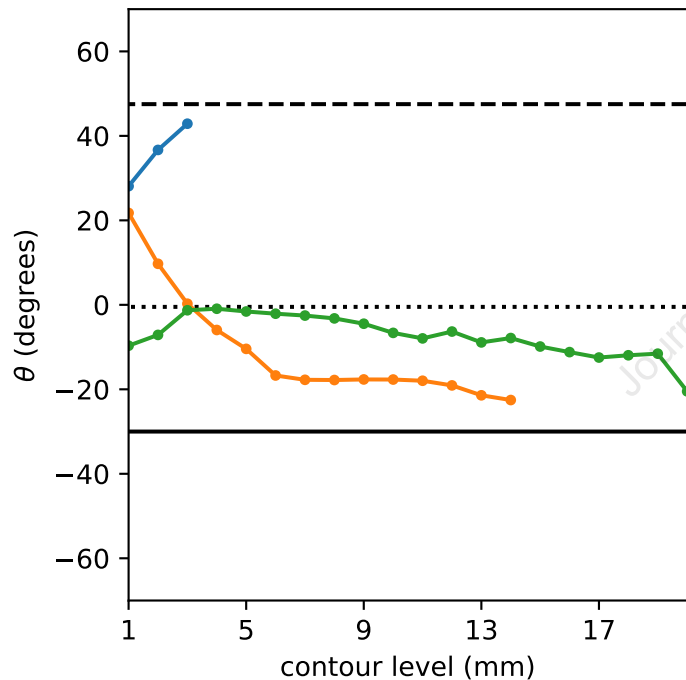
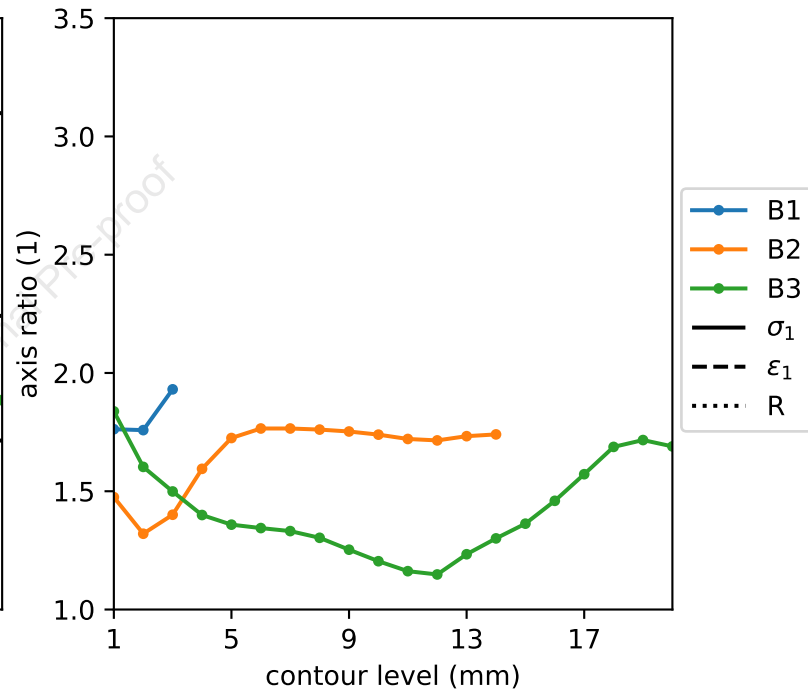
Journal Pre-proof

Model B2



Model B3



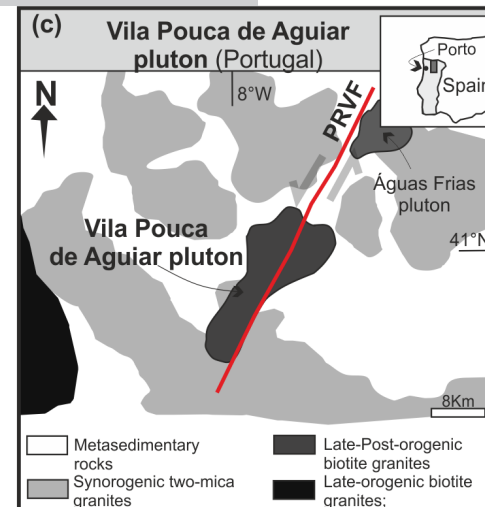
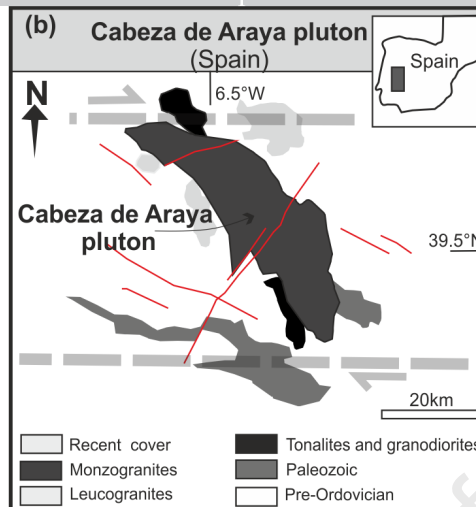
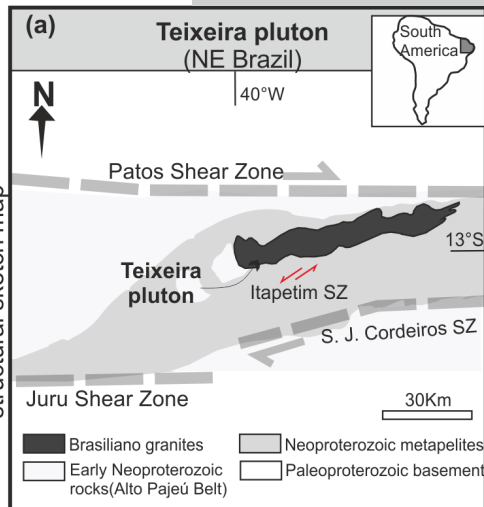
**(a)****(b)**

Pre-tectonic Pluton

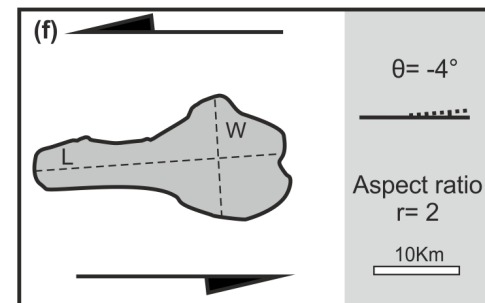
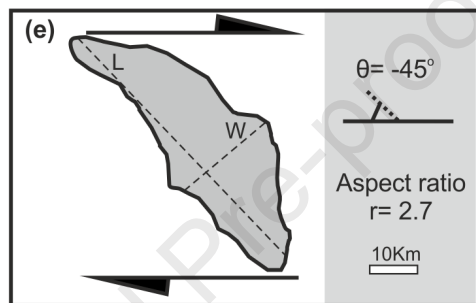
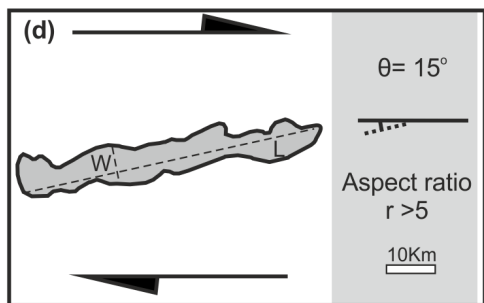
Journal Pre-proof

Syn-tectonic Pluton

Geological and structural sketch map



Geometrical features



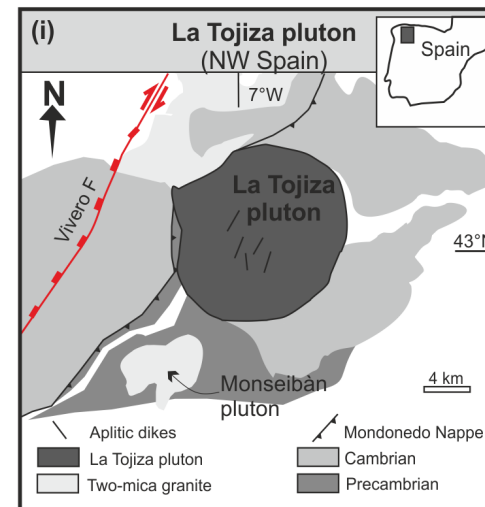
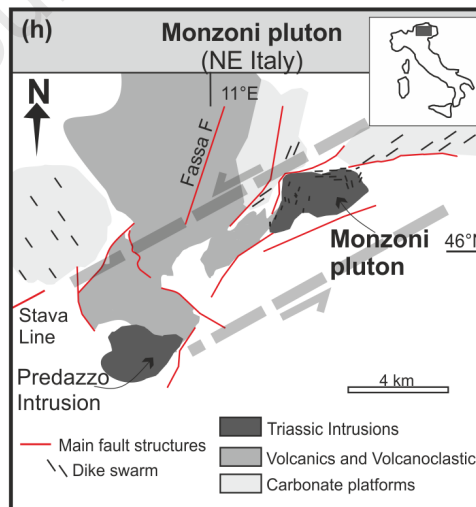
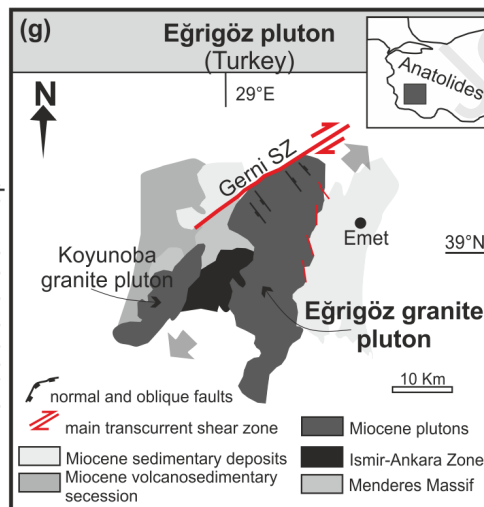
## Natural Examples in Transtension

Pre-tectonic Pluton

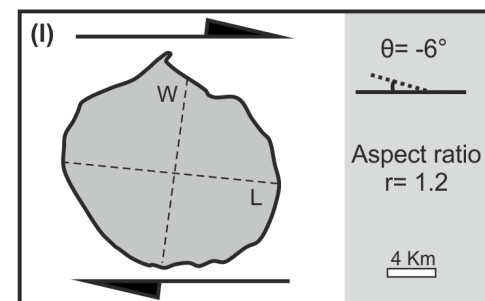
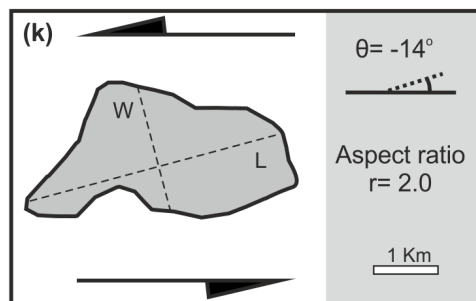
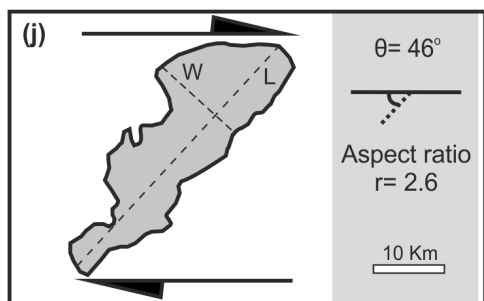
Syn-tectonic Pluton

Post-tectonic Pluton

Geological and structural sketch map



Geometrical features



## Highlights

- Spatial and temporal relation of magmatism in simple and transtensional shear zones.
- Intrusion asymmetry reflects regional stresses, fault pattern and strain field.
- Pre-tectonic intrusions show strong elongation parallel to the extension field.
- Syn-tectonic intrusions bear acute roofs and show typical scissor-tail apophyses.
- Inverse shear sense is observed exclusively in the post-tectonic intrusion.

### **Declaration of Interests**

☒ The authors declare that they have no known competing financial interests or personal relationships that could have appeared to influence the work reported in this paper.

☐ The authors declare the following financial interests/personal relationships which may be considered as potential competing interests: